Functional catalysts by design for renewable fuels and chemicals production

by

Nannan Shan

B.S., Qingdao Agricultural University, 2010
M.S., Beijing University of Chemical Technology, 2013

AN ABSTRACT OF A DISSERTATION

submitted in partial fulfillment of the requirements for the degree

DOCTOR OF PHILOSOPHY

Department of Chemical Engineering
College of Engineering

KANSAS STATE UNIVERSITY
Manhattan, Kansas

2019

Abstract

In the course of mitigating our dependence on fossil energy, it has become an urgent issue to develop unconventional and innovative technologies based on renewable energy utilization for fuels and chemicals production. Due to the lack of fundamental understanding of catalytic behaviors of the novel chemical compounds involved, the task to design and engineer effective catalytic systems is extremely challenging and time-consuming.

One central challenge is that an intricate balance among catalytic reactivity, selectivity, durability, and affordability must be achieved pertinent to any successful design. In this dissertation, density functional theory (DFT), coupled with modeling techniques derived from DFT, is employed to gain insights into molecular interactions between elusive intermediates and targeted functional catalytic materials for novel electrochemical and heterogeneous catalytic processes. Two case studies, i.e., electroreduction of furfural and step-catalysis for cyclic ammonia production, will be discussed to demonstrate the capability and utility of DFT-based theoretical modeling toolkits and strategies.

Transition metal cathodes such as silver, lead, and nickel were evaluated for furfuryl alcohol and 2-methylfuran production through detailed DFT modeling. Investigation of the molecular mechanisms revealed that two intermediates, mh6 and mh7 from mono-hydrogenation of furfural, are the key intermediates that will determine the product formation activities and selectivities. Nickel breaks the trends from other metals as DFT calculations suggested the 2-methylfuran formation pathway is most likely different from other cathodes. In this work, the Brønsted–Evans–Polanyi relationship, derived from DFT energy barrier calculations, has been found to be particularly reliable and computationally efficient for C-O bond activation trend predictions. To obtain the solvation effect on the adsorptions of biomass-derived compounds (e.g.,

furfural and glycerol), influence of explicit solvent was probed using periodic DFT calculations. The adsorptions of glycerol and its dehydrogenation intermediates at the water-platinum surface were understood via various water–adsorbate, water–water, and water–metal interactions. Interestingly, the bond-order-based scaling relationship established in solvent-free environment is found to remain valid based on our explicit solvent models.

In the second case study, step-catalysis that relies on manganese's ability to dissociate molecular nitrogen and as a nitrogen carrier emerges as an alternative route for ammonia production to the conventional Haber-Bosch process. In this collaborative project, DFT was used as the primary tool to produce the mechanistic understanding of NH_3 formation via hydrogen reduction on various manganese nitride systems (e.g., Mn_4N and Mn_2N). Both nickel and iron dopants have the potential to facilitate NH_3 formation. A broader consideration of a wide range of nitride configurations revealed a rather complex pattern. Materials screening strategies, supported by linear scaling relationships, suggested the linear correlations between NH_x ($x=0, 1, 2$) species must be broken in the development of optimal step catalysis materials. These fundamental findings are expected to significantly guide and accelerate the experimental material design.

Overall, molecular modeling based on DFT has clearly demonstrated its remarkable value beyond just a validation tool. More importantly, its unique predictive power should be prized as an avenue for scientific advance through the fundamental knowledge in novel catalysts design.

Functional catalysts by design for renewable fuels and chemicals production

by

Nannan Shan

B.S., Qingdao Agricultural University, 2010
M.S., Beijing University of Chemical Technology, 2013

A DISSERTATION

submitted in partial fulfillment of the requirements for the degree

DOCTOR OF PHILOSOPHY

Department of Chemical Engineering
College of Engineering

KANSAS STATE UNIVERSITY
Manhattan, Kansas

2019

Approved by:

Major Professor
Bin Liu

Copyright

Abstract

In the course of mitigating our dependence on fossil energy, it has become an urgent issue to develop unconventional and innovative technologies based on renewable energy utilization for fuels and chemicals production. Due to the lack of fundamental understanding of catalytic behaviors of the novel chemical compounds involved, the task to design and engineer effective catalytic systems is extremely challenging and time-consuming.

One central challenge is that an intricate balance among catalytic reactivity, selectivity, durability, and affordability must be achieved pertinent to any successful design. In this dissertation, density functional theory (DFT), coupled with modeling techniques derived from DFT, is employed to gain insights into molecular interactions between elusive intermediates and targeted functional catalytic materials for novel electrochemical and heterogeneous catalytic processes. Two case studies, i.e., electroreduction of furfural and step-catalysis for cyclic ammonia production, will be discussed to demonstrate the capability and utility of DFT-based theoretical modeling toolkits and strategies.

Transition metal cathodes such as silver, lead, and nickel were evaluated for furfuryl alcohol and 2-methylfuran production through detailed DFT modeling. Investigation of the molecular mechanisms revealed that two intermediates, mh6 and mh7 from mono-hydrogenation of furfural, are the key intermediates that will determine the product formation activities and selectivities. Nickel breaks the trends from other metals as DFT calculations suggested the 2-methylfuran formation pathway is most likely different from other cathodes. In this work, the Brønsted–Evans–Polanyi relationship, derived from DFT energy barrier calculations, has been found to be particularly reliable and computationally efficient for C-O bond activation trend predictions. To obtain the solvation effect on the adsorptions of biomass-derived compounds (e.g.,

furfural and glycerol), influence of explicit solvent was probed using periodic DFT calculations. The adsorptions of glycerol and its dehydrogenation intermediates at the water-platinum surface were understood via various water–adsorbate, water–water, and water–metal interactions. Interestingly, the bond-order-based scaling relationship established in solvent-free environment is found to remain valid based on our explicit solvent models.

In the second case study, step-catalysis that relies on manganese's ability to dissociate molecular nitrogen and as a nitrogen carrier emerges as an alternative route for ammonia production to the conventional Haber-Bosch process. In this collaborative project, DFT was used as the primary tool to produce the mechanistic understanding of NH_3 formation via hydrogen reduction on various manganese nitride systems (e.g., Mn_4N and Mn_2N). Both nickel and iron dopants have the potential to facilitate NH_3 formation. A broader consideration of a wide range of nitride configurations revealed a rather complex pattern. Materials screening strategies, supported by linear scaling relationships, suggested the linear correlations between NH_x (x=0, 1, 2) species must be broken in the development of optimal step catalysis materials. These fundamental findings are expected to significantly guide and accelerate the experimental material design.

Overall, molecular modeling based on DFT has clearly demonstrated its remarkable value beyond just a validation tool. More importantly, its unique predictive power should be prized as an avenue for scientific advance through the fundamental knowledge in novel catalysts design.

Table of Contents

List of Figures

List of Tables

Acknowledgements

First of all, my sincere and deepest gratitude goes to my advisor, Dr. Bin Liu, for his excellent mentorship, encouragement and patience throughout my Ph.D. program. His insightful comments are always incentive for me to seek the broad visions and perspectives of my research. I really appreciate his scientific inspiration and sage advice for my research to guide me to the success.

I would like to express my thanks to Dr. Christine Aikens for her constructive suggestions, guidance and invaluable discussion during my time at Kansas State University. I also would like to thank my committee members, Dr. Keith Hohn, Dr. Placidus Amama and Dr. Bala Natarajan, for their time and supportive comments on my research.

I am thankful to our collaborators from experimental groups, Dr. Peter Pfromm, Dr. Viktor Chikan and Pratikshya Sharma. Thanks for the communications with them on project meetings and their technical suggestions for my research.

I appreciate the wonderful research atmosphere provided by current and former lab members from Liu's and Aikens' groups, Mingxia Zhou, Song Liu, Jiajun Tang, Jiayi Xu, Jiahan Li, Narges Manavi, Chaoran Huang, Amendra Fernando Hewa Dewage, Natalia Karimova, Dimuthu Weerawardene, Ravithree Senanayake, Fahri Alkan, Gowri Udayangani, Pratima Pandeya, Olivia Hull, Zhen Liu and Shana Havenridge. Thanks for their friendship and advice. I have had the pleasure to work with undergraduate research assistants, Josephine Chen, Mary K. Hanchett, and Robert T. Lee. I really appreciate their enthusiasms and contributions.

I am truly grateful to Dr. James H. Edgar for his support and assistance during my time at Department of Chemical Engineering. I am thankful to all staff members, Cynthia Brott, Karen Strathman, Danita Deters, Debi Wahl, and Cindy Fowler, for their continuous efforts to make my life lovelier here. People from Beocat group, Dave Turner, Adam Tygart and Kyle Hutson, are highly acknowledged. Many thanks for their technical supports and nice responses every time.

I sincerely appreciate my life-mentor, Dr. Lianbin Xu, for his consistent inspiration, discussion, encouragement, and assistance these years. I also would like to express my gratitude to my dear friends, Jane Fox, Miaomiao Wu, Jiahui Xue, Jianxiong Li, Xu Li, Yixiao Li, Xin Zhao, Rigele Te, Zijun Wu, Shiqiang Jin, Zhenzhen Shi, Mac Mao, Qian Li, Huina Hu, and Lianjie Xue, for their friendship and help.

Finally, my special thanks go to my parents, my brother, my sister-in-law, my nephew and my niece for their endless love, encouragement, sacrifice, and support for me to get here. I was so lucky to have such a lovely family!

Dedication

To the truth of life, love and loyalty.

Chapter 1 - Introduction

The world's energy future is witnessing a significant revolution. Since the late 19th century, wood has been replaced by fossil fuels (i.e. coal, petroleum, and natural gas), which have become the major energy sources in the United States until the modern era. Today, it is remarkable to note that renewable and sustainable energy sources have transformed global energy consuming structure [1-3]. As shown in Figure 1.1, the combined share of U.S. energy consumption from renewable energy sources (i.e., biofuels, geothermal, nuclear, solar, wind and hydraulic power) has increased to 11% in 2017 [4]. Renewable fuels and chemicals production has become one of the most important scientific and technological topics to enable a sustainable future [5]. At the end of 2018, the US DOE (Department of Energy) Energy Efficiency and Renewable Energy (EERE) Office announced that a total of $20 million will be released to support more than one hundred new projects for innovative research and technology transfer related to renewable energy production and applications [6].

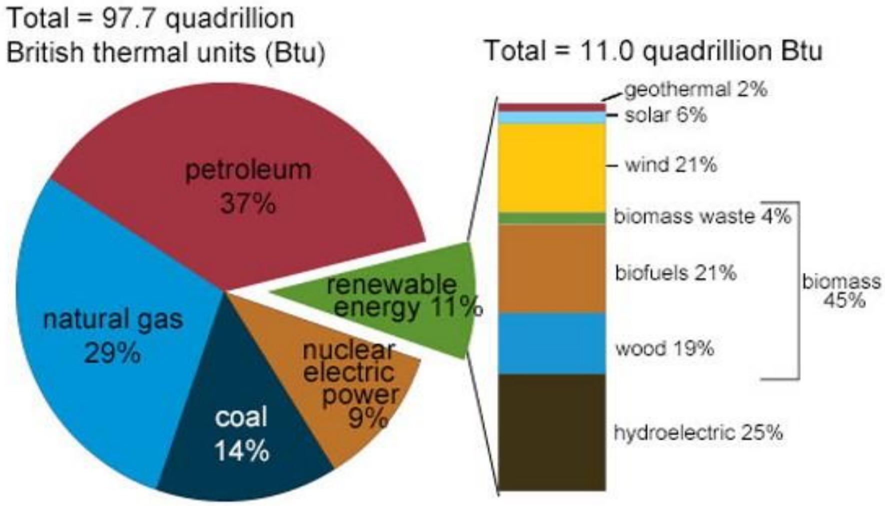

Figure 1.1 U.S. energy consumption sources in 2017 [4].

As shown in Figure 1.1, biomass accounts for nearly 50% of the renewable energy. Particularly, biofuels and biochemicals have the potential to alleviate our dependence on the carbon source from fossil fuels. Hence, when the CO_2 from the consumption of biofuels and biochemicals is recycled back during biomass growth, no net carbon shall be released into the atmosphere, as illustrated in Figure 1.2.

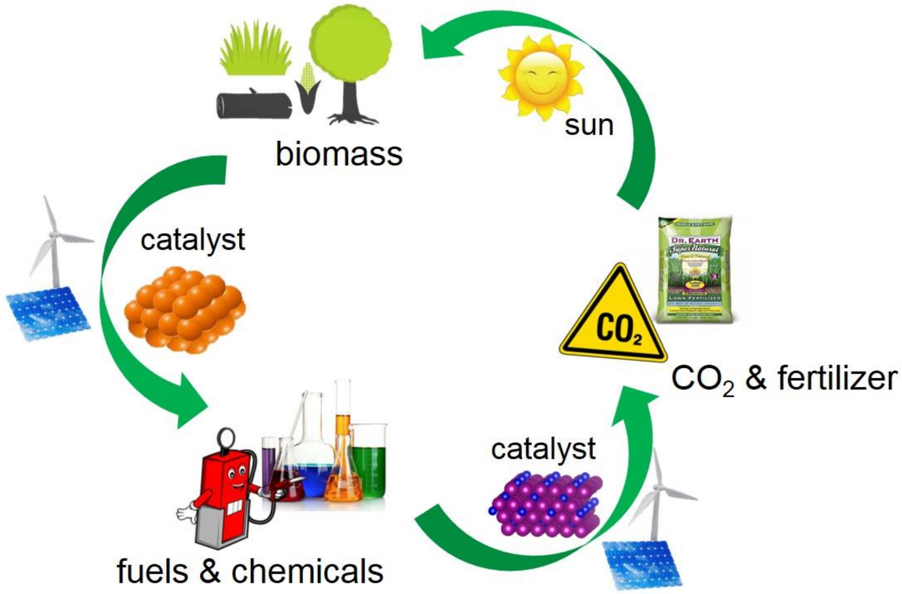

Figure 1.2 Renewable fuels and chemicals production in a sustainable way.

1.1 Computational Catalyst Design

Many value-added fuels and chemicals production involves catalytic reactions at the gas-solid, or liquid-solid interface [7-11]. An ideal catalyst should possess a balanced performance among reactivity, selectivity, and thermodynamic stability [12-17]. In addition, for practical application, the cost of catalysts for large-scale usage can also be a limiting factor as well. All these constraints must be considered as top priorities in the process of catalyst design.

In recent years, fundamental catalysis research is experiencing a notable transition from a trial-and-error-based practice to a strategy-driven approach rationalized with molecular-level insights obtained from either high resolution *in situ* characterization, or from theoretical modeling supported by quantum mechanical tools such as density functional theory (DFT) [18-22]. DFT calculations have gained tremendous recognition in the past twenty years as a particularly powerful tool to study catalysis problems by obtaining molecular adsorptions, characterizing reaction intermediates, searching the transition states, and simulating reaction rates.

Among the numerous successful case studies, the most representative example is none other than the Haber-Bosch process for ammonia synthesis, a catalytic process that has been playing a critical role in supporting 40% of the 7.6 billion global population today [23, 24]. Understandably, tremendous efforts have been devoted to improve ammonia catalysis continuously [25-30]. In early 20th century, a central scientific question has been proposed: whether molecular or atomic nitrogen adsorption was the "slow step" based on high-throughput experiments of thousands of metal and metal alloy catalysts [31, 32]. It was Ertl, awarded the Nobel Prize on this work, whose surface chemistry approach based on model catalyst surfaces finally resolved this debate and led to the development of modern catalysis [33]. Through the employment of the (111), (110), and (100) facets of Fe single crystal, Ertl and co-workers were able to reveal that the activation of the N–N bond is the rate-limiting step via their investigations of the molecular adsorptions of hydrogen (H_2), nitrogen (N_2), and ammonia (NH_3). It was later found that these fundamental ammonia production steps can be modeled at a very high level of accuracy with quantum mechanical level calculations with a very reasonable computational cost. Moreover, hypothetic reaction intermediates, which were almost impossible to detect experimentally at that time, can be directly modeled on the computer. For instance, Nørskov and co-workers [34] carried out DFT calculations by following Ertl's proposed mechanism on Fe single crystal facets, and demonstrated for the first time that theory and experiments can be integrated to solve catalysis problems. Since then, the first-principles modeling has been playing an increasing role in driving the advancement of a wide range of catalytic systems [35-43].

The predicative power of first-principles calculations for rational catalyst design is noteworthy based on the Sabatier principle, which suggested that the key reaction intermediates cannot bind on the catalyst active sites neither too strongly nor too weakly for the optical catalyst performance [44]. For ammonia synthesis, Nørskov et al. chose the binding of elemental N as the determining factor to represent ammonia production activity for a given catalyst in terms of the so-called 'volcano' plot. From theory, the CoMo alloy was identified as a high performance catalyst, which is later shown experimentally by Jacobsen et al. [45] to be indeed a superior catalyst for ammonia synthesis.

1.2 Catalytic Systems Considered in This Thesis

This thesis aims to utilize state-of-the-art computational tools to provide the fundamental understanding central to the technological innovations for renewable fuels and chemicals production. Two case studies will be discussed:

(1) Electrochemical reduction of furfural; and

(2) Step catalysis for ammonia synthesis.

1.2.1 Electrochemical Reduction of Furfural

Furfural has been identified as one important platform compound for manufacturing a variety of bio-chemicals and biofuels [46-49]. Today, an amount of more than 0.2 million tons per year of furfural is being produced, and has become one of the most common industrial chemicals derived from biomass [50]. Hydrogenation of furfural on various metal catalysts can lead to furfuryl alcohol (FA), 2-methylfuran (MF), furan, and tetrahydrofuran, as shown in Figure 1.3. Among these chemicals, FA and MF are the most valuable because FA is the common solvent used in the manufacture of resins, and MF is a gasoline alternative to boost the performance on anti-explosion, as the octane number of MF is shown to be higher than that of gasoline [51].

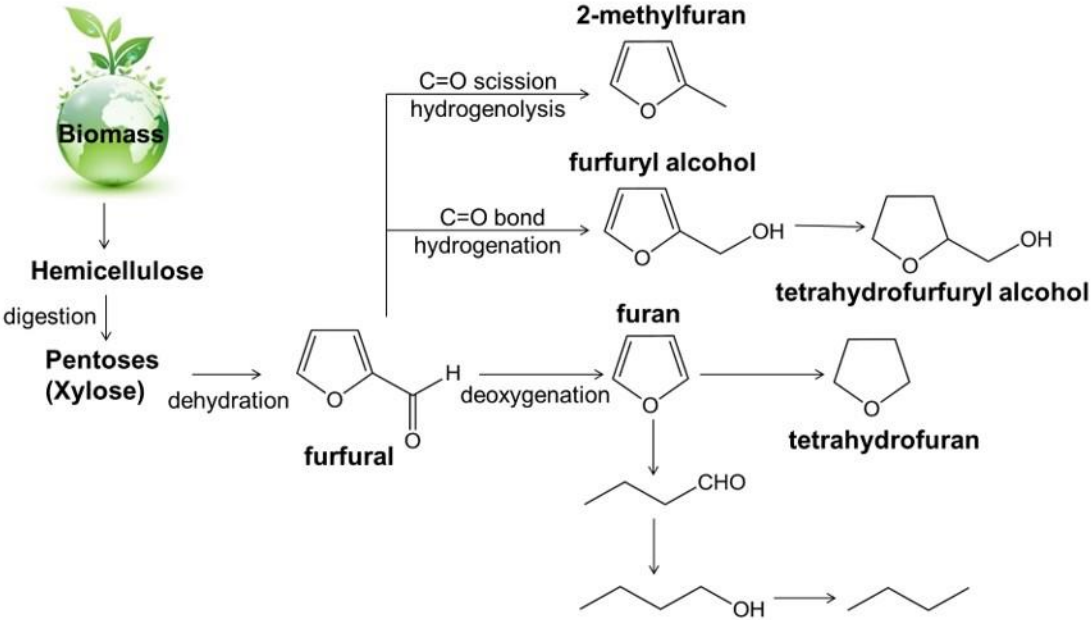

Figure 1.3 Schematic reaction roadmap for conversion of furfural to fuels and chemicals [8].

Electrochemical reduction of furfural to FA and MF can be carried out at atmospheric pressure and room temperature with non-gaseous hydrogen sources [52, 53]. Thus, this technology will be a promising alternative approach with meaningful economic and environmental advantages compared to heterogeneous processes via hydrogenation and hydrogenolysis [54, 55], which would require much higher pressure (0.1–1 MPa) and temperature (100–500°C). The molecular H_2 feedstock used will have to be produced through energy intensive routes (reforming) as well.

The product selectivity of furfural electroreduction strongly depends on the cathode materials. Cu was found to be effective for electrochemically catalyzing furfural into MF via hydrogenolysis, while Au, Pt, Ni, and Pb are more selective for FA via hydrogenation to varying degrees [52, 56-61]. However, the exact reaction pathways for the major product are still being debated. Current experimental hypothesis of MF formation considers FA as the intermediate for subsequent MF formation [52, 58, 59]. Current theoretical studies on heterogenous conversions of furfural to FA and MF on transition metals, such as Cu, Pt, and Pd, are not able to fully address these issues [62-64].

To further complicate the matter, the solvation effect will also play a critical role in influencing furfural reduction chemistries. It has been confirmed that explicit solvation is believed to affect both reaction kinetics and thermodynamics of CO_2 reduction [65-69]. Theoreical modeling of solvation effect on conversion of biomass still remains a challenging task due to the complexity and lack of detailed understanding of the liquid-metal interface. Both of the issues mentioned here will be addressed in this thesis.

1.2.2 Step Catalysis for Ammonia Synthesis

Large-scale ammonia production via Haber-Bosch consumes 1-2% of the global energy annually with high temperature and extremely enhanced pressure (at 500 °C and 300 bar), which were used to break N_2 triple bond and drive the chemical equilibrium toward NH_3 [7, 70]. Moreover, Haber-Bosch process requires 60% of global hydrogen production coming from 3-5% global natural gas annually [71]. In the past ten years, numerous approaches via non-thermal routes, or completely different nitrogen conversion pathways, have been proposed. For instance, electrochemical synthesis of NH_3 is now gaining a lot of attention because it is conducted at ambient pressure with protons as the hydrogen source either coming from solid or liquid electrolytes [26, 29, 72, 73], which thus decreases the need gaseous H_2 made from fossil fuels. However, the lack of novel electrolytes with high conductivity and low reactivity remain as the main obstacle to compete against the conventional method [72, 73].

More recently, Steinfeld and co-workers proposed a two-step solar thermochemical cycle for NH_3 synthesis at atmospheric pressure [74-77]. In this method, aluminum oxide (Al_2O_3) is first reduced to aluminum nitride (AlN) in the nitridation step. Then, water is used to extract its lattice nitrogen to obtain NH_3. After NH_3 production, the Al_2O_3 formed from AlN reduction is recycled to participate in nitridation in the next cycle. However, a potential issue is that high temperature (1000 – 2000 °C) is needed for Al_2O_3 nitridation.

The challenge for step catalysis process is to engineer a material that facilitates the utilization of elemental nitrogen in both nitridation and reduction [78]. Pfromm and co-workers have extensively investigated various transition metal (e.g., Cr, Mn, and Fe) nitrides as nitrogen carriers [27, 28, 78, 79]. Particularly, manganese nitrides (Mn_xN_y) are regarded as the most promising candidates due to their relatively favorable nitridation and reduction thermodynamics. However, the long-term stability of Mn nitrides and the low NH_3 yield [80] still need to be improved. Currently, modifications of Mn nitrides, via chemical doping and alloying, are being systematically explored and will be discussed in detail in this thesis.

1.2.3 Target Questions for This Dissertation

With theoretical modeling in this dissertation, few questions drawn through two case studies are waiting for answers. For the first case study, electrochemical reduction of furfural, the questions are:

(1) What is/are the dominant pathway(s) for FA and MF formations via electrocatalysis on transition metal cathodes?
(2) What determines the product selectivity for FA and MF productions on different metals?
(3) What is the role of explicit solvent for the biomass conversion?

For the second case study, step-catalysis for ammonia synthesis, key questions are:

(1) What are the reaction mechanisms for ammonia synthesis via step-catalysis using manganese nitride as the N carrier?
(2) Will doping or alloying of manganese nitride with other transition metals be beneficial to ammonia synthesis, and how?
(3) Are we able to establish some design principles for targeting the efficient catalysts for ammonia synthesis with modified manganese nitrides?

1.3 Organization of This Dissertation

The contents of this dissertation are organized in seven chapters. Chapter 1 (this chapter) provides a brief introduction on the research background and scope of the dissertation. Chapter 2 describes the basic theory and methodology being employed. Chapter 3 discusses the mechanistic investigation of furfural electroreduction on transition metals. Chapter 4 presents a novel approach to understand the explicit solvation effect on glycerol adsorption on platinum surface. Chapters 5 and 6 focus on ammonia production over Mn nitrides. The Fe and Ni doping effects, as well as a broader consideration of the modification impacts on nitrides, will be investigated in these chapters. The conclusions and outlook of this dissertation will be presented in Chapter 7.

Bibliography

[1]. Zhang, L.; Xu, C.; Champagne, P., Overview of recent advances in thermo-chemical conversion of biomass. *Energy Conversion and Management* **2010,** 51, (5), 969-982.

[2]. Nema, P.; Nema, R. K.; Rangnekar, S., A current and future state of art development of hybrid energy system using wind and PV-solar: A review. *Renewable and Sustainable Energy Reviews* **2009,** 13, (8), 2096-2103.

[3]. Blaabjerg, F.; Ionel, D. M., Renewable Energy Devices and Systems – State-of-the-Art Technology, Research and Development, Challenges and Future Trends. *Electric Power Components and Systems* **2015,** 43, (12), 1319-1328.

[4]. US Energy Information Administration, Renewable Energy Explained. *Available at https://www.eia.gov/energyexplained/?page=renewable_home* **2018**, updated July 13, 2018.

[5]. Kajikawa, Y.; Yoshikawa, J.; Takeda, Y.; Matsushima, K., Tracking emerging technologies in energy research: Toward a roadmap for sustainable energy. *Technological Forecasting and Social Change* **2008,** 75, (6), 771-782.

[6]. Office of Energy Efficiency & Renewable Energy, US Department of Energy. *Available at https://www.energy.gov/eere/articles/office-energy-efficiency-and-renewable-energy-announces-20-million-available-small* **2018**, Updated December 18, 2018.

[7]. Ertl, G., Reactions at surfaces: From atoms to complexity (Nobel lecture). *Angewandte Chemie-International Edition* **2008,** 47, (19), 3524-3535.

[8]. Sitthisa, S.; Resasco, D. E., Hydrodeoxygenation of Furfural Over Supported Metal Catalysts: A Comparative Study of Cu, Pd and Ni. *Catalysis Letters* **2011,** 141, (6), 784-791.

[9]. Rostrup-Nielsen, J. R., Catalytic Steam Reforming. *Catalysis* **1984,** 5, 1-117.

[10]. Besenbacher, F.; Chorkendorff, I.; Clausen, B. S.; Hammer, B.; Molenbroek, A. M.; Norskov, J. K.; Stensgaard, I., Design of a surface alloy catalyst for steam reforming. *Science* **1998,** 279, (5358), 1913-1915.

[11]. Cortright, R. D.; Davda, R. R.; Dumesic, J. A., Hydrogen from catalytic reforming of biomass-derived hydrocarbons in liquid water. *Nature* **2002,** 418, (6901), 964-967.

[12]. Office of Basic Energy Sciences, US Department of Energy, Basic Energy Needs Catalysis for Energy, Workshop Report. *Available at http://www.er.doe.gov/bes/reports* **2007**, Accessed June 1, 2010.

[13]. Nørskov, J. K.; Abild-Pedersen, F.; Studt, F.; Bligaard, T., Density functional theory in surface chemistry and catalysis. *Proceedings of the National Academy of Sciences* **2011,** 108, (3), 937.

[14]. Sutton, D.; Kelleher, B.; Ross, J. R. H., Review of literature on catalysts for biomass gasification. *Fuel Processing Technology* **2001,** 73, (3), 155-173.

[15]. Zhang, S.; Yuan, X.-Z.; Hin, J. N. C.; Wang, H.; Friedrich, K. A.; Schulze, M., A review of platinum-based catalyst layer degradation in proton exchange membrane fuel cells. *Journal of Power Sources* **2009,** 194, (2), 588-600.

[16]. Frontera, P.; Macario, A.; Ferraro, M.; Antonucci, P., Supported Catalysts for CO_2 Methanation: A Review. *Catalysts* **2017,** 7, (2).

[17]. Yu, W.; Porosoff, M. D.; Chen, J. G., Review of Pt-Based Bimetallic Catalysis: From Model Surfaces to Supported Catalysts. *Chemical Reviews* **2012,** 112, (11), 5780-5817.

[18]. Nørskov, J. K.; Bligaard, T.; Rossmeisl, J.; Christensen, C. H., Towards the computational design of solid catalysts. *Nature Chemistry* **2009,** 1, (1), 37-46.

[19]. Shan, N.; Zhou, M.; Hanchett, M. K.; Chen, J.; Liu, B., Practical Principles of Density Functional Theory for Catalytic Reaction Simulations on Metal Surfaces – from Theory to Applications. *Molecular Simulation* **2017,** 43, (10-11), 861-885.
[20]. O'Neill, B. J.; Jackson, D. H. K.; Lee, J.; Canlas, C.; Stair, P. C.; Marshall, C. L.; Elam, J. W.; Kuech, T. F.; Dumesic, J. A.; Huber, G. W., Catalyst Design with Atomic Layer Deposition. *ACS Catalysis* **2015,** 5, (3), 1804-1825.
[21]. Li, D.; Li, X.; Gong, J., Catalytic Reforming of Oxygenates: State of the Art and Future Prospects. *Chemical Reviews* **2016,** 116, (19), 11529-11653.
[22]. Greeley, J., Theoretical Heterogeneous Catalysis: Scaling Relationships and Computational Catalyst Design. *Annual Review of Chemical and Biomolecular Engineering* **2016,** 7, (1), 605-635.
[23]. Smil, V., Detonator of the Population Explosion. *Nature* **1999,** 400, (6743), 415-415.
[24]. Bosch, C., The development of the chemical high-pressure method during the establishment of the new ammonia industry, Nobel Lecture. **1932**.
[25]. Marnellos, G.; Stoukides, M., Ammonia synthesis at atmospheric pressure. *Science* **1998,** 282, (5386), 98-100.
[26]. Amar, I. A.; Lan, R.; Petit, C. T. G.; Tao, S., Solid-state Electrochemical Synthesis of Ammonia: A Review. *Journal of Solid State Electrochemistry* **2011,** 15, (9), 1845-1860.
[27]. Michalsky, R.; Parman, B. J.; Amanor-Boadu, V.; Pfromm, P. H., Solar thermochemical production of ammonia from water, air and sunlight: Thermodynamic and economic analyses. *Energy* **2012,** 42, (1), 251-260.
[28]. Michalsky, R.; Pfromm, P. H., Thermodynamics of metal reactants for ammonia synthesis from steam, nitrogen and biomass at atmospheric pressure. *AIChE Journal* **2012,** 58, (10), 3203-3213.
[29]. Yandulov, D. V.; Schrock, R. R., Catalytic reduction of dinitrogen to ammonia at a single molybdenum center. *Science* **2003,** 301, (5629), 76-78.
[30]. Arashiba, K.; Miyake, Y.; Nishibayashi, Y., A molybdenum complex bearing PNP-type pincer ligands leads to the catalytic reduction of dinitrogen into ammonia. *Nature Chemistry* **2011,** 3, (2), 120-125.
[31]. Emmett, P. H.; Brunauer, S., The Adsorption of Nitrogen by Iron Synthetic Ammonia Catalysts. *Journal of the American Chemical Society* **1934,** 56, 35-41.
[32]. Mittasch, A., Early studies of multicomponent catalysts. *Advances in Catalysis* **1950,** 2, 81-104.
[33]. Ertl, G., Surface science and catalysis - studies on the mechanism of ammonia-synthesis - the Emmett, P.H. Award address. *Catalysis Reviews-Science and Engineering* **1980,** 21, (2), 201-223.
[34]. Stoltze, P.; Nørskov, J. K., Bridging the pressure gap between ultrahigh-vacuum surface physics and high-pressure catalysis. *Physical Review Letters* **1985,** 55, (22), 2502-2505.
[35]. Stoltze, P.; Nørskov, J. K., A description of the high-pressure ammonia-synthesis reaction based on surface science. *Journal of Vacuum Science & Technology a-Vacuum Surfaces and Films* **1987,** 5, (4), 581-585.
[36]. Christoffersen, E.; Mortensen, J. J.; Stoltze, P.; Nørskov, J. K., N_2 interaction with Fe surfaces. *Israel Journal of Chemistry* **1998,** 38, (4), 279-284.
[37]. Stoltze, P.; Nørskov, J. K., An interpretation of the high-pressure kinetics of ammonia-synthesis based on a microscopic model. *Journal of Catalysis* **1988,** 110, (1), 1-10.

[38]. Stoltze, P.; Nørskov, J. K., The application of surface kinetic data to the industrial synthesis of ammonia - comment. *Surface Science* **1988,** 197, (1-2), L230-L232.

[39]. Stoltze, P.; Nørskov, J. K., The surface science based ammonia kinetics revisited. *Topics in Catalysis* **1994,** 1, (3-4), 253-263.

[40]. Dahl, S.; Logadottir, A.; Egeberg, R. C.; Larsen, J. H.; Chorkendorff, I.; Tornqvist, E.; Nørskov, J. K., Role of steps in N_2 activation on Ru(0001). *Physical Review Letters* **1999,** 83, (9), 1814-1817.

[41]. Boisen, A.; Dahl, S.; Nørskov, J. K.; Christensen, C. H., Why the optimal ammonia synthesis catalyst is not the optimal ammonia decomposition catalyst. *Journal of Catalysis* **2005,** 230, (2), 309-312.

[42]. Dahl, S.; Logadottir, A.; Jacobsen, C. J. H.; Nørskov, J. K., Electronic factors in catalysis: the volcano curve and the effect of promotion in catalytic ammonia synthesis. *Applied Catalysis a-General* **2001,** 222, (1-2), 19-29.

[43]. Honkala, K.; Hellman, A.; Remediakis, I. N.; Logadottir, A.; Carlsson, A.; Dahl, S.; Christensen, C. H.; Nørskov, J. K., Ammonia synthesis from first-principles calculations. *Science* **2005,** 307, (5709), 555-558.

[44]. Medford, A. J.; Vojvodic, A.; Hummelshøj, J. S.; Voss, J.; Abild-Pedersen, F.; Studt, F.; Bligaard, T.; Nilsson, A.; Nørskov, J. K., From the Sabatier principle to a predictive theory of transition-metal heterogeneous catalysis. *Journal of Catalysis* **2015,** 328, 36-42.

[45]. Jacobsen, C. J. H.; Dahl, S.; Clausen, B. S.; Bahn, S.; Logadottir, A.; Nørskov, J. K., Catalyst design by interpolation in the periodic table: Bimetallic ammonia synthesis catalysts. *Journal of the American Chemical Society* **2001,** 123, (34), 8404-8405.

[46]. Li, X.; Jia, P.; Wang, T., Furfural: A Promising Platform Compound for Sustainable Production of C_4 and C_5 Chemicals. *ACS Catalysis* **2016,** 6, 7621-7640.

[47]. Mariscal, R.; Maireles-Torres, P.; Ojeda, M.; Sadaba, I.; Lopez Granados, M., Furfural: A Renewable and Versatile Platform Molecule for the Synthesis of Chemicals and Fuels. *Energy & Environmental Science* **2016,** 9, (4), 1144-1189.

[48]. Lange, J.-P.; van der Heide, E.; van Buijtenen, J.; Price, R., Furfural-A Promising Platform for Lignocellulosic Biofuels. *ChemSusChem* **2012,** 5, (1), 150-166.

[49]. Huber, G. W.; Iborra, S.; Corma, A., Synthesis of Transportation Fuels from Biomass: Chemistry, Catalysts, and Engineering. *Chemical Reviews* **2006,** 106, (9), 4044-4098.

[50]. Nilges P , S. U., Electrochemistry for biofuel generation: production of furans by electrocatalytic hydrogenation of furfurals. *Energy Environ Sci* **2013,** 6, (10), 2925-2931.

[51]. Zhu, F. D. Y., Cr-free Cu-catalysts for the selective hydrogenation of biomass-derived furfural to 2-methylfuran: The synergistic effect of metal and acid sites. *Journal of Molecular Catalysis A* **2015,** 398, 140-148.

[52]. Nilges, P.; Schröder, U., Electrochemistry for Biofuel Generation: Production of Furans by Electrocatalytic Hydrogenation of Furfurals. *Energy & Environmental Science* **2013,** 6, (10), 2925-2931.

[53]. Jung, S.; Biddinger, E. J., Electrocatalytic Hydrogenation and Hydrogenolysis of Furfural and the Impact of Homogeneous Side Reactions of Furanic Compounds in Acidic Electrolytes. *ACS Sustainable Chemistry & Engineering* **2016,** 4, (12), 6500-6508.

[54]. Li, F.; Cao, B.; Ma, R.; Liang, J.; Song, H.; Song, H., Performance of Cu/TiO_2-SiO_2 Catalysts in Hydrogenation of Furfural to Furfuryl Alcohol. *The Canadian Journal of Chemical Engineering* **2016,** 94, (7), 1368-1374.

[55]. Kotbagi, T. V.; Gurav, H. R.; Nagpure, A. S.; Chilukuri, S. V.; Bakker, M. G., Highly Efficient Nitrogen-doped Hierarchically Porous Carbon Supported Ni Nanoparticles for the Selective Hydrogenation of Furfural to Furfuryl Alcohol. *RSC Advances* **2016,** 6, (72), 67662-67668.
[56]. Albert, W. C.; Lowy, A., The Electrochemical Reduction of Furfural. *Journal of the Electrochemical Society* **1939,** 75, (1), 367-375.
[57]. Parpot, P.; Bettencourt, A. P.; Chamoulaud, G.; Kokoh, K. B.; Belgsir, E. M., Electrochemical Investigations of the Oxidation–reduction of Furfural in Aqueous Medium: Application to Electrosynthesis. *Electrochimica Acta* **2004,** 49, (3), 397-403.
[58]. Li, Z.; Kelkar, S.; Lam, C. H.; Luczek, K.; Jackson, J. E.; Miller, D. J.; Saffron, C. M., Aqueous Electrocatalytic Hydrogenation of Furfural Using a Sacrificial Anode. *Electrochimica Acta* **2012,** 64, 87-93.
[59]. Zhao, B.; Chen, M.; Guo, Q.; Fu, Y., Electrocatalytic Hydrogenation of Furfural to Furfuryl Alcohol Using Platinum Supported on Activated Carbon Fibers. *Electrochimica Acta* **2014,** 135, 139-146.
[60]. Green, S. K.; Lee, J.; Kim, H. J.; Tompsett, G. A.; Kim, W. B.; Huber, G. W., The Electrocatalytic Hydrogenation of Furanic Compounds in a Continuous Electrocatalytic Membrane Reactor. *Green Chemistry* **2013,** 15, (7), 1869-1879.
[61]. Wang, F.; Xu, M.; Wei, L.; Wei, Y.; Hu, Y.; Fang, W.; Zhu, C. G., Fabrication of La-doped TiO_2 Film Electrode and Investigation of Its Electrocatalytic Activity for Furfural Reduction. *Electrochimica Acta* **2015,** 153, 170-174.
[62]. Liu, B.; Cheng, L.; Curtiss, L.; Greeley, J., Effects of Van der Waals Density Functional Corrections on Trends in Furfural Adsorption and Hydrogenation on Close-Packed Transition Metal Surfaces. *Surface Science* **2014,** 622, 51-59.
[63]. Shi, Y.; Zhu, Y.; Yang, Y.; Li, Y.-W.; Jiao, H., Exploring Furfural Catalytic Conversion on Cu(111) from Computation. *ACS Catalysis* **2015,** 5, (7), 4020-4032.
[64]. Vorotnikov, V.; Mpourmpakis, G.; Vlachos, D. G., DFT Study of Furfural Conversion to Furan, Furfuryl Alcohol, and 2-Methylfuran on Pd(111). *ACS Catalysis* **2012,** 2, (12), 2496-2504.
[65]. Nie, X. W.; Esopi, M. R.; Janik, M. J.; Asthagiri, A., Selectivity of CO_2 Reduction on Copper Electrodes: The Role of the Kinetics of Elementary Steps. *Angewandte Chemie-International Edition* **2013,** 52, (9), 2459-2462.
[66]. Nie, X. W.; Luo, W. J.; Janik, M. J.; Asthagiri, A., Reaction mechanisms of CO_2 electrochemical reduction on Cu(111) determined with density functional theory. *Journal of Catalysis* **2014,** 312, 108-122.
[67]. Shi, C.; Chan, K.; Yoo, J. S.; Nørskov, J. K., Barriers of Electrochemical CO2 Reduction on Transition Metals. *Organic Process Research & Development* **2016,** 20, (8), 1424-1430.
[68]. Peterson, A. A.; Abild-Pedersen, F.; Studt, F.; Rossmeisl, J.; Norskov, J. K., How copper catalyzes the electroreduction of carbon dioxide into hydrocarbon fuels. *Energy & Environmental Science* **2010,** 3, (9), 1311-1315.
[69]. Cheng, T.; Xiao, H.; Goddard, W. A., Reaction Mechanisms for the Electrochemical Reduction of CO_2 to CO and Formate on the Cu(100) Surface at 298 K from Quantum Mechanics Free Energy Calculations with Explicit Water. *Journal of the American Chemical Society* **2016,** 138, (42), 13802-13805.
[70]. Erisman, J. W.; Sutton, M. A.; Galloway, J.; Klimont, Z.; Winiwarter, W., How A Century of Ammonia Synthesis Changed the World. *Nature Geosci* **2008,** 1, (10), 636-639.

[71]. Nazemi, M.; El-Sayed, M. A., Electrochemical Synthesis of Ammonia from N2 and H2O under Ambient Conditions Using Pore-Size-Controlled Hollow Gold Nanocatalysts with Tunable Plasmonic Properties. *The Journal of Physical Chemistry Letters* **2018,** 9, (17), 5160-5166.
[72]. Licht, S.; Cui, B. C.; Wang, B. H.; Li, F. F.; Lau, J.; Liu, S. Z., Ammonia Synthesis by N_2 and Steam Electrolysis in Molten Hydroxide Suspensions of Nanoscale Fe_2O_3. *Science* **2014,** 345, (6197), 637-640.
[73]. Skodra, A.; Stoukides, M., Electrocatalytic synthesis of ammonia from steam and nitrogen at atmospheric pressure. *Solid State Ionics* **2009,** 180, (23-25), 1332-1336.
[74]. Galvez, M. E.; Halmann, M.; Steinfeld, A., Ammonia production via a two-step Al_2O_3/AlN thermochemical cycle. 1. Thermodynamic, environmental, and economic analyses. *Industrial & Engineering Chemistry Research* **2007,** 46, (7), 2042-2046.
[75]. Gálvez, M. E.; Frei, A.; Halmann, M.; Steinfeld, A., Ammonia Production via a Two-Step Al_2O_3/AlN Thermochemical Cycle. 2. Kinetic Analysis. *Industrial and Engineering Chemistry Research* **2007,** 46, (7), 2047-2053.
[76]. Gálvez, M. E.; Hischier, I.; Frei, A.; Steinfeld, A., Ammonia Production via a Two-Step Al_2O_3/AlN Thermochemical Cycle. 3. Influence of the Carbon Reducing Agent and Cyclability. *Industrial and Engineering Chemistry Research* **2008,** 47, (7), 2231-2237.
[77]. Galvez, M. E.; Frei, A.; Meier, F.; Steinfeld, A., Production of AlN by Carbothermal and Methanothermal Reduction of Al_2O_3 in a N_2 Flow Using Concentrated Thermal Radiation. *Industrial & Engineering Chemistry Research* **2009,** 48, (1), 528-533.
[78]. Heidlage, M. G.; Kezar, E. A.; Snow, K. C.; Pfromm, P. H., Thermochemical Synthesis of Ammonia and Syngas from Natural Gas at Atmospheric Pressure. *Industrial & Engineering Chemistry Research* **2017,** 56, (47), 14014-14024.
[79]. Michalsky, R.; Pfromm, P. H., An Ionicity Rationale to Design Solid Phase Metal Nitride Reactants for Solar Ammonia Production. *The Journal of Physical Chemistry C* **2012,** 116, (44), 23243-23251.
[80]. Michalsky, R.; Avram, A. M.; Peterson, B. A.; Pfromm, P. H.; Peterson, A. A., Chemical looping of metal nitride catalysts: low-pressure ammonia synthesis for energy storage. *Chemical Science* **2015,** 6, (7), 3965-3974.

Chapter 2 - Quantum Mechanical Theory and Methodology

Chapter 2 is reproduced with permission from:

Shan, N.; Zhou, M.; Hanchett, M. K.; Chen, J.; Liu, B., “Practical principles of density functional theory for catalytic reaction simulations on metal surfaces-from theory to applications”, *Molecular Simulation*, 2017, 43(10-11), 861-885.

2.1 Kohn–Sham Density Functional Theory

First-principles (or *ab initio*) methods treat interacting, inhomogeneous, N-body systems (e.g., molecules, solids, and surfaces) without any empirical data or parameters, where the wave function $\Psi(r_1, \ldots, r_N)$ can be approximated by the product of N single-particle wave functions, $\psi_i(r_i)$, as expressed in Equation (1).

$$\Psi(r_1, \ldots, r_N) = \psi_1(r_1) \cdots \psi_N(r_N) \quad (1)$$

In Kohn and Sham’s formulation [1], the single-particle (for particle *i*) Schrödinger equation describing a system of non-interacting electrons can be written in the form of Equation (2). The Hamiltonian consists of the electronic kinetic term and the effective potential functional ($\upsilon_{eff}(r)$ in Equation (3)), which itself is a functional of the electron density ($\rho(r)$, evaluated using Equation (4)).

$$\left[-\frac{\hbar^2}{2m}\nabla_i^2 + \upsilon_{eff}(r)\right]\psi_i(r) = \varepsilon_i\psi_i(r) \quad (2)$$

$$\upsilon_{eff}(r) = V_{en}(r) + \int \frac{\rho(r')}{|r - r'|}dr' + V_{xc}[\rho(r)] \quad (3)$$

$$\rho(r) = \sum_i |\psi_i(r_i)|^2 \tag{4}$$

The ground state density (ρ) and energy (ε_i) shall be solved self-consistently according to the general scheme illustrated in Figure 2.1. The procedure begins with the assumption of initial electron density, followed by the construction of the Coulombic and exchange-correlation potentials in the Hamiltonian, and then the solution of new density and energy for the next round of iteration.

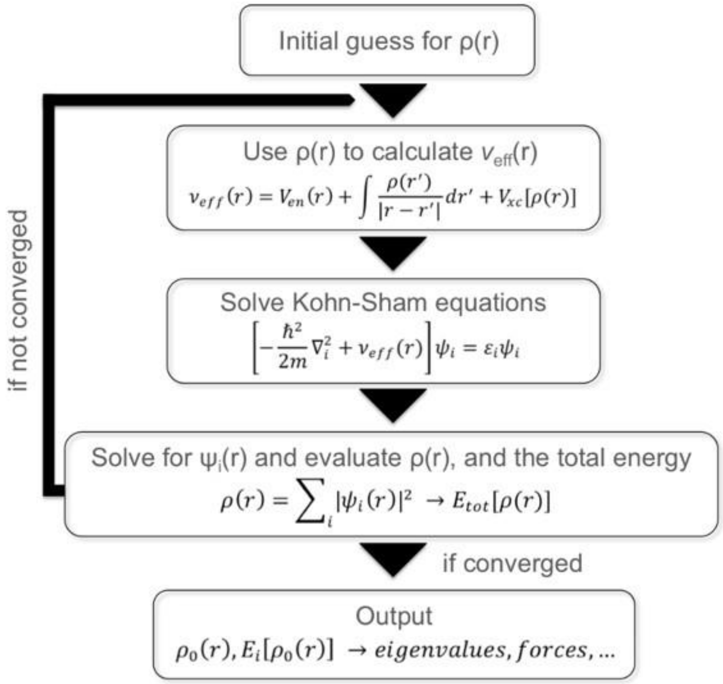

Figure 2.1 A general self-consistent scheme to solve the Kohn-Sham equation, adapted with permission from Ref [2]. Copyright 2017, Taylor & Francis.

2.1.1 Plane Wave Basis Set

For solid crystal systems, the wave function is formulated based on the Bloch's theorem [3]. Hence, in a crystal, the wave function ($\psi_k(\vec{r})$) of an electron occupying a state of k (i.e., a wave vector confined to the first Brillouin Zone) in a periodic potential can be written as Equation (5),

$$\psi_{\vec{k}}(\vec{r}) = e^{i\vec{k}\cdot\vec{r}} u_{\vec{k}}(\vec{r}) \tag{5}$$

$$\rho(r) \approx \sum\nolimits_{k} |\psi_k(\vec{r})|^2 \tag{6}$$

where $u_{\vec{k}}(\vec{r})$ is a periodic function with the same periodicity as the supercell. The use of plane wave-based wave function offers great numerical efficiency.

Each electron occupies a k state, and the density (ρ) will be constructed by integrating over an infinite number (i.e., continuous) of k values. In fact, wave functions are varying slowly, therefore, it is possible to approximate density with Equation (6) using a finite number of k-points. A number of schemes have been devised, such as the Monkhorst-Pack method [4], to generate a set of 'special' k-points. Based on the Bloch's theorem, the plane wave basis set can be expanded into Equation (7) in the reciprocal space.

$$\psi_{ik}(\vec{r}) = \sum\nolimits_{\vec{G}} c_{i\vec{k}}(\vec{G})\, e^{i(\vec{k}+\vec{G})\cdot\vec{r}} \tag{7}$$

where $\vec{G}$ is the lattice vector in the reciprocal space. $c_{i\vec{k}}(\vec{G})$ is the expansion coefficient corresponding to vector $\vec{G}$. In fact, this coefficient becomes smaller as $|\vec{G}|^2$ increases. Therefore, it is sufficient to truncate the infinite series in Equation (7) and only include the plane waves up to the cutoff energy E_{cut} as in Equations (8) and (9). In practice, the ground state energy and density converge rather quickly with the number of k-points and the cutoff energy used for the integration of the reciprocal space. The plane wave-based DFT has been implemented in a number of popular packages (e.g. ABINIT [5], CASTEP [6], CPMD [7], DACAPO [8], Quantum Espresso [9], and VASP[10, 11]).

$$E_{cut} = \frac{\hbar^2}{2m}\vec{G}_{cut}^2 \tag{8}$$

$$\left|\vec{k} + \vec{G}\right| < \vec{G}_{cut} \tag{9}$$

2.1.2 Pseudopotential

Electron wave functions oscillate rapidly when the potential in the proximity to the nuclei becomes very attractive. Thus, all electron calculations with full Coulombic potential are rather expensive. Furthermore, the wave functions close to the nuclei are usually not directly responsible for the surface chemistries. For this reason, pseudopotential methods have been developed and widely adopted by representing the valence electrons with full wave functions, but smoother approximate functions for core electrons, which are often ‘frozen’ (i.e., pre-calculated and fixed). Current methods include norm-conserving pseudopotentials [12-16], ultra-soft pseudopotentials [14, 17, 18], and the projector augmented wave (PAW) method [19]. The PAW pseudopotential is more effective in mitigating the artificial effects introduced by the treatment.

2.1.3 Electron Exchange-Correlation

In the Kohn-Sham DFT formulation, the exchange-correlation energy (E_{XC}, shown in Equation (3)) accounts for: (1) the electron kinetic energy difference between the exact interacting system and the non-interacting approximation; and (2) the Coulombic interactions of electrons with their own exchange-correlation hole. The computation of E_{XC} has to be approximated due to its unknown form. In past two decades, methods to approximate E_{XC} at various levels of theory have been developed, summarized and known as the *Jacob*'s ladder [20, 21]. The local density approximation (LDA), generalized gradient approximation (GGA), Meta-GGA, and hybrid functionals are included along *Jacob's* ladder with the increase of accuracy [20].

The generalized gradient approximation (GGA) functionals, in which local electron density as well as local gradient of electron density is integrated for E_{XC}, remain a primary functional choice in DFT calculations thanks to the balance between accuracy and computational cost, although GGA functionals usually overestimate the lattice constants. Different approaches to treat the gradient of the electron density have produced a large number of distinct GGA functionals, such as the Perdew-Wang (PW91) [22], the Perdew-Burke-Ernzerhof (PBE) [23], the revised PBE (RPBE) [8], the PBE re-parametrized for solids (PBEsol) [24], and the Becke-Lee-Yang-Parr functional (BLYP) [25, 26]. Mavrikakis and co-workers employed PW91 and RPBE functionals to obtain the chemisorption energies of atomic (H, O, N, S and C), molecular (N_2, CO, NO), and radical species (CH_3, OH) on Rh(111) up to within 0.15 eV of the experimental values [27]. Hammer et al. [28] showed that the GGA functional also performs better at predicting H_2 chemisorption energy and the H-H bond dissociation barrier on Cu(111) than the LDA functional. Pederson et al. [29] proposed that GGA lead to a more reasonable C-C dissociation barrier of 8.7

kcal/mol, while LDA lead to a barrier of about 0.7 kcal/mol, a factor of 20 smaller than experiment value.

It has long been recognized that the neglect of the long-range electron correlations (i.e., dispersions) in GGA functionals is inadequate and sometimes erroneous when describing intermolecular, or molecule-surface interactions. Prominent examples include adsorptions of benzene, furfural, hydrocarbons, as well as many layered 2D systems, such as graphite, hexagonal boron nitride (hBN), and MoS_2, where the interlayer van der Waals forces cannot be ignored. In fact, within the past 15 years, a number of empirical and functional approaches have quickly emerged in the effort to account for the dispersion effects properly.

Using a pre-calculated C_6 coefficient for the dispersion energy, the DFT-D2 and DFT-D3 methods, proposed by Grimme [30, 31], offer a remarkably reliable means by correcting the GGA calculations at a negligible additional computational cost. Alternatively, Tkatchenko and Scheffler [32] proposed to compute the dispersion correction using the reference atomic C_6 coefficients, which are scaled based on the atom's chemical environment. By adding the dispersion description directly to the exchange-correlation function as an additional non-local correlation term, a number of vdW-DF functionals were developed [33, 34]. Further improvements upon vdW-DF functionals, involving changes to both exchange and non-local correlation terms, produces a 'opt'-class functionals, such as optPBE-vdW, optB88-vdW and optB86b-vdW [35], which have shown noticeable improvements in structural and energetic calculations [36]. Although useful, it should be noted that the dispersion forces could be *over-corrected*, resulting in overestimated adsorption energies. The overall quality of these methods may very well depend on the reference dataset used in the functional development. Recently, a methodology based on Bayesian error estimation using cross-validation methods from machine learning has been developed by Wellendorff et al. [37], which enables the approximation of electron exchange-correlation using more flexible model space. The Bayesian error estimation-based functional (BEEF) is also applied to obtain the van der Waals correlation, abbreviated as BEEF–vdW. It has been shown that the BEEF-vdW functional is competing well with several GGA, vdW-DF, and meta-GGA functionals in computing intramolecular bond energies, chemisorption energies, molecular reaction barriers, molecular reaction energies, bulk solid cohesive energies, lattice constants, and interaction energies of non-covalently bonded complexes [37].

2.1.4 Electron Self-Interaction Errors

It is worthwhile pointing out that the errors generated by standard GGA functionals in calculating the lattice parameters, magnetic moments, band gaps, oxygen vacancy formation, and reaction energies of most transition metal oxides (most notably, TiO_2 [38-40], CeO_2 [41, 42], Fe_2O_3 [43], or NiO [44]) could also be due to self-interaction errors (SIEs). The discussion on the origin and treatments of SIEs has been presented in several review articles [44, 45]. In order to address this issue, parameters, i.e., U and J accounting for respective electron Coulombic and exchange interactions, are added to the calculated total energy with the same angular orbital momentum, known as the LDA+U or GGA+U methods [44-46]. When implementing this approach, the Hubbard U parameter can be determined empirically via the U-parameter screening based on the known properties of the material. Wang et al. [47] computed the oxidation of 3d (V, Cr, Mn, Fe, Co, Ni, and Cu) transition metals to identify the main contributions (i.e., the overbinding and SIE of the GGA functional) to the systematic errors for a wide range of materials.

2.2 Building Single Crystal Surfaces

Building the crystal surface structure is the first step of modeling. Surfaces with uniform well-defined sites play a central role in surface science and catalysis. The use of ‘plane surfaces’ has been rationalized by Langmuir, who believes that ‘if the principles in this case are well understood, it should then be possible to extend the theory to the case of porous bodies’ [48].

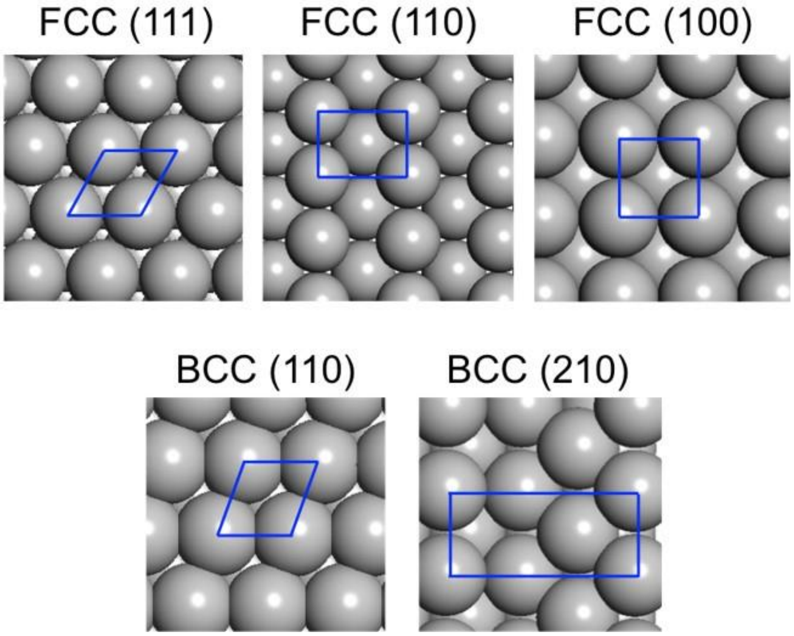

Figure 2.2 Surface models based on face-centered cubic (FCC) and body-centered cubic (BCC) single crystals. The blue lines indicate the 2D Bravais lattices. Adapted with permission from Ref [2]. Copyright 2017, Taylor & Francis.

The practice of using well-defined model surfaces is well suited for periodic DFT calculations, which are particularly well suited for the treatments of crystalline systems. A model surface can be generated from the cleavage of a perfect single crystal. For instance, low-index facets, such as (111), (100), and (110) are the basal planes of the face-centered cubic (FCC) and body-centered cubic (BCC) lattices [3], and are frequently employed. For FCC crystals, as illustrated in Figure 2.2, the (111) facet is the most close-packed (i.e., surface atom with the maximum coordination number), and also the lowest surface energy. For BCC crystals, the (110) facet is the most close-packed.

Atoms with lower coordination numbers can be found in step, corners, and defect sites, which can be presented by either low-index single crystal planes, for example, the (211) and (322) facet [49], or by artificially created architectures by adding or removing atoms in the lattice. Other crystal facets are also used to represent the catalyst corner, kink sites, which can be modeled using facet (321)[50-53], facet (531) [54, 55], facet (643) [55], facet (763) [49], and facet (854) [49, 56].

In periodic DFT calculations, slab models in a supercell that is bounded with periodic lateral boundaries, and separated by vacuum space perpendicular to the surface, are also used to accommodate specific computational needs. Figure 2.3 illustrates a FCC (755) supercell model consisting of both the (111) terrace and (211) step sites.

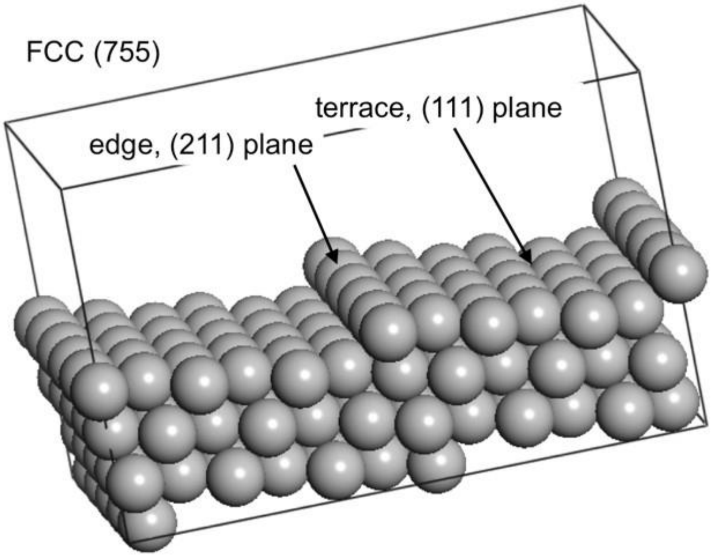

Figure 2.3 A supercell model based on the FCC (755) facet, with periodic boundaries indicated by the black lines. The terrace (flat) and step sites are indicated. Adapted with permission from Ref [2]. Copyright 2017, Taylor & Francis.

2.3 Energetics of Chemisorption and Thermodynamics Estimation

2.3.1 Linear Scaling Relationship for Binding Energy Estimation

DFT modeling can obtain the thermodynamic and kinetic properties of the reactions. Atomic and molecular adsorptions are essential, both experimentally and computationally, in probing surface active sites and surface reactivity. In computational catalysis, binding energies are the most fundamental properties for catalyst screening and catalyst design. With the adsorption energies of reactants, intermediates and products, as well as the transition state searching, one can generate the potential energy surface for a specific reaction to figure out the thermodynamic mechanisms. The quantum mechanical DFT computational cost grows exponentially with increasing number of atoms [57]. To avoid the unnecessary computational cost spent on those highly metastable species, a more efficient strategy is to be able to quickly identify the most thermodynamically stable species without explicit DFT calculations.

Abild-Pederson, Greeley, and coworkers [58] first formulated linear scaling relationships between the binding energies of several main group elements (i.e. C, O, N, S) and their hydrogenated counterparts (i.e. CH_x, OH_x, NH_x and SH_x) based on periodic DFT calculations. As an example, Figure 2.4 (a) shows that the adsorption energies of elemental nitrogen (ΔE^{N}) and NH_x (x=1–2) (ΔE^{NH_x}) follow a linear trend, as described by Equation (10),

$$\Delta E^{NH_x} = \gamma \Delta E^{N} + \xi \tag{10}$$

where $\gamma = (x_{max} - x)/x_{max}$, in which x_{max} represents the maximum number of H atoms to which N can form a single covalent bond. In the case of N, x_{max} is 3, satisfying its natural valency as in NH_3.

x is the total H atoms that N actually bonds. Hence, the slope of the linear function in Equation (10) can be understood with simple geometric bond-order variables.

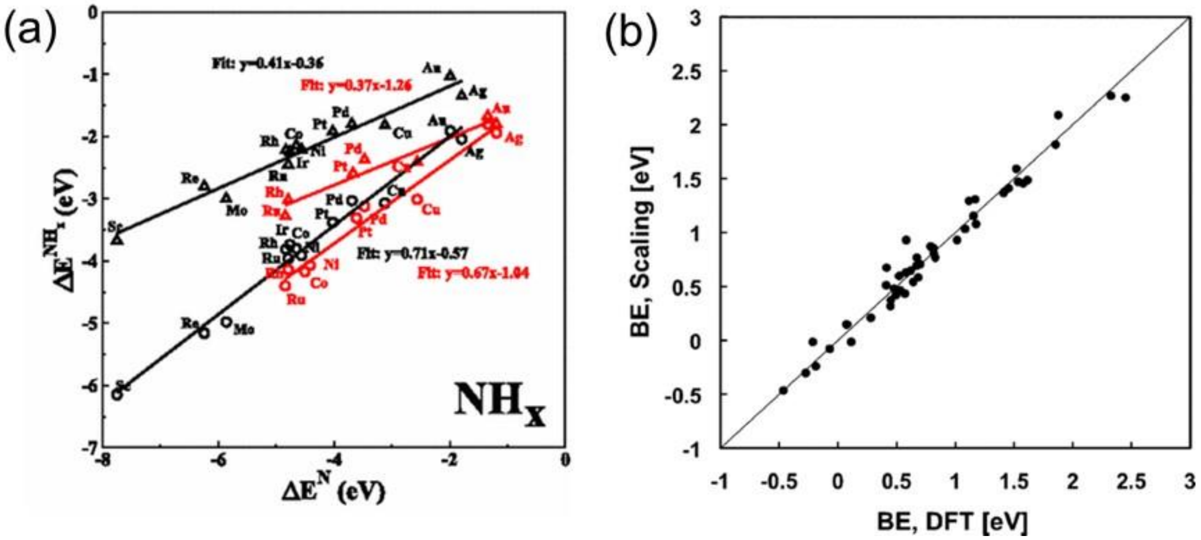

Figure 2.4 Binding energies of NH_x intermediates (circles: x=1; triangles: x=2) plotted against adsorption energies of N, The data points represent results for close-packed (black) and stepped (red) surfaces on various transition-metal surfaces [58]. (b) Predicted binding energies using Equation (11) for glycerol dehydrogenation intermediates on Pt(111) [59].

The existence of such linear scaling relationship originates from the *d*-band theory, where Hammer and Nørskov [60-62] identified that the *d*-electron state contribution is responsible for the variation of adsorbate-substrate bond energy from one metal to the next, and used this theory to explain the variation of surface reactivities of different metal substrates. Equation (10) indicates that the binding energy of AH_x (ΔE^{AH_x}) can be estimated using ΔE^{A} instead. A represents the main group elements (i.e. C, O, N, S). It can also be learned from Equation (10) that ξ, determined by the linear fit, is independent of the actual substrate.

The linear scaling relationship is particularly useful as adsorbate molecules become larger. Liu and Greeley [59, 63] devised a scaling scheme for a glycerol-derived species, $C_3H_xO_3^*$ (x = 0-8), can be defined by Equation (11):

$$BE_{C_3H_xO_3^*} = \sum_i p_{Ci}v_{Ci} + \sum_i p_{Oi}v_{Oi} + \sum_i p_{CiOj}v_{Ci}v_{Oj} + \sum_i p_{CiCj}v_{Ci}v_{Cj} + BE_{glycerol}, \tag{11}$$

where $BE_{glycerol}$ is the adsorption energy of gas phase glycerol on the Pt(111) surface. The variables v_{Ci} and v_{Oi} represent the degree of undersaturation of C and O atoms, and are defined the same way as the scaling relationship presented in Equation (10) previously. For this reason, it can be noted that the scaling formalism, described in Equation (11), is also motivated by the bond-order conservation principle, in which the undersaturated C and O atoms try to satisfy their gas-phase valency. The first order terms in Equation (11) are analogous to Equation (10). The interactions between adjacent undersaturated C and O, or C and C atoms, are accounted for with second order valency terms in Equation (11). The parameters in Equation (11) will be determined from fitting to DFT calculations. For glycerol decomposition, Equation (11) works remarkably well, as shown in Figure 2.4 (b). The overall standard error of within 0.2 eV can be reached.

2.3.2 Estimations of Thermodynamic Properties

The relationships between macroscopic thermodynamic properties (e.g., entropy, enthalpy, and Gibbs free energy) and quantum mechanical calculations can be linked through statistical mechanical treatment via partition functions in a straightforward manner. The total partition function, q_{total}, can be expressed by the products of individual contributions from various motions, such as the electronic, translational, rotational, and vibrational modes, as in Equation (12):

$$q_{total} = q_{electronic} \times q_{translation} \times q_{rotation} \times q_{vibration}. \tag{12}$$

Le et al. [64] presented a comprehensive description of the calculations of partition functions pertaining to computational surface chemistry. In this thesis, the key aspects for rate constant and equilibrium constant estimations for surface elementary reaction steps are briefly summarized.

For strong binding species, such as CO adsorption on Pt(111), the translational and rotational modes are frustrated, and lost upon adsorption except for vibrational modes. The vibrational partition, $q_{vibrational}$, can then be calculated using Equation (13).

$$q_{vibrational} = \prod_{i=1}^{3N} \left(\frac{1}{1 - e^{-\beta h c v_i}}\right) \tag{13}$$

where h is the Planck's constant, v_i is the i^{th} vibrational mode, N is the number of relaxed atoms, and $\beta = {}^{1}/_{k_B T}$. k_B is the Boltzmann constant, and c is the speed of light.

For weakly bounded adsorbates, such as H_2O on Pt(111), the molecule can be approximated as a two-dimensional (2D) gas, which is still able to access the translational and rotational modes in the surface plane. Hence, the associated translational and rotational partition functions can be calculated by Equations (14) and (15).

$$q_{translational(A,T)}^{2D} = \left(\frac{2\pi m k_B T}{h^2}\right) A \tag{14}$$

$$q_{rotational}^{2D} = \frac{\pi^{1/2}}{\sigma}\left(\frac{8\pi^2 I_{zz} k_B T}{h^2}\right)^{1/2}, \tag{15}$$

where m is the mass, A is the surface area, I_{zz} is the moment of inertia representing the z-axis (the only possible rotational mode on the surface) through the mass center of the adsorbate. The vibrational degrees of freedom thus become 3N-3 due to the consideration of the translational and rotational molecular motions. Lastly, the electronic partition function is usually considered to be the degeneracy of the ground state (except NO) because the electronic energy is much larger and only the ground state energy is relevant.

Using the calculated partition functions, the standard entropy (S°), internal energy (U°), enthalpy (H°), and Gibbs free energy (G°) can be calculated using Equations (16 – 24):

$$S_{2D-translation}^{\circ}(\mathrm{T}) = \mathrm{R}[\ln\left(\frac{2\pi m k_B T}{h^2} A\right) + 1] \tag{16}$$

$$S_{2D-rotation}^{\circ}(\mathrm{T}) = \mathrm{R}[\ln(\frac{\pi^{1/2}}{\sigma}\left(\frac{8\pi^2 I_{zz} k_B T}{h^2}\right)^{1/2}) + \frac{1}{2}] \tag{17}$$

$$S_{vibration}^{\circ}(\mathrm{T}) = \mathrm{R}\sum_i [\frac{hcv_i/k_B T}{e^{\beta hcv_i} - 1} - \ln(1 - e^{-\beta hcv_i})] \tag{18}$$

$$U_{2D-translation}^{\circ}(\mathrm{T}) = \mathrm{RT} \tag{19}$$

$$U_{2D-rotation}^{\circ}(\mathrm{T}) = \frac{1}{2}\mathrm{RT} \tag{20}$$

$$U_{vibration}^{\circ}(\mathrm{T}) = \mathrm{RT}\sum_i \frac{\beta hcv_i}{\exp\left(\frac{hcv_i}{k_B T}\right) - 1} \tag{21}$$

$$U^{\circ}_{correction} = U^{\circ}_{translation} + U^{\circ}_{rotation} + U^{\circ}_{vibration} \quad (22)$$

$$H^{\circ} = E_{electronic} + ZPE + U^{\circ}_{corrections} \quad (23)$$

$$G^{\circ} = H^{\circ} - TS^{\circ} \quad (24)$$

where R is the gas constant, $E_{electronic}$ is the total energy from DFT calculation, and ZPE is the zero point energy expressed as $ZPE = \frac{1}{2}\sum_i hcv_i$.

2.3.3 Computational Hydrogen Electrode Method for Electrochemical Reactions

The estimations of thermodynamics for electrochemical reactions are obtained based on the computational hydrogen electrode (CHE) model established by Nørskov et al. [65], where the free energy of the proton-electron pair ($\mu(H^+ + e^-)$) is equivalent to the chemical potential of ½H_2 in gas phase ($\frac{1}{2}\mu\left(H_{2(g)}\right)$) at all pH values, temperature and pressure of 1 atm, which can be represented by Equation (25),

$$\mu(H^+ + e^-) = \frac{1}{2}\mu\left(H_{2(g)}\right) - eU \quad (25)$$

where e is the elementary positive charge, and U is the applied potential bias. For example, the elementary step of furfural ($C_5H_4O_2$) hydrogenation to monohydrogenated intermediate ($C_5H_5O_2$) can be written as Equation (26),

$$C_5H_4O_2{}^{*} + (H^+ + e^-) \rightarrow C_5H_5O_2{}^{*} \quad (26)$$

where an asterisk (*) indicates adsorbed species on the surface. The free energy change, ΔG, of this elementary step can be written as Equation (27),

$$\Delta G = G(C_5H_5O_2{}^*) - G(C_5H_4O_2{}^*) - [\frac{1}{2}G\big(H_{2(g)}\big) - eU] \tag{27}$$

2.4 Kinetics, and Reaction Rates of Surface Reactions

2.4.1 Transition State Searching Techniques

It is fundamentally important in surface science to identify and elucidate minimum energy paths (MEPs) describing atomic or molecular diffusion or reaction on a given potential energy surface (PES). For surface reactions, it is also necessary to find those elusive transition states and obtain reliable energy barriers to determine kinetics. A number of techniques have been developed. As summarized by Henkelman et al. [66], when both the initial and final states are known, the drag method, Nudged Elastic Band (NEB) [67, 68], the conjugate peak refinement (CPR) method,[69] the Ridge method [70], Synchronous Transit [71], and so on can be used. If only the initial state is known, on the other hand, the dimer method [72] becomes more appropriate. Most quantum mechanical packages have incorporated one or more of these algorithms enabling the finding of MEPs and transition states. In this thesis, NEB and dimer methods are mainly adopted.

2.4.1.1 Nudged Elastic Band (NEB) Method

In the NEB method, a string of images (or geometric interpolations) between the known reactant (R) and product (P), as indicated in Figure 2.5(a), are generated and relaxed. The locations of intermediate images can be generated from a simple linear interpolation, labeled by ‘1’ in blue in Figure 2.5(a). Subsequent optimizations will relax the images to the real MEP, labeled by ‘2’ in red in Figure 2.5(a). Hence, NEB is an ideal method in order to obtain an overall view of the potential energy landscape. In principle, more than one saddle point can be identified this way. The true force on each image in the elastic band is decomposed into a perpendicular and a parallel component to the MEP. A nudging force, perpendicular to the path, is necessary to ensure that there will not be severe corner cutting at the curve of the MEP.

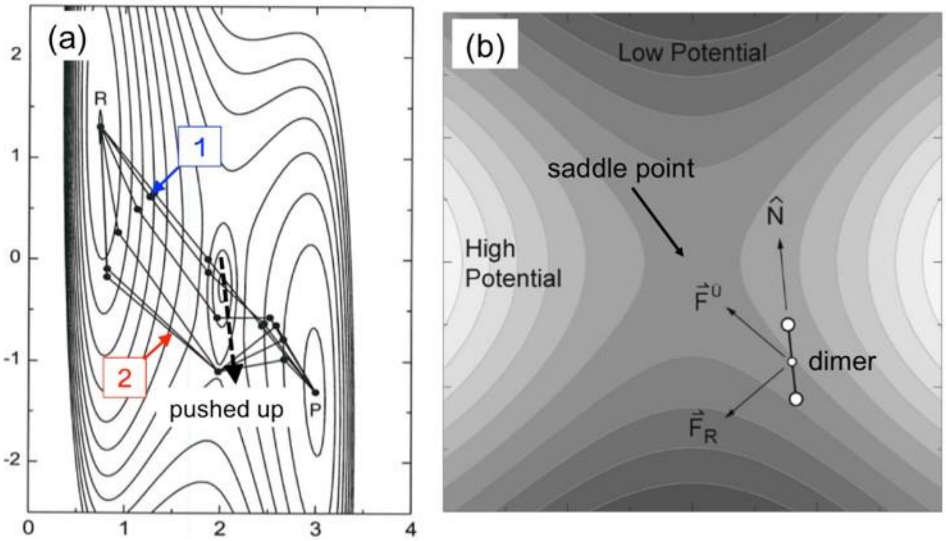

Figure 2.5 Schematic illustration of finding the MEP and the saddle point on a potential energy surface using (a) the NEB method (with three interpolated images), where ‘1’ represents the initial interpolated path and ‘2’ represents the final relaxed path, and the dashed arrow indicates that the highest energy image is being pushed up toward the saddle point; (b) the dimer method. Adapted with permission from Ref [2]. Copyright 2017, Taylor & Francis.

The Climbing Image NEB (CI-NEB) method introduced a modification to the original NEB, where the highest energy image is moved energy uphill by turning off the nudging force and only keeping the inverted parallel component. In this way, the image tries to maximize its energy along the band, and minimize in all other directions. In principle, when this image converges, this image will fall to the saddle point exactly. If the maximum image is initially very far from the saddle point, and the climbing image was used from the outset, the path would develop very different spacing on either side of the saddle point.

2.4.1.2 Dimer Method

The dimer method can be used when the product state on the MEP is not known. Based on the eigenvector-following theory, the dimer method is developed to use the first derivatives of the potential energy in order to find the saddle point [66, 72]. Two replicas (or a 'dimer') are constructed, with a fixed separation (c.a. 0.1 Å) between each other, as indicted in Figure 2.5(b). The dimer is rotated and the energy is minimized, giving the direction of the lowest frequency normal mode ($\widehat{N}$), shown in Figure 2.5(b). The dimer image is moved toward the saddle point with an effective force ($\vec{F}^U$), which acts on the center of the dimer and is calculated using the component of the true force ($\vec{F}_R$) along the inverted direction of $\widehat{N}$. The dimer method does not require the evaluation the Hessian matrix and is, therefore, much more efficient. In fact, the dimer method provides a convenient means for solving problem, where the MEP is potentially complex and hard to define, or only the knowledge of the transition state is needed. Lately, it has been shown that the CI-NEB and dimer methods can be used together [73, 74], where an educated guess can be first obtained from CI-NEB, followed by a refinement using the dimer method if only the transition state is the target.

2.4.2 Brønsted–Evans–Polanyi (BEP) Relationship

It is well known that transition state search remains an extremely computationally intensive task. Inspired by the reaction kinetics theory, the BEP [75], which established an empirical linear relationship between the reaction energy (ΔE) and the activation energy (E_a), has been developed and adapted for surface reactions. One such relationship can be represented by Equation (28).

$$\boldsymbol{E_a = \alpha \cdot \Delta E + \ \beta} \tag{28}$$

Usually, the kinetics of an elementary reaction step can be characterized with two fitting parameters (α and β, as in Equation (28)), which depend on reaction types and catalyst. Based on the accumulation of vast DFT calculations, it has been shown that the α values are in the range of 0.5–0.9 on metal surfaces [76, 77]. The β parameter values fall in the range of 1–2 eV. The variations of α and β parameters governed by geometric and electronic characters of catalysts provide an avenue to manipulate catalytic functionality for catalyst design. Because of the tremendous computational acceleration provided by the BEP relationship, it has become an integral component in the field of computational catalysis. Figure 2.6 gives an example of BEP relationship for CO dissociation in methanation reaction on transition metals [78]. The reaction barriers, E_a, is linearly correlated with CO molecule dissociation energy.

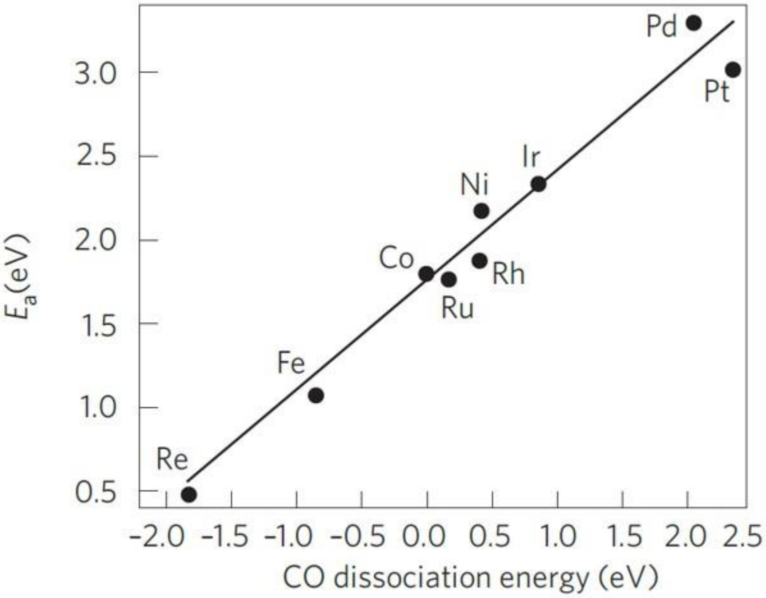

Figure 2.6 Brønsted–Evans–Polanyi relation for CO dissociation over transition metal surfaces [78]. The transition state potential energy, E_a, is linearly related to the CO dissociation energy.

2.4.3 Rate Constant of Elementary Steps and Microkinetic Modeling

From the first-principles methods, the elementary step rate constant can be calculated. Within the transition state theory (TST) framework, rate constant can be obtained from Equation (29),

$$k_{TST}(T) = \frac{k_B T}{h} \frac{q_{TS}}{q_R} exp\left(-\frac{E_a}{k_B T}\right) \tag{29}$$

where q_{TS}, q_R are the partition functions associated with the transition state and reactants, respectively, and E_a is the activation energy (see CI-NEB and dimer method).

The equilibrium constant, K_{eq}(T), can be derived from the van’t Hoff equation, as in Equation (30),

$$K_{eq}(T) = \frac{k_f(T)}{k_r(T)} = exp\left(-\frac{\Delta G}{k_B T}\right) \qquad (30)$$

By combining DFT and statistical mechanical treatment, the above framework enables the thermochemistry estimations that are functions of temperature and pressure. The formulation presented above lays the theoretical foundation for *ab initio* microkinetic modeling.

Microkinetic modeling breaks down an overall catalytic reaction in the form of elementary steps, with well-defined reaction rate expression for each step. Hence, microkinetic modeling is capable of consolidating the experimental data and molecular-level modeling in a quantitative model, using information that can be directly produced from first-principles calculations.

A general first step to construct a microkinetic model is to identify all the elementary steps that may be involved in the catalytic process [79-81]. Stoltze and Nørskov [82] presented the first microkinetic model for the study of ammonia synthesis. The associated rate constants and thermodynamic equilibrium constants can be measured or computationally determined. Working within the mean-field theory microkinetic modeling framework, Medford et al. [83] developed a python-based kinetic modeling package (CatMAP), which also supporting linear scaling relationship, BEP relationship, and the capability to account for the adsorbate–adsorbate interactions for both heterogeneous and electrocatalytic models.

2.4.4 Sabatier's Principle and 'Volcano' Plot

The establishment of linear scaling relationships and BEP relationship provide the indication that catalytic behavior can be understood in a predictive way. Catalytic reactions are governed by only a handful of reaction parameters. For instance, in ammonia synthesis, the binding energy of nitrogen, N_2 dissociation energy, and the activation energy of N-N bond cleavage play the determining roles. In addition, the well-known Sabatier's principle states that the optimal catalyst should neither bind reactants too weakly nor the products too strongly. This principle dictates that the best catalyst would offer an optimum value for binding energy, reaction energy, or the energy barrier of the rate-limiting step that ultimately results in the maximum catalyst activity. These binding energies and energy barriers are known as 'catalytic descriptors' [78], which are essentially the reflection of the mechanistic origin of the performance of a catalyst. The concept of descriptor can be conveniently adapted as a rational catalyst design parameter.

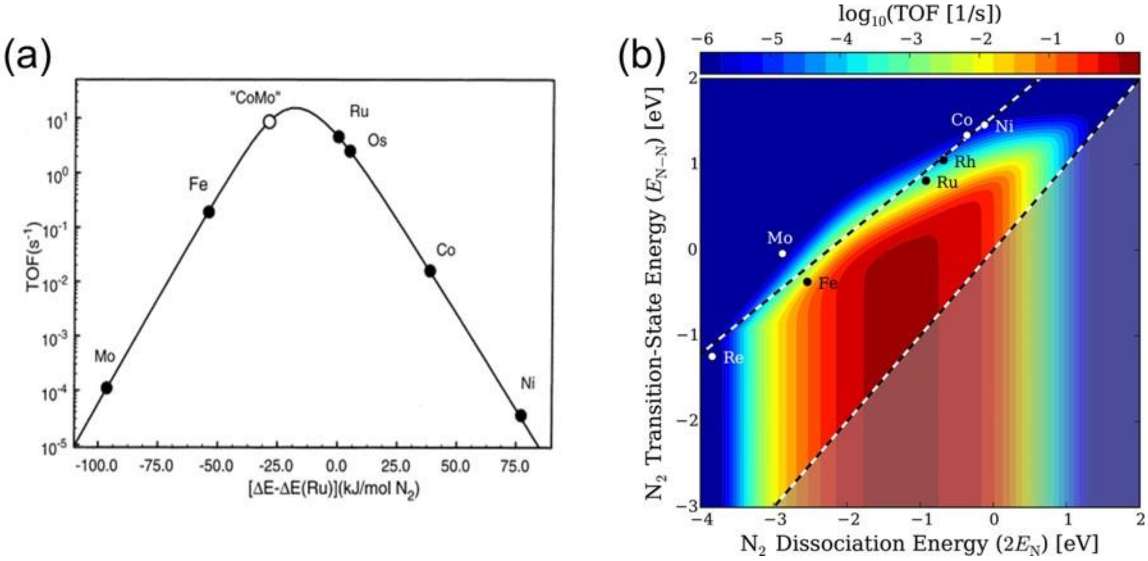

Figure 2.7 (a) Calculated turnover frequencies for ammonia synthesis as a function of the adsorption energy of nitrogen [84]. (b) 2-D activity heat map describing the steady-state turnover frequency (TOF) to NH_3 as a function of N_2 dissociation barrier ($E_{N\text{-}N}$) and N_2 dissociation energy ($2E_N$), Two BEP scaling lines are shown (upper corresponding to stepped transition metal surfaces and lower corresponding to the ideal limit) [85].

Here, using ammonia synthesis as an example, the N_2 dissociation energy on a metal is used as the descriptor to predict the ammonia production activity on a range of transition metal surfaces, as shown in Figure 2.7 (a). In this figure, it can be seen that both Co and Mo are far from the optimal turnover frequencies (TOFs) for ammonia production because N binds either too weak (for Co) or too strong (for Mo). The Co–Mo alloy, enabling N_2 dissociation energy somewhere in between, is predicted to be a much better catalyst than its constituent elements. Jacobsen et al. [84] synthesized Co_3Mo_3N which indeed exhibits much higher ammonia production rates than pure Co and Mo.

2.4.5 Breaking the Scaling Relationship

Long-time study of catalytic trends has also revealed that for many important catalytic reactions, such as oxygen reduction reaction (ORR) and ammonia synthesis on transition metal catalysts, the scaling relationships between key reaction intermediates can be broken and the ‘optimal’ activity can be achieved. For instance, because the energy difference between OH and OOH is separated by 3.2 eV, and always stays intact on any 2D surface due to the intrinsic linear scaling relationship (between OH and OOH), the scaling between OH and OOH has to be broken in order to overcome this major technological barrier in fuel cell development [86, 87]. Another example can be found, again, for ammonia synthesis. Figure 2.7 (b) depicted a 2D ‘volcano’ plot for ammonia synthesis using two descriptors, N_2 dissociation barrier ($E_{N\text{-}N}$) and nitrogen dissociation energy ($2E_N$) over transition metals. The linear BEP relationship between $2E_N$ and $E_{N\text{-}N}$ was shown in upper dashed black–white line. As shown in Figure 2.7 (b), in order to obtain the the optimum catalyst region in red area, efforts have to be devoted into breaking the existed linear scaling relationship. Specific configurations have been tested and a few promising candidates by breaking the scaling relationship are predicted to enhance NH_3 synthesis [85].

Bibliography

[1]. Kohn, W.; Sham, L. J., Self-consistent equations including exchange and correlation effects. *Physical Review* **1965,** 140, (4A), A1133.
[2]. Shan, N.; Zhou, M.; Hanchett, M. K.; Chen, J.; Liu, B., Practical Principles of Density Functional Theory for Catalytic Reaction Simulations on Metal Surfaces – from Theory to Applications. *Molecular Simulation* **2017,** 43, (10-11), 861-885.
[3]. Kittel, C., *Introduction to Solid State Physics*. 7th ed.; John Wiley & Sons: 1996; p 673.
[4]. Monkhorst, H. J.; Pack, J. D., Special Points for Brillouin Zone Integrations. *Physical Review B* **1976,** 13, (12), 5188-5192.
[5]. Gonze, X.; Beuken, J. M.; Caracas, R.; Detraux, F.; Fuchs, M.; Rignanese, G. M.; Sindic, L.; Verstraete, M.; Zerah, G.; Jollet, F.; Torrent, M.; Roy, A.; Mikami, M.; Ghosez, P.; Raty, J. Y.; Allan, D. C., First-principles computation of material properties: the ABINIT software project. *Computational Materials Science* **2002,** 25, (3), 478-492.
[6]. Clark, S. J.; Segall, M. D.; Pickard, C. J.; Hasnip, P. J.; Probert, M. J.; Refson, K.; Payne, M. C., First principles methods using CASTEP. *Zeitschrift Fur Kristallographie* **2005,** 220, (5-6), 567-570.
[7]. Sutton, J. E.; Vlachos, D. G., Building large microkinetic models with first-principles' accuracy at reduced computational cost. *Chemical Engineering Science* **2015,** 121, 190-199.
[8]. Hammer, B.; Hansen, L. B.; Nørskov, J. K., Improved adsorption energetics within density-functional theory using revised Perdew-Burke-Ernzerhof functionals. *Physical Review B* **1999,** 59, (11), 7413-7421.
[9]. Giannozzi, P.; Baroni, S.; Bonini, N.; Calandra, M.; Car, R.; Cavazzoni, C.; Ceresoli, D.; Chiarotti, G. L.; Cococcioni, M.; Dabo, I.; Dal Corso, A.; de Gironcoli, S.; Fabris, S.; Fratesi, G.; Gebauer, R.; Gerstmann, U.; Gougoussis, C.; Kokalj, A.; Lazzeri, M.; Martin-Samos, L.; Marzari, N.; Mauri, F.; Mazzarello, R.; Paolini, S.; Pasquarello, A.; Paulatto, L.; Sbraccia, C.; Scandolo, S.; Sclauzero, G.; Seitsonen, A. P.; Smogunov, A.; Umari, P.; Wentzcovitch, R. M., QUANTUM ESPRESSO: a modular and open-source software project for quantum simulations of materials. *Journal of Physics-Condensed Matter* **2009,** 21, (39).
[10]. Kresse, G.; Hafner, J., Ab initio Molecular Dynamics for Open Shell Transitio Metals. *Physical Review B* **1993,** 48, (17), 13115-13118.
[11]. Kresse, G.; Furthmuller, J., Efficiency of ab-initio total energy calculations for metals and semiconductors using a plane-wave basis set. *Computational Materials Science* **1996,** 6, (1), 15-50.
[12]. Hamann, D. R.; Schluter, M.; Chiang, C., Norm-conserving pseudopotentials. *Physical Review Letters* **1979,** 43, (20), 1494-1497.
[13]. Hamann, D. R., Generalized norm-conserving pseudopotentials. *Physical Review B* **1989,** 40, (5), 2980-2987.
[14]. Vanderbilt, D., Optimally smooth norm-conserving pseudopotentials. *Physical Review B* **1985,** 32, (12), 8412-8415.

[15]. Bachelet, G. B.; Hamann, D. R.; Schluter, M., Pseudopotentials that work - from H to Pu. *Physical Review B* **1982,** 26, (8), 4199-4228.

[16]. Bachelet, G. B.; Schluter, M., Relativistic norm-conserving pseudopotentials. *Physical Review B* **1982,** 25, (4), 2103-2108.

[17]. Kresse, G.; Hafner, J., Norm-conserving and ultrasoft pseudopotentials for first-row and transition-elements. *Journal of Physics-Condensed Matter* **1994,** 6, (40), 8245-8257.

[18]. Vanderbilt, D., Soft self-consistent pseudopotentials in a generalized eigenvalue formalism. *Physical Review B* **1990,** 41, (11), 7892-7895.

[19]. Kresse, G.; Joubert, D., From ultrasoft pseudopotentials to the projector augmented-wave method. *Physical Review B* **1999,** 59, (3), 1758-1775.

[20]. Perdew, J. P.; Schmidt, K., Jacob's Ladder of Density Functional Approximations for the Exchange-Correlation Energy. *AIP Conference Proceedings* **2001,** 577, (1), 1-20.

[21]. Car, R., Density functional theory: Fixing Jacob's ladder. *Nature Chemistry* **2016,** 8, 820.

[22]. Perdew, J. P.; Chevary, J. A.; Vosko, S. H.; Jackson, K. A.; Pederson, M. R.; Singh, D. J.; Fiolhais, C., Atoms, molecules, solids, and surfaces: Applications of the generalized gradient approximation for exchange and correlation. *Physical Review B* **1992,** 46, (11), 6671-6687.

[23]. Perdew, J. P.; Burke, K.; Ernzerhof, M., Generalized Gradient Approximation Made Simple. *Physical Review Letters* **1996,** 77, (18), 3865-3868.

[24]. Perdew, J. P.; Ruzsinszky, A.; Csonka, G. I.; Vydrov, O. A.; Scuseria, G. E.; Constantin, L. A.; Zhou, X.; Burke, K., Restoring the Density-Gradient Expansion for Exchange in Solids and Surfaces. *Physical Review Letters* **2008,** 100, (13), 136406.

[25]. Lee, C.; Yang, W.; Parr, R. G., Development of the Colle-Salvetti correlation-energy formula into a functional of the electron density. *Physical Review B* **1988,** 37, (2), 785-789.

[26]. Becke, A. D., Density-functional exchange-energy approximation with correct asymptotic behavior. *Physical Review A* **1988,** 38, (6), 3098-3100.

[27]. Mavrikakis, M.; Rempel, J.; Greeley, J.; Hansen, L. B.; Nørskov, J. K., Atomic and molecular adsorption on Rh(111). *The Journal of Chemical Physics* **2002,** 117, (14), 6737-6744.

[28]. Hammer, B.; Scheffler, M.; Jacobsen, K. W.; Nørskov, J. K., Multidimensional potential-energy surface for H_2 dissociation over Cu(111). *Physical Review Letters* **1994,** 73, (10), 1400-1403.

[29]. Pederson, M. R., Density-functional based determination of the CH_3-CH_4 hydrogen exchange reaction barrier. *Chemical Physics Letters* **1994,** 230, (1), 54-60.

[30]. Grimme, S., Accurate description of van der Waals complexes by density functional theory including empirical corrections. *Journal of Computational Chemistry* **2004,** 25, (12), 1463-1473.

[31]. Grimme, S.; Antony, J.; Ehrlich, S.; Krieg, H., A Consistent and Accurate Ab initio Parametrization of Density Functional Dispersion Correction (DFT-D) for the 94 Elements H-Pu. *Journal of Chemical Physics* **2010,** 132, (15).

[32]. Tkatchenko, A.; Scheffler, M., Accurate Molecular Van Der Waals Interactions from Ground-State Electron Density and Free-Atom Reference Data. *Physical Review Letters* **2009,** 102, (7), 073005.

[33]. Rydberg, H.; Lundqvist, B. I.; Langreth, D. C.; Dion, M., Tractable nonlocal correlation density functionals for flat surfaces and slabs. *Physical Review B* **2000,** 62, (11), 6997-7006.

[34]. Dion, M.; Rydberg, H.; Schroder, E.; Langreth, D. C.; Lundqvist, B. I., Van der Waals density functional for general geometries. *Physical Review Letters* **2004,** 92, (24), 246401-246404.

[35]. Jiří, K.; David, R. B.; Angelos, M., Chemical Accuracy for the van der Waals Density Functional. *Journal of Physics: Condensed Matter* **2010,** 22, (2), 022201.
[36]. Klimeš, J.; Bowler, D. R.; Michaelides, A., Chemical accuracy for the van der Waals density functional. *Journal of Physics-Condensed Matter* **2010,** 22, (2), 022201-022205.
[37]. Wellendorff, J.; Lundgaard, K. T.; Møgelhøj, A.; Petzold, V.; Landis, D. D.; Nørskov, J. K.; Bligaard, T.; Jacobsen, K. W., Density functionals for surface science: Exchange-correlation model development with Bayesian error estimation. *Physical Review B* **2012,** 85, (23), 235149.
[38]. Morgan, B. J.; Watson, G. W., A Density Functional Theory plus U Study of Oxygen Vacancy Formation at the (110), (100), (101), and (001) Surfaces of Rutile TiO2. *Journal of Physical Chemistry C* **2009,** 113, (17), 7322-7328.
[39]. Di Valentin, C.; Pacchioni, G.; Selloni, A., Reduced and n-Type Doped TiO_2: Nature of Ti^{3+} Species. *Journal of Physical Chemistry C* **2009,** 113, (48), 20543-20552.
[40]. Hu, Z. P.; Metiu, H., Choice of U for DFT plus U Calculations for Titanium Oxides. *Journal of Physical Chemistry C* **2011,** 115, (13), 5841-5845.
[41]. Fabris, S.; de Gironcoli, S.; Baroni, S.; Vicario, G.; Balducci, G., Taming multiple valency with density functionals: A case study of defective ceria. *Physical Review B* **2005,** 71, (4).
[42]. Paier, J.; Penschke, C.; Sauer, J., Oxygen Defects and Surface Chemistry of Ceria: Quantum Chemical Studies Compared to Experiment. *Chemical Reviews* **2013,** 113, (6), 3949-3985.
[43]. Tang, J.-J.; Liu, B., Reactivity of the Fe_2O_3(0001) Surface for Methane Oxidation: A GGA + U Study. *Journal of Physical Chemistry C* **2016,** 120, (12), 6642-6650.
[44]. Dudarev, S. L.; Botton, G. A.; Savrasov, S. Y.; Humphreys, C. J.; Sutton, A. P., Electron-energy-loss spectra and the structural stability of nickel oxide: An LSDA+U study. *Physical Review B* **1998,** 57, (3), 1505-1509.
[45]. Anisimov, V. I.; Zaanen, J.; Andersen, O. K., Band thoery and Mott insulators: Hubbard U instead of Stoner I. *Physical Review B* **1991,** 44, (3), 943-954.
[46]. Anisimov, V. I.; Aryasetiawan, F.; Lichtenstein, A., First-principles calculations of the electronic structure and spectra of strongly correlated systems: the LDA+ U method. *Journal of Physics-Condensed Matter* **1997,** 9, 767-808.
[47]. Wang, L.; Maxisch, T.; Ceder, G., Oxidation energies of transition metal oxides within the GGA + U framework. *Physical Review B* **2006,** 73, (19), 195107.
[48]. Langmuir, I., Part II.—"Heterogeneous reactions". Chemical reactions on surfaces. *Transactions of the Faraday Society* **1922,** 17, 607-620.
[49]. Arnadottir, L.; Stuve, E. M.; Jonsson, H., Adsorption of water monomer and clusters on platinum(111) terrace and related steps and kinks I. Configurations, energies, and hydrogen bonding. *Surface Science* **2010,** 604, (21-22), 1978-1986.
[50]. Fajin, J. L. C.; Cordeiro, M.; Gomes, J. R. B., Adsorption of atomic and molecular oxygen on the au(321) surface: DFT study. *Journal of Physical Chemistry C* **2007,** 111, (46), 17311-17321.
[51]. Carabineiro, S. A. C.; Nieuwenhuys, B. E., Adsorption of small molecules on gold single crystal surfaces. *Gold Bulletin* **2009,** 42, (4), 288-301.
[52]. Bray, J. M.; Schneider, W. F., Potential Energy Surfaces for Oxygen Adsorption, Dissociation, and Diffusion at the Pt(321) Surface. *Langmuir* **2011,** 27, (13), 8177-8186.

[53]. Bray, J. M.; Smith, J. L.; Schneider, W. F., Coverage-Dependent Adsorption at a Low Symmetry Surface: DFT and Statistical Analysis of Oxygen Chemistry on Kinked Pt(321). *Topics in Catalysis* **2014,** 57, (1-4), 89-105.
[54]. Held, G.; Jones, L. B.; Seddon, E. A.; King, D. A., Effect of oxygen adsorption on the chiral Pt{531} surface. *Journal of Physical Chemistry B* **2005,** 109, (13), 6159-6163.
[55]. Rampulla, D. M.; Gellman, A. J.; Sholl, D. S., Bromine atom diffusion on stepped and kinked copper surfaces. *Surface Science* **2006,** 600, (10), 2171-2177.
[56]. Strasser, P.; Koha, S.; Greeley, J., Voltammetric surface dealloying of Pt bimetallic nanoparticles: an experimental and DFT computational analysis. *Physical Chemistry Chemical Physics* **2008,** 10, (25), 3670-3683.
[57]. Chen, Y.; Salciccioli, M.; Vlachos, D. G., An Efficient Reaction Pathway Search Method Applied to the Decomposition of Glycerol on Platinum. *The Journal of Physical Chemistry C* **2011,** 115, (38), 18707-18720.
[58]. Abild-Pedersen, F.; Greeley, J.; Studt, F.; Rossmeisl, J.; Munter, T. R.; Moses, P. G.; Skulason, E.; Bligaard, T.; Nørskov, J. K., Scaling properties of adsorption energies for hydrogen-containing molecules on transition-metal surfaces. *Physical Review Letters* **2007,** 99, (1), 016105-016101.
[59]. Liu, B.; Greeley, J., Decomposition Pathways of Glycerol via C–H, O–H, and C–C Bond Scission on Pt(111): A Density Functional Theory Study. *The Journal of Physical Chemistry C* **2011,** 115, (40), 19702-19709.
[60]. Hammer, B.; Nørskov, J. K., Electronic factors determining the reactivity of metal surfaces. *Surface Science* **1995,** 343, (3), 211-220.
[61]. Hammer, B.; Nørskov, J. K., Why gold is the noblest of all the metals. *Nature* **1995,** 376, (6537), 238-240.
[62]. Hammer, B.; Nørskov, J. K., Theoretical surface science and catalysis - Calculations and concepts. In *Advances in Catalysis, Vol 45: Impact of Surface Science on Catalysis*, Gates, B. C.; Knozinger, H., Eds. 2000; Vol. 45, pp 71-129.
[63]. Liu, B.; Greeley, J., A Density Functional Theory Analysis of Trends in Glycerol Decomposition on Close-Packed Transition Metal Surfaces. *Physical Chemistry Chemical Physics* **2013,** 15, (17), 6475-6485.
[64]. Le, T. H.-M.; Liu, B.; Huynh, L. K., SurfKin: An Ab initio Kinetic Code for Modeling Surface Reactions. *Journal of Computational Chemistry* **2014,** 35, (26), 1890-1899.
[65]. Nørskov, J. K.; Rossmeisl, J.; Logadottir, A.; Lindqvist, L.; Kitchin, J. R.; Bligaard, T.; Jónsson, H., Origin of the Overpotential for Oxygen Reduction at a Fuel-Cell Cathode. *The Journal of Physical Chemistry B* **2004,** 108, (46), 17886-17892.
[66]. Henkelman, G.; Jóhannesson, G.; Jósson, H., Methods for Finding Saddle Points and Minimum Energy Paths. In *Theoretical Methods in Condensed Phase Chemistry*, Kluwer Academic: New York, 2000; Vol. 5, pp 269-300.
[67]. Henkelman, G.; Uberuaga, B. P.; Jonsson, H., A climbing image nudged elastic band method for finding saddle points and minimum energy paths. *Journal of Chemical Physics* **2000,** 113, (22), 9901-9904.
[68]. Mills, G.; Jonsson, H., Quantum and thermal effects in H_2 dissociative adsorption - evaluation of free-energy barriers in multidimensional quantum-systems. *Physical Review Letters* **1994,** 72, (7), 1124-1127.

[69]. Fischer, S.; Karplus, M., Conjugate peak refinement - an algorithm for finding reaction paths and accurate transition-states in systems with many degrees of freedom. *Chemical Physics Letters* **1992,** 194, (3), 252-261.
[70]. Ionova, I. V.; Carter, E. A., Ridge method for finding saddle-points on potential-energy surfaces. *Journal of Chemical Physics* **1993,** 98, (8), 6377-6386.
[71]. Halgren, T. A.; Lipscomb, W. N., Synchronous-transit method for determining reaction pathways and locating molecular transition-states. *Chemical Physics Letters* **1977,** 49, (2), 225-232.
[72]. Henkelman, G.; Jonsson, H., A dimer method for finding saddle points on high dimensional potential surfaces using only first derivatives. *Journal of Chemical Physics* **1999,** 111, (15), 7010-7022.
[73]. Liu, B.; Greeley, J., Decomposition pathways of glycerol via C-H, O-H and C-C bond scission on Pt(111), a density functional theory study. *Journal of Physical Chemistry C* **2011,** 115, 19702-19709.
[74]. Liu, B.; Cheng, L.; Curtiss, L.; Greeley, J., Effects of Van der Waals Density Functional Corrections on Trends in Furfural Adsorption and Hydrogenation on Close-Packed Transition Metal Surfaces. *Surface Science* **2014,** 622, 51-59.
[75]. Groß, A., Reactivity of bimetallic systems studied from first principles. *Topics in Catalysis* **2006,** 37, (1), 29-39.
[76]. Wang, S.; Petzold, V.; Tripkovic, V.; Kleis, J.; Howalt, J. G.; Skulason, E.; Fernandez, E. M.; Hvolbaek, B.; Jones, G.; Toftelund, A.; Falsig, H.; Bjorketun, M.; Studt, F.; Abild-Pedersen, F.; Rossmeisl, J.; Nørskov, J. K.; Bligaard, T., Universal transition state scaling relations for (de)hydrogenation over transition metals. *Physical Chemistry Chemical Physics* **2011,** 13, (46), 20760-20765.
[77]. Wang, S.; Temel, B.; Shen, J.; Jones, G.; Grabow, L. C.; Studt, F.; Bligaard, T.; Abild-Pedersen, F.; Christensen, C. H.; Nørskov, J. K., Universal Brønsted-Evans-Polanyi Relations for C–C, C–O, C–N, N–O, N–N, and O–O Dissociation Reactions. *Catalysis Letters* **2011,** 141, (3), 370-373.
[78]. Nørskov, J. K.; Bligaard, T.; Rossmeisl, J.; Christensen, C. H., Towards the computational design of solid catalysts. *Nature Chemistry* **2009,** 1, (1), 37-46.
[79]. Gokhale, A. A.; Kandoi, S.; Greeley, J. P.; Mavrikakis, M.; Dumesic, J. A., Molecular-level descriptions of surface chemistry in kinetic models using density functional theory. *Chemical Engineering Science* **2004,** 59, (22-23), 4679-4691.
[80]. Mhadeshwar, A. B.; Vlachos, D. G., Microkinetic modeling for water-promoted CO oxidation, water-gas shift, and preferential oxidation of CO on Pt. *Journal of Physical Chemistry B* **2004,** 108, (39), 15246-15258.
[81]. Madon, R. J.; Braden, D.; Kandoi, S.; Nagel, P.; Mavrikakis, M.; Dumesic, J. A., Microkinetic analysis and mechanism of the water gas shift reaction over copper catalysts. *Journal of Catalysis* **2011,** 281, (1), 1-11.
[82]. Stoltze, P.; Nørskov, J. K., An interpretation of the high-pressure kinetics of ammonia-synthesis based on a microscopic model. *Journal of Catalysis* **1988,** 110, (1), 1-10.
[83]. Medford, A. J.; Shi, C.; Hoffmann, M. J.; Lausche, A. C.; Fitzgibbon, S. R.; Bligaard, T.; Nørskov, J. K., CatMAP: A Software Package for Descriptor-Based Microkinetic Mapping of Catalytic Trends. *Catalysis Letters* **2015,** 145, (3), 794-807.

[84]. Jacobsen, C. J. H.; Dahl, S.; Clausen, B. S.; Bahn, S.; Logadottir, A.; Nørskov, J. K., Catalyst design by interpolation in the periodic table: Bimetallic ammonia synthesis catalysts. *Journal of the American Chemical Society* **2001,** 123, (34), 8404-8405.
[85]. Singh, A. R.; Montoya, J. H.; Rohr, B. A.; Tsai, C.; Vojvodic, A.; Nørskov, J. K., Computational Design of Active Site Structures with Improved Transition-State Scaling for Ammonia Synthesis. *ACS Catalysis* **2018,** 8, (5), 4017-4024.
[86]. Koper, M. T. M., Thermodynamic theory of multi-electron transfer reactions: Implications for electrocatalysis. *Journal of Electroanalytical Chemistry* **2011,** 660, (2), 254-260.
[87]. Man, I. C.; Su, H.-Y.; Calle-Vallejo, F.; Hansen, H. A.; Martinez, J. I.; Inoglu, N. G.; Kitchin, J.; Jaramillo, T. F.; Nørskov, J. K.; Rossmeisl, J., Universality in Oxygen Evolution Electrocatalysis on Oxide Surfaces. *Chemcatchem* **2011,** 3, (7), 1159-1165.

Chapter 3 - Electrochemical Reduction of Furfural on Transition Metals

Chapter 3 is adapted with permission from:

Shan, N.; Hanchett, M. K.; Liu, B. “Mechanistic insights evaluating Ag, Pb, and Ni as electrocatalysts for furfural reduction from first-principles methods”, *Journal of Physical Chemistry C*, 2017, 121 (46), 25768–25777.

3.1 Introduction

Furfural has been identified as an important biomass-derived compound for sustainable manufacturing of a variety of bio-chemicals and biofuels, including furfuryl alcohol (FA) and 2-methyfuran (MF) [1-4]. Electrochemical reduction of furfural (ECRFF) to FA and MF, can be carried out at atmospheric pressure and room temperature with non-gaseous hydrogen sources [5, 6], as illustrated in Figure 3.1. This new technology becomes an energy efficient and environmentally advantageous approach compared to thermal furfural reduction routes via heterogeneous hydrogenation and hydrogenolysis [7, 8], which typically require high pressure (0.1–1 MPa), elevated temperature (100–500°C), and H_2 feedstocks that are generated in energy intensive processes. In ECRFF, FA formation is a 2-electron process (Figure 3.1), while furfural-to-MF conversion requires four electrons. The interchange between FA and MF is possible and involves two electrons, thus forming a closed loop.

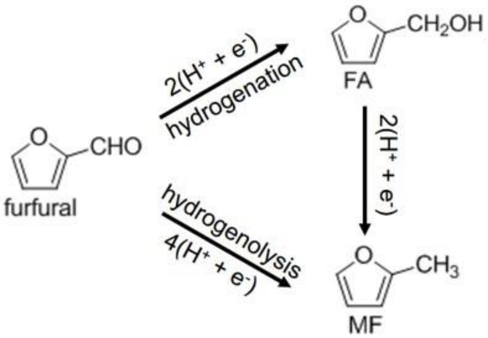

Figure 3.1 Routes for electrochemical reduction of furfural (ECRFF) to furfuryl alcohol (FA) and 2-methylfuran (MF), adapted from Ref [9]. Copyright 2017, American Chemical Society.

The ECRFF product selectivity is strongly linked to the intrinsic properties of the transition metal-based cathodes [5]. Insights into furfural conversion trends can be drawn from studies analogous to CO_2 electrochemical reduction [10, 11], where it has been shown that Cu and its alloys are uniquely selective for small hydrocarbons (e.g., CH_4, CH_3OH) [10, 12, 13]; Au and Ag are more selective for CO yield [14, 15]; and Pb and Sn exhibit strong tendency to produce formic acid [16-19].

In a similar but not parallel manner, Cu has been found to be effective for electrochemically catalyzing furfural, consisting of a C=O bond in its aldehyde group, into MF via hydrogenolysis, while Au, Pt, Ni, and Pb are more selective for FA via hydrogenation to varying degrees [5, 20-25]. Current experimental hypothesis of MF formation considers FA as the intermediate [5, 22, 23]. According to Figure 3.1, in principle, the 4-electron direct furfural-to-MF conversion, parallel to the furfural-to-FA process, is plausible. Although studies on heterogeneous catalysis of furfural to FA and MF on transition metals, such as Cu [26, 27] and Pd [28], exist, molecular-level insights for relevant electrocatalytic furfural conversion remain elusive.

The furan ring with conjugated C–C bonds, which is chemically functional in furfural conversions, adds significant computational challenges to achieve a systematic understanding of furfural reduction compared to CO_2 reduction. Both theoretical and experimental investigations of heterogeneous conversions of furfural suggest that variations in adsorption patterns of furfural and its derivatives on different transition metals, ranging from weak binding on Cu to strong binding on Ir, Ni, Pd, and Pt, play a role in influencing product selectivity [26-34]. For instance, on Cu, the furan ring binds weakly and tilts away from the surface, which is considered beneficial for being selective toward FA (or MF) formation [26, 27, 33]. However, the furan ring binds strongly on Pd and enables decarbonylation, which leads to furan production [28].

In this chapter, molecular mechanisms for furfural electroreduction via hydrogenation and hydrogenolysis on single crystal Ag, Pb, and Ni facets were generated using periodic density functional theory (DFT). Although Cu has long been regarded as a standard material for furfural hydrogenation and hydrogenolysis [26, 27], we evaluated the performance of Ag, Pb, and Ni in order to explore the options as alternative cathode materials for ECRFF. Recent experimental efforts have successfully demonstrated that Pb and Ni can be utilized as economical alternative cathodes to replace noble metals like Pt and Au for FA production [5, 22]. Moreover, the selectivity of MF versus FA can be tuned with electrolytes when Ni electrodes are used [5]. Although there are no direct data so far on Ag being used in ECRFF, Ag has exhibited excellent performance in the conversion of 5-hydroxymethylfurfural (HMF), a chemically analogous compound to furfural, and approximately 100% Faradic Efficiency and selectivity to 2,5-bis(hydroxymethyl)furan have been obtained [35]. Herein, periodic DFT calculations were performed on the close-packed and stepped surfaces of Ag, Pb, and Ni so that the intrinsic thermodynamic and kinetic behaviors associated with FA and MF formations can be understood. Such molecular insights are necessary for eventual deployment of these promising materials for ECRFF.

3.2 Computational Details

All periodic DFT calculations were executed using Vienna *Ab initio* Simulation Package (VASP) [36, 37]. The exchange and correlation energies were described by the Perdew-Burke-Ernzerhof (PBE) functional [38]. An energy cutoff of 340 eV was determined to construct the plane waves. Tests based on furfural adsorption using higher cutoff value have shown that the binding energies have converged to within 0.01 eV. A k-point mesh of 4 × 4 × 1 based on the Monkhorst-pack scheme was used to sample the reciprocal first Brillouin zone [39]. Self-consistent iteration was converged up to 1×10^{-6}. The ionic step was converged when the force on each atom is less than 0.02 eV/Å. The Methfessel-Paxton smearing scheme was used with a Fermi population in the Kohn-Sham states at $k_BT = 0.2$ eV [40]. The total energies were then extrapolated to 0 K. Dipole corrections were included in all calculations.

The (111) and (211) facets of Ag, Pb, and Ni (all face-centered cubic crystals) were adopted to represent the flat close-packed terrace and stepped sites. A $p(4 \times 4)$ unit cell with three layers was used for (111) slab model. The top layer and the adsorbates were allowed to relax, whereas the bottom two layers were fixed at the optimized bulk values at 4.17, 5.05, and 3.52 Å, corresponding to Ag, Pb, and Ni, respectively. These lattice parameters compare satisfactorily with the experimental lattice constants [41]. An orthogonal (3 × 1) unit cell with nine atomic layers was used for the (211) facet, with the bottom six layers fixed to its respective bulk value as well.

It is well recognized that standard GGA functionals are inadequate to describe dispersion effects on molecular adsorptions due to the van der Waals force between adsorbates and substrates [42-45]. Such dispersion effect has been assessed on Cu(111), Pt(111) and Pd(111) using Grimme's D3 [46] method and vdw-DF functionals [47] (i.e., optPBE and optB88) in our previous study [26]. In this work, these van der Waals-correction functionals were also used to optimize furfural, FA, MF, and reaction intermediates on close-packed and stepped Ag, Pb and Ni surfaces.

The vibrational frequencies were calculated using central difference method based on simple harmonic oscillation approximation. These vibrational frequencies were then used to compute zero-point energies (*ZPE*) and free energies (*G*) according to Equation (31) [48],

$$G = E_{DFT} + ZPE - TS, \tag{31}$$

where E_{DFT} denotes the total energy, and *TS* is the entropy term. Only entropy changes stemming from gaseous species (i.e., furfural, FA, and MF) adsorption and desorption were considered. The translational and rotational contributions were included in our estimations. Details of the computation of these contributions are based on standard statistical mechanics treatment and can be found in our previous work [48].

The free energies of ECRFF elementary steps are estimated using the computational hydrogen electrode (CHE) model established by Nørskov et al [49], where the chemical potential of a proton-electron pair ($\mu(H^+ + e^-)$) is equilibrated with the chemical potential of ½H_2 in the gas phase, which can be expressed by Equation (32),

$$\mu(H^+ + e^-) = \frac{1}{2}\mu\left(H_{2(g)}\right) - eU, \tag{32}$$

where e is the elementary charge, and U represents the applied potential bias. For instance, the elementary step for C–H bond formation during the first step of furfural hydrogenation can be written as Equation (33),

$$furfural^{*} + (H^{+} + e^{-}) \rightarrow mh6^{*} \tag{33}$$

where the species with the asterisk (*) indicates an adsorbate on the surface. The free energy change (ΔG) of this step becomes (Equation (34)),

$$\Delta G = G(mh6^{*}) - G(furfural^{*}) - [\frac{1}{2}G(H_{2(g)}) - eU]. \tag{34}$$

The energy barriers for C-O bond cleavage were calculated using the climbing image nudged elastic band (CI-NEB) and dimer methods. The transition states were confirmed by examining that only one single imaginary frequency exists. The energy barriers for hydrogenation steps were estimated using the Brønsted–Evans–Polanyi (BEP) relationship from our previous work [26].

3.3 Mechanistic Insights on Transition Metals

An expanded reaction network detailing ECRFF (Figure 3.1) associated with FA and MF formations is shown in Figure 3. 2. The construction of this network is based on two hydrogenated furfural intermediates: mh6, corresponding to the mono-hydrogenated furfural resulting from C–H bond formation (blue arrows); and mh7, from O–H bond formation (red arrows). The horizontal routes represent the two FA production paths. MF formation originates from furfural and its intermediates are represented by vertical arrows and are labeled in blue, red, and green corresponding to mh6, mh7, and furfural respectively. Moreover, the pathway for FA conversion into MF (diagonal yellow arrows) is included as well.

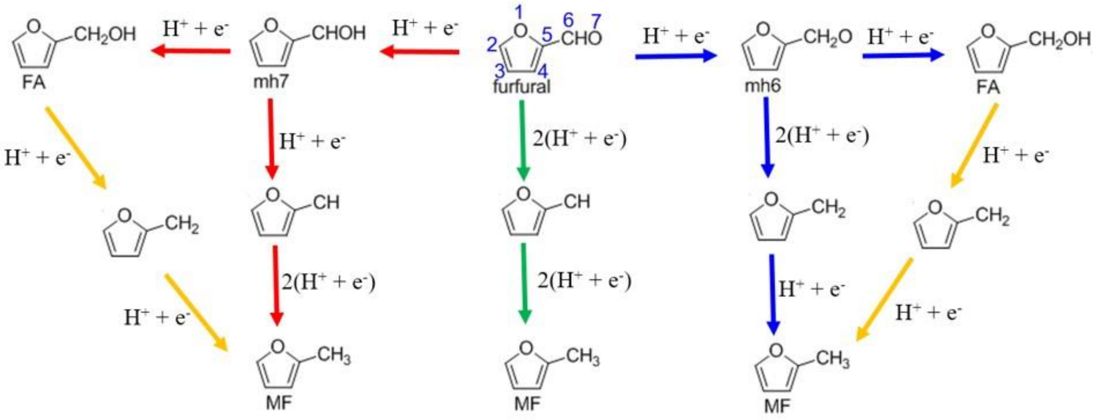

Figure 3.2 Reaction network of furfural conversions into FA and MF for ECRFF, adapted from Ref [9]. Copyright 2017, American Chemical Society.

3.3.1 Molecular Adsorptions on Ag, Pb, and Ni

The binding energies (E_{ads}) for molecular adsorption (furfural, FA, MF, and reaction intermediates) on close-packed Ag, Pb and Ni surfaces are collectively defined by Equation (35),

$$E_{ads} = E_{ads*} - E_{*} - E_{gas}, \tag{35}$$

where E_{ads*}, E_{*}, and E_{gas} represent the total energies of surface adsorbate, clean surface, and gas-phase adsorbate, respectively.

Adsorption geometries of furfural, FA, MF, mh6, and mh7 on Ag(111), Pb(111), and Ni(111), as illustrated in Figure 3.3, were optimized using the optPBE functional. The binding energies are summarized in Table 3.1. The geometry of furfural on Ag(111) is shown in Figure 3.3(a_1), suggesting that furfural binds on one of the top sites with the oxygen located at the end of the aldehyde group. The adsorption of furfural is rather critical for ECRFF. Comparison with furfural adsorption on Cu(111) [26] shows that the up-tilting of the furan ring is an indication of weak binding on silver surfaces. Adsorption energy of furfural on Ag(111), calculated from Equation (35), is -0.62 eV, comparable but slightly weaker than that on Cu(111) [26]. FA binds on Ag(111) via its hydroxyl oxygen (Figure 3.3(a_2)) with a binding energy of -0.74 eV. The MF molecule is almost non-polar and parallel to the surface upon adsorption (Figure 3.3(a_3)), with a binding energy of -0.62 eV. The two mono-hydrogenated intermediates, mh6 and mh7, bind on Ag(111) at the 3-fold and top site by their unsaturated O and C atom, as depicted in Figure 3.3(a_4-a_5), respectively.

On Pb(111), the overall geometry pattern agrees consistently with that on Ag(111), as seen from the second row of Figure 3.3. As shown in Table 3.1, furfural, FA, and MF bind even more weakly on Pb(111) than on Ag(111). On the other hand, mh6 and mh7 bind slightly more strongly on Pb(111) than on Ag(111), i.e., -2.79 eV versus -2.40 eV for mh6, and -0.81 eV versus -0.78 eV for mh7, respectively.

In Figure 3.3(c_1-c_3, and c_5), adsorptions of furfural, FA, MF, and mh7 on Ni(111) exhibit different behaviors. Unlike on Ag(111) and Pb(111), the adsorptions of furfural, FA, and MF take place mainly due to the interactions between their furan rings and the substrate, with expectedly stronger binding energies as well (see Table 3.1). The mh6 still binds on the 3-fold hollow site of Ni(111) with its unsaturated oxygen, as shown in Figure 3.3(c_4). The binding strength of mh7 is contributed by both the unsaturated carbon (in -CHOH) and the furan ring (Figure 3.3(c_5)).

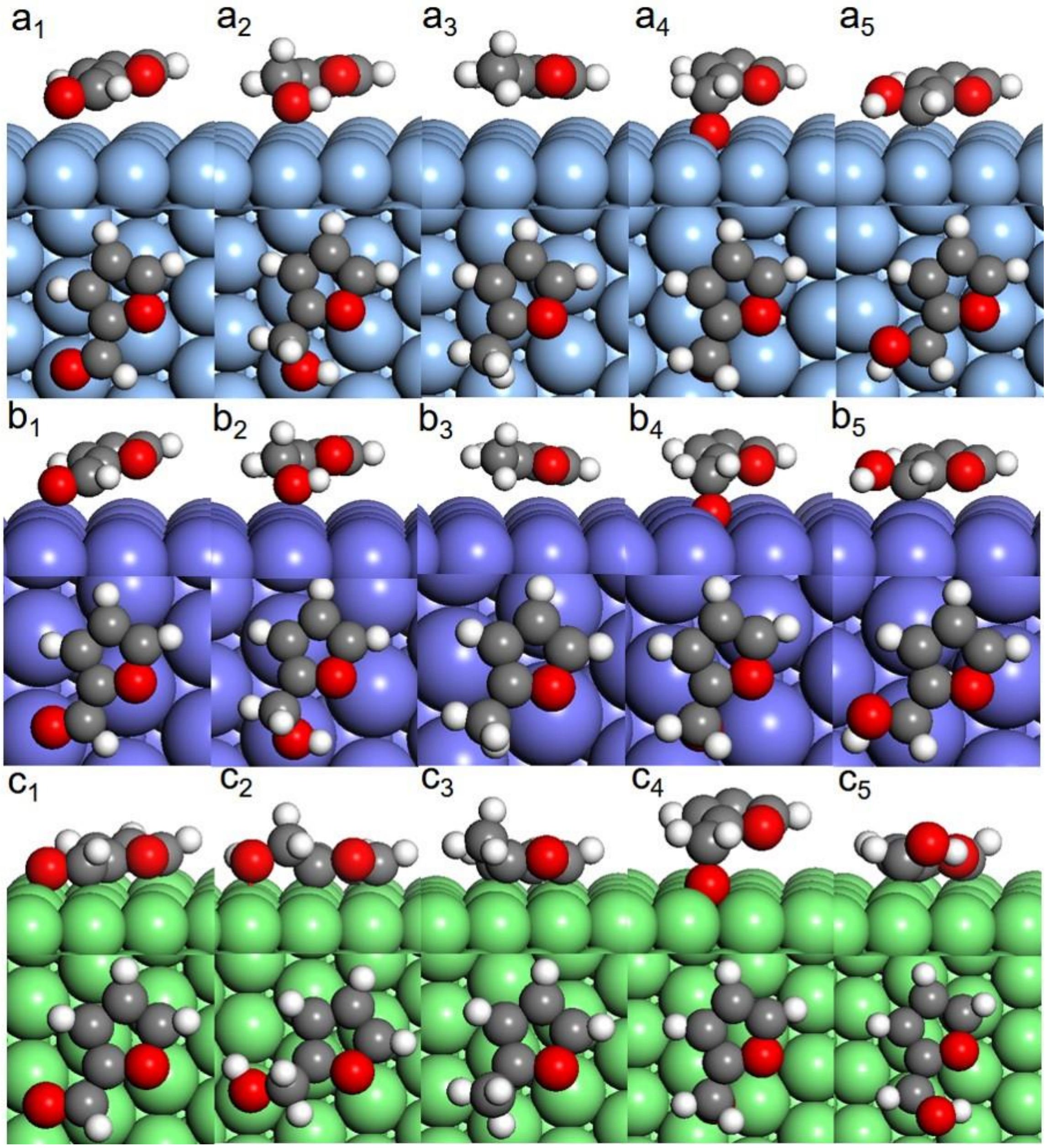

Figure 3.3 Optimized structures of furfural, FA, MF, mh6 and mh7 using optPBE functional, labeled numerically from 1 to 5 from left to right, on Ag(111) (a_1 ~ a_5), Pb(111) (b_1 ~ b_5) and Ni(111) (c_1 ~ c_5). Grey, red, white, blue, purple, and green spheres represent C, O, H, Ag, Pb, and Ni, respectively. Adapted from Ref [9]. Copyright 2017, American Chemical Society.

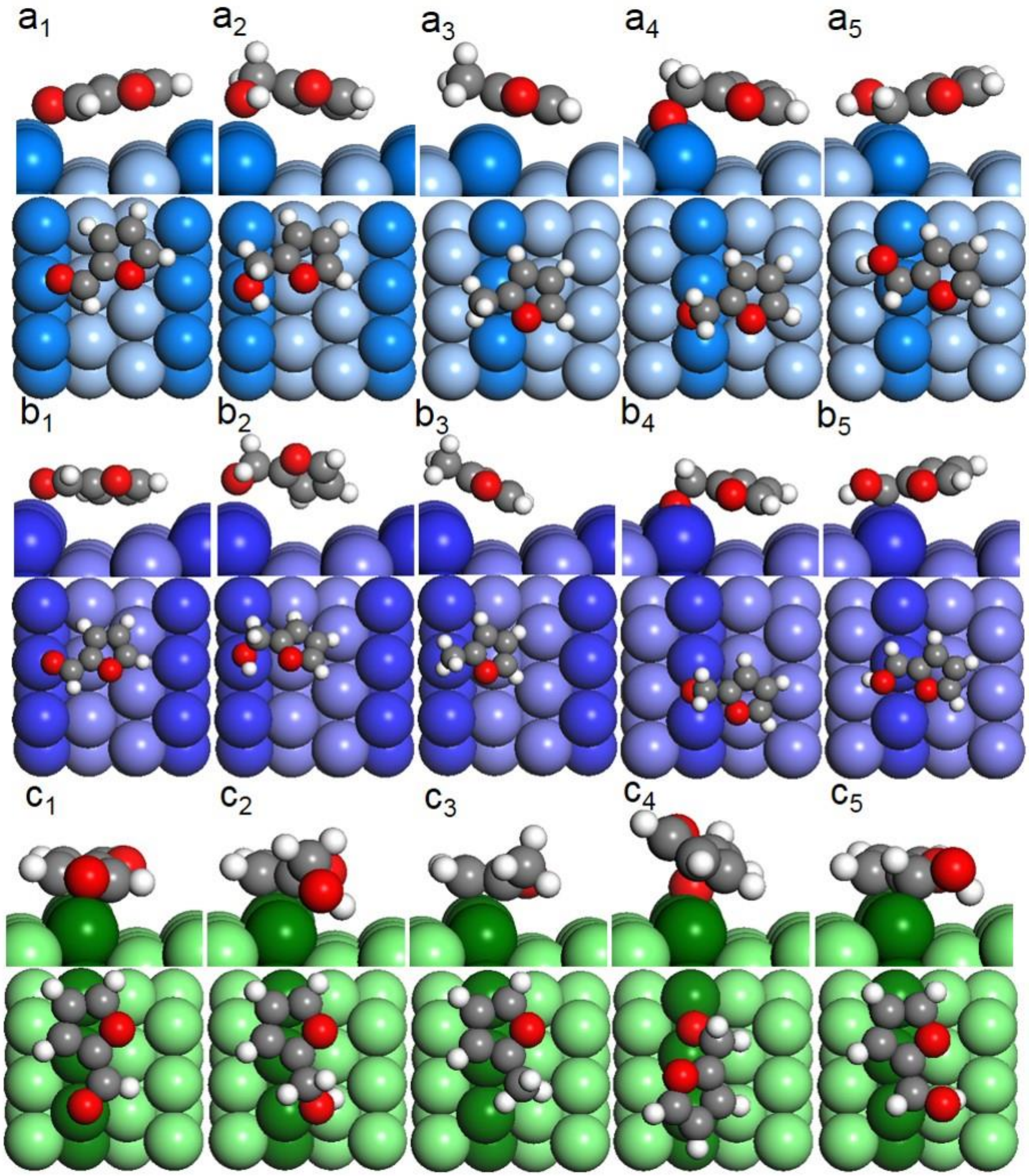

Figure 3.4 Optimized structures of furfural, FA, MF, mh6, and mh7 using optPBE functional, labeled numerically from 1 to 5 from left to right, on Ag(211) (a_1 ~ a_5), Pb(211) (b_1 ~ b_5) and Ni(211) (c_1 ~ c_5). Grey, red, white, blue, purple, and green spheres represent C, O, H, Ag, Pb, and Ni, respectively. The step edges are highlighted. Adapted from Ref [9]. Copyright 2017, American Chemical Society.

Adsorptions on the step sites of Ag, Pb and Ni surfaces were considered using the (211) slab models. The optimized geometries are depicted in Figure 3.4. On Ag(211) and Pb(211), furan rings in furfural, FA, MF, mh6, and mh7 all tilt away without apparent contact with the surface. On Ni(211), on the other hand, furan rings in all species (except mh6) bind at the edge of the Ni(211).

Table 3.1 suggests that adsorptions of all species (including H_2O, OH, and O) become stronger on the stepped Ag(211) and Ni(211) surfaces than on the flat Ag(111) and Ni(111) surfaces. This trend remains for data obtained from optB88 (see Table 3.2). Moreover, it is interesting to note that, except for furfural, adsorptions (e.g., FA, mh6, mh7, f-CH_2, H_2O, OH, O) on Pb(211) have generally remained the same or even weaker than that on Pb(111). Using optB88, adsorptions of all species become weaker (Table 3.2).

Table 3.1 Binding energies (in eV) on Ag, Pb, and Ni based on the optPBE functional. Adapted from Ref [9]. Copyright 2017, American Chemical Society.

	Ag(111)	Ag(211)	Pb(111)	Pb(211)	Ni(111)	Ni(211)
furfural	-0.62	-0.86	-0.57	-0.66	-1.33	-2.27
FA	-0.74	-0.81	-0.60	-0.57	-1.12	-2.00
MF	-0.62	-0.67	-0.50	-0.50	-0.94	-1.69
mh6	-2.40	-2.65	-2.79	-2.70	-3.20	-3.63
mh7	-0.78	-0.88	-0.81	-0.59	-1.95	-2.73
[a]f-CH	-2.36	-2.63	-2.45	-2.45	-3.87	-4.20
[a]f-CH_2	-0.95	-1.17	-1.06	-0.93	-2.05	-2.69
H_2O	-0.26	-0.37	-0.23	-0.22	-0.41	-0.66
OH	-2.80	-2.89	-3.20	-3.14	-3.50	-3.95
O	-3.88	-4.13	-5.19	-5.00	-5.74	-5.66

[a] Letter ‘f’ represents the furan ring.

An evaluation of various treatments of van der Waals corrections is shown in Figure 3.5, summarizing binding energies of furfural, FA, MF, mh6, and mh7 obtained using the PBE, PBE-D3, optPBE, and optB88 functionals. Solidly filled columns represent binding energies on (111) surfaces, whereas the hatched columns are for (211). All the binding energies obtained using PBE-D3 and optB88 functionals are also listed in Table 3.2.

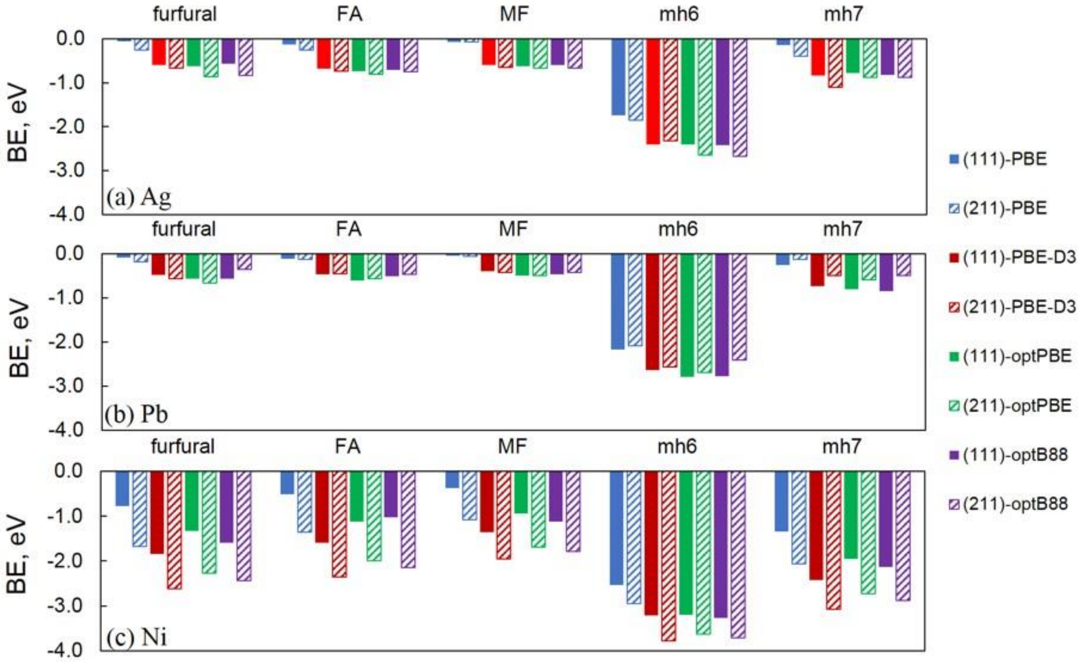

Figure 3.5 DFT calculated binding energies ($\boldsymbol{E_{ads}}$), according to Equation 35, of furfural, FA, MF, mh6, and mh7 on (a) Ag, (b) Pb, and (c) Ni (solid–(111), hatched–(211)) surfaces using PBE (blue), PBE-D3 (red), optPBE (green), and optB88 (purple) functionals. Adapted from Ref [9]. Copyright 2017, American Chemical Society.

According to Figure 3.5, it can be noted that the GGA-PBE functional (blue columns) indeed underestimates binding energies to the extent up to 1 eV. Furthermore, on both (111) and (211) facets of Ag and Pb (Figure 3.5(a-b)), with van der Waals corrections being included, binding energies become insensitive to the theory used. In the present study, variations within approximately 0.2 eV have been observed (Table 3.1–3.2). A similar trend has been noticed in our previous work on Cu(111) [26].

On Ni(111) and Ni(211), as shown in Figure 3.5(c), larger fluctuations of binding energies are observed among different functionals. For instance, adsorption energies of furfural computed using PBE-D3, optPBE, and optB88 may vary in a range of 0.5 eV on both Ni(111) and Ni(211). Nevertheless, adsorption configurations obtained from different theories vary to a much lesser extent, which has been noted on Pd(111) and Pt(111) surfaces previously [26]. In this work, calculations based on the optPBE functional were chosen to generate free energy diagrams for ECRFF on Ag, Pb and Ni presented in the following section.

3.3.2 Brønsted–Evans–Polanyi (BEP) Relationship for C-O Bond Cleavage

First-principles calculations of transition state (TS) search involving biomass-derived compounds, which typically consist of multiple functional groups such as furfural, can be notoriously challenging and computationally intensive [26, 50]. Our previous work has successfully established a BEP relationship for furfural hydrogenation steps on Cu, Pd, and Pt [26], which will continue to be employed in this work. Likewise, a BEP relationship, for C-O bond cleavages has been developed in a similar manner and is shown in Figure 3.6. The energy barriers for representative C–O bond cleavage reactions involving mh6 (square), mh7 (circle), furfural (triangle), and FA (diamond), on Cu (red), Ag (blue), Pb (purple) and Ni (green), were first calculated using CI-NEB and dimer methods using the GGA-PBE functional, and then used for the linear fitting. The identified transition states structures are shown in Figure A.1, and numerical barrier values are listed in Table A.1.

Table 3.2 Binding Energies (in eV) on Ag, Pb and Ni Surfaces Obtained Using optB88 and PBE-D3 Functionals. Adapted from Ref [9]. Copyright 2017, American Chemical Society.

		Ag(111)	Ag(211)	Pb(111)	Pb(211)	Ni(111)	Ni(211)
optB88	furfural	-0.57	-0.83	-0.57	-0.35	-1.59	-2.44
	FA	-0.70	-0.75	-0.51	-0.46	-1.02	-2.15
	MF	-0.59	-0.66	-0.47	-0.42	-1.13	-1.79
	mh6	-2.42	-2.67	-2.78	-2.41	-3.27	-3.71
	mh7	-0.82	-0.87	-0.84	-0.49	-2.13	-2.88
	[a]f-CH	-2.08	-2.32	-2.15	-2.13	-3.65	-3.92
	[a]f-CH$_2$	-0.99	-1.20	-1.08	-0.87	-2.25	-2.85
	H_2O	-0.22	-0.31	-0.20	-0.18	-0.42	-0.66
	OH	-2.82	-2.93	-3.21	-3.16	-3.62	-4.03
	O	-3.98	-4.25	-5.30	-5.12	-5.92	-5.80
PBE-D3	furfural	-0.59	-0.66	-0.48	-0.56	-1.85	-2.62
	FA	-0.68	-0.73	-0.46	-0.45	-1.59	-2.36
	MF	-0.59	-0.65	-0.39	-0.43	-1.36	-1.95
	mh6	-2.41	-2.32	-2.64	-2.56	-3.22	-3.78
	mh7	-0.83	-1.11	-0.74	-0.50	-2.43	-3.08
	[a]f-CH	-2.45	-2.70	-2.36	-2.43	-4.07	-4.34
	[a]f-CH$_2$	-1.06	-1.21	-1.03	-0.91	-2.50	-3.05
	H_2O	-0.31	-0.45	-0.20	-0.25	-0.49	-0.77
	OH	-2.87	-2.93	-3.15	-3.08	-3.59	-4.03
	O	-3.96	-4.18	-5.09	-4.96	-5.83	-5.75

[a] Letter ‘f’ represents furan ring.

In Figure 3.6, E_{FS} denotes the final state energy of an elementary step written in the exothermic direction, and E_{TS} represents the transition state energy, both using the reactants in the gas phase and clean surface as the energy reference. It can be noted that a linear relationship (the black dashed line) exists between E_{FS} and E_{TS} for C-O bond cleavage on Cu, Ag, Pb, and Ni at their respective terrace and stepped surfaces. The slope and intersection are 0.95 (dimensionless) and 1.01 eV, respectively. The mean absolute error (MAE) is 0.22 eV for the fitting.

It is worth to point out that only data obtained from the GGA-PBE functional were used to generate the BEP relationship. Data from optPBE (denoted with P) and optB88 (denoted with B) functionals are included in Figure 3.6 in order to validate the transferability of this BEP relationship. Based on the agreement shown in Figure 3.6, we can conclude that energy barriers calculated from the optPBE and the optB88 functional in this work also follow the same BEP relationship. Also, it is notable that (111) and (211) surfaces followed the same BEP relationship. The reason can be attributed to similar transition state geometries on close-packed and stepped surfaces (shown in Figure A.1).

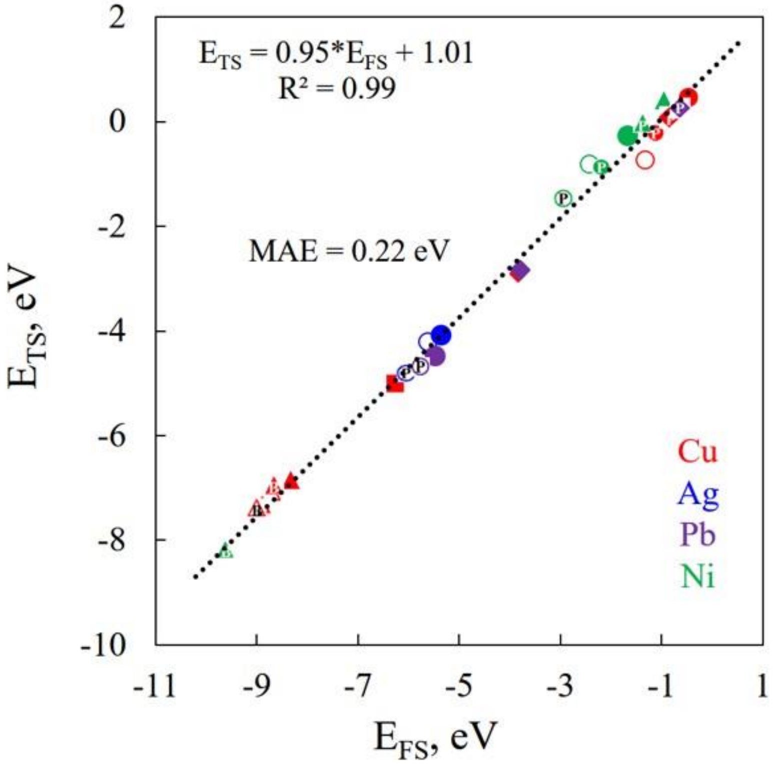

Figure 3.6 BEP relationship (black dashed line) for C-O bond cleavage of mh6 (square), mh7 (circle), furfural (triangle), and FA (diamond) on Cu (red), Ag (blue), Pb (purple) and Ni (green), using the GGA-PBE functional. Solid symbols are data obtained on (111) surfaces, while hollow symbols are data obtained from (211) surfaces. The data obtained from different functional, i.e., optPBE and optB88, were labeled with letters P and B, respectively. Adapted from Ref [9]. Copyright 2017, American Chemical Society.

3.3.3 Free Energies of Furfural Electrochemical Reduction

The elementary steps for ECRFF are listed as R1–R10. All reactions start with the adsorption of furfural (R1). As shown in Figure 3.2, the two FA production pathways via mh6 and mh7 correspond to R2 and R3. The three MF formation pathways via mh6, mh7, and the direct furfural C-O bond cleavage are presented by R4–R6. Conversion of FA to MF is shown by R7. FA, MF, and H_2O desorption are represented by R8, R9, and R10, respectively.

$$\text{furfural (gas)} + * \rightarrow \text{furfural}^* \tag{R1}$$

$$\text{furfural}^* \xrightarrow{H^+ + e^-} \text{mh6}^* \xrightarrow{H^+ + e^-} \text{FA}^* \tag{R2}$$

$$\text{furfural}^* \xrightarrow{H^+ + e^-} \text{mh7}^* \xrightarrow{H^+ + e^-} \text{FA}^* \tag{R3}$$

$$\text{furfural}^* \xrightarrow{H^+ + e^-} \text{mh6}^* \xrightarrow{\text{C-O bond cleavage}} \text{f-CH}_2{}^* + \text{O}^* \xrightarrow{3(H^+ + e^-)} \text{MF}^* + \text{H}_2\text{O}^* \tag{R4}$$

$$\text{furfural}^* \xrightarrow{H^+ + e^-} \text{mh7}^* \xrightarrow{\text{C-O bond cleavage}} \text{f-CH}^* + \text{OH}^* \xrightarrow{3(H^+ + e^-)} \text{MF}^* + \text{H}_2\text{O}^* \tag{R5}$$

$$\text{furfural}^* \xrightarrow{\text{C-O bond cleavage}} \text{f-CH}^* + \text{O}^* \xrightarrow{4(H^+ + e^-)} \text{MF}^* + \text{H}_2\text{O}^* \tag{R6}$$

$$\text{FA}^* \xrightarrow{\text{C-O bond cleavage}} \text{f-CH}_2{}^* + \text{OH}^* \xrightarrow{2(H^+ + e^-)} \text{MF}^* + \text{H}_2\text{O}^* \tag{R7}$$

$$\text{FA}^* \rightarrow * + \text{FA (gas)} \tag{R8}$$

$$\text{MF}^* \rightarrow * + \text{MF (gas)} \tag{R9}$$

$$\text{H}_2\text{O}^* \rightarrow * + \text{H}_2\text{O (gas)} \tag{R10}$$

The free energies of all these elementary steps are summarized in Figure 3.7 (a-f). These free energies are estimated at 298 K, 1 atm, and 0 V (no applied potential). Clean surface, gas phase furfural, and the proton-electron pair are used as the zero energy reference. Reaction thermodynamics (ΔG) calculations adopt a similar proton coupled electron transfer (PCET) approach introduced by Rossmeisl and Skulason et al. [51-53] In this work, reaction energy barriers are explicitly included in our discussion, and the barriers of hydrogenation were obtained directly using the BEP relationship in Ref [26] while the barriers describing C-O bond cleavage steps either from explicit DFT calculations (if available) or the best estimations from BEP (Figure 3.6) were used. It should be pointed out that electrochemical factors related to solvents and surface charge are not included in this analysis, therefore, the presented thermodynamic and kinetic properties can be considered solely intrinsic to the metals.

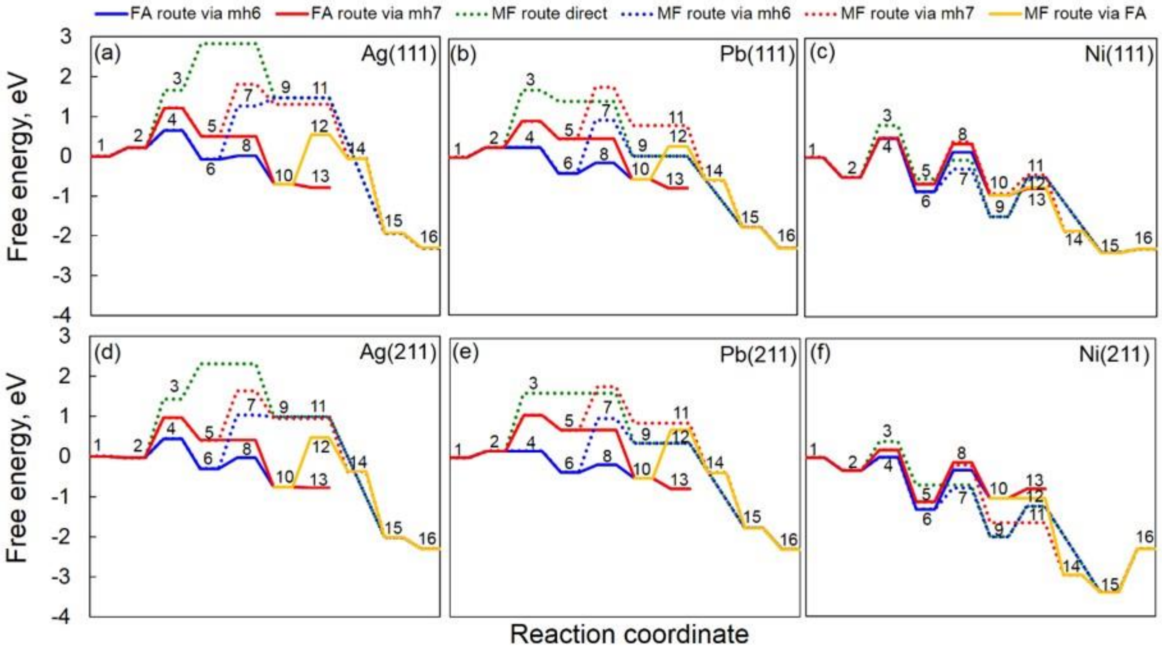

Figure 3.7 ECRFF free energy diagrams on (a) Ag(111), (b) Pb(111), (c) Ni(111), (d) Ag(211), (e) Pb(211), and (f) Ni(211) at 298 K, 1 atm, and 0 V. Elementary steps are labeled as follows: (1) furfural (gas), proton, and clean surface; (2) furfural*; (3) TS - furfural C-O bond cleavage; (4) TS for C–H formation; (5) mh7*; (6) mh6*; (7) TS for C-O bond cleavage; (8) TS for C-H bond formation; (9) f-CH_2* + O*; (10) FA*; (11) TS for C-H bond formation; (12) TS for FA C-O bond cleavage; (13) FA (gas); (14) f-CH_2* + OH*; (15) MF * + H_2O*; (16) MF (gas) + H_2O (gas). Adapted from Ref [9]. Copyright 2017, American Chemical Society.

3.3.3.1 Furfural Conversion on Ag(111)

On Ag(111) (Figure 3.7(a)), furfural adsorption (Step 1→2) is endothermic (at 0 V) with an adsorption free energy of 0.21 eV. The mh6 formation step (Step 2→6) is exothermic, while the parallel mh7 formation step (Step 2→5) is endothermic. In addition, the energy barrier associated with the mh6 formation is also lower than that for mh7 formation (i.e., 0.44 eV vs. 1.0 eV). The second hydrogenation step producing FA is much facile for both mh6 and mh7 intermediates. Therefore, on Ag(111), the overall free energy profile for the mh6 route (solid blue line) appears to be more favorable than the mh7 route, and should be regarded as the competitive pathway for FA production. The desorption energy for FA on Ag(111) surface is -0.09 eV. The first hydrogenation step (Step 2→6) would be rate limiting.

As shown in Figure 3.7(a), it is possible that furfural, mh6, and mh7 are all capable of undergoing C-O bond cleavages necessary for MF formation (dotted lines). In all MF production routes, the C-O bond cleavage step should be the rate-limiting step as they are consistently located at the highest part of the free energy diagram. The direct route where the C–O bond cleavage in furfural (green dotted line) is regarded as the least favorable path for MF formation due to a substantial energy barrier of 1.45 eV (Step 3). For partially hydrogenated furfural intermediates, C-O bond cleavages are facilitated, as respective energy barriers for mh6 and mh7 become 1.33 and 1.31 eV (Step 7). Hence, for MF formation, the mh6 route (blue dotted line) should be more favorable compared to the mh7 route (red dotted line). Upon the C-O bond cleavage, the remaining steps for MF formation on Ag(111) will be facile, with negligible barriers according to BEP estimations.

Moreover, a barrier of 1.23 eV is found for direct FA dissociation via the C–O bond cleavage in the -CH_2OH group to produce MF (Step 12 shown in yellow solid line in Figure 3.7(a)).

This energy barrier is significantly higher than the FA desorption energy from Ag(111), suggesting that this pathway would be infeasible as an intermediate step for MF formation on Ag(111).

An overall analysis of the free energy diagram (Figure 3.7(a)) concludes that MF production is likely to be hindered by the kinetics of C-O bond cleavage, although it is thermodynamically more favorable. It should be pointed out that Goddard et al. [54] recently showed, based on first-principles modeling, protons in aqueous solutions are quite capable of protonating the C–O bond in CO electroreduction intermediates and then cleaving the C–O bond at a much lower barrier.

3.3.3.2 Furfural Conversion on Pb(111)

On Pb(111), as shown in Figure 3.7(b), the free energy of furfural adsorption (Step 1→2) is 0.25 eV, weaker compared to the same step on Ag(111). The formation of mh6 is exothermic (-0.66 eV), and proceeds with an almost negligible energy barrier. On the other hand, the formation of mh7 is endothermic (0.22 eV), with an energy barrier of 0.66 eV. Therefore, the mh6 formation is, again, both thermodynamically and kinetically more favorable than mh7 formation. To complete the second hydrogenation step, mh6 needs to overcome an energy barrier of 0.26 eV. Although the hydrogenation of mh7 proceeds with a negligible barrier (~0 eV), the overall free energy of the mh7 pathway is still too high to be competitive against the mh6 pathway. The desorption energy of FA on Pb(111) surface is -0.22 eV. Unlike Ag(111), the rate-limiting step for FA formation on Pb(111) appears to be furfural adsorption due to the low energy barrier of first hydrogenation to mh6.

On Pb(111), the C-O bond cleavage steps are still the rate-limiting steps for MF production. Respective C-O bond scission barriers for mh6 and mh7 are 1.34 eV and 1.31 eV. On the other hand, the direct path has an energy barrier of 1.45 eV. Therefore, a similar conclusion can be drawn that the mh6 route is the most competitive MF production route.

For FA conversion into MF, an energy barrier of 0.84 eV is required to break the C–O bond, again, much high than the desorption energy of FA. Recent results obtained by Schröder et al. [5] have shown that the selectivity of FA is higher than MF on Pb cathode, which supports the findings shown in Figure 3.7(b).

3.3.3.3 Furfural Conversion on Ni(111)

On Ni(111), the adsorption of furfural is exothermic (-0.50 eV) due to the strong binding with its furan ring (Figure 3.3(c_1)). The two hydrogenation steps, producing mh6 and mh7, are comparable with similar energy barriers of 0.98 and 0.99 eV, respectively. The produced mh6 is slightly more stable than mh7 on Ni(111). In the second hydrogenation step, a barrier of 1.0 eV is required for both mh6 and mh7 to form FA. As shown in Figure 3.7(c), unlike Ag(111) and Pb(111), both mh6 and mh7 routes can be competitive for FA formation on Ni(111).

On Ni(111), the direct route for MF formation needs to overcome a barrier of 1.30 eV to cleave the C–O bond, while the barriers of C-O bond cleavage for mh6 and mh7 are 0.57 and 1.05 eV, respectively. After the C-O bond cleavage, the energy barriers of subsequent hydrogenation steps to obtain MF are 0.47 and 1.00 eV, respectively. As shown in Figure 3.7(c), it is noteworthy to mention that all the routes for MF formation become competitive, MF formation can now even compete against FA formation. Such a behavior indicates that the eventually ECRFF product selectivity could be sensitive to experimental conditions, such as surface coverage, solvent, and electrolyte used. Experimental observations confirmed that the ECRFF product selectivity tends to show more variations on Ni as well [5, 22].

It can also be observed that FA desorption becomes endothermic with a desorption energy of 0.17 eV. Compared to a small barrier of 0.20 eV for FA to break its C–O bond (Step 12) on Ni(111), the channel for FA-to-MF conversion can be open, thus enabling FA to be an intermediate for MF formation.

3.3.3.4 Furfural Conversions on the Stepped Ag, Pb, and Ni Surfaces

It is known that the stepped surface sites tend to exhibit higher activities than terrace sites. Hence, the free energy diagrams of ECRFF on the (211) facets of Ag, Pb, and Ni are shown in Figure 3.7(d-f), respectively. For the stepped Ag surface, electroreduction free energies shift down -0.25 eV due to stronger furfural adsorption. However, no appreciable gains in C–O bond cleavage was observed on Ag(211) (see Table A.1). The mh6 route is still more favorable than the mh7 route for both FA and MF productions, with the first hydrogenation step and the C-O bond cleavage being the rate-limiting steps for respective FA for MF formation. Again, the FA-to-MF conversion will not be competitive since FA will prefer to desorb from Ag(211) as well.

On Pb(211), furfural adsorption is still endothermic despite stronger binding than on Pb(111). The FA production via mh6 proceeds with a lower energy barrier on Pb(211) than on Pb(111) (0.19 eV versus 0.26 eV). As on Ag(211), the stepped Pb surface does not improve C-O bond scission. The pathways involving mh6 remain as the competitive paths for both FA and MF productions. The FA-to-MF conversion route, with an energy barrier of 1.22 eV for C-O bond cleavage compared to the FA desorption (-0.26 eV), will not be feasible on Pb(211).

All intermediates bind stronger on Ni(211) than on Ni(111). As shown in Figure 3.7(f), the formation of mh6 is enhanced kinetically with a reduced hydrogenation barrier of 0.33 eV from 0.98 eV. Moreover, an energy barrier of 0.52 eV for mh7 formation on Ni(211) is also lower than that of 0.99 eV on Ni(111). Hence, on Ni(211), the mh6 route actually becomes more favorable than the mh7 route for FA formation. Both the energy barriers for C-O bond cleavage and for subsequent hydrogenation steps leading to MF are lower on Ni(211) than on Ni(111). Unlike Ag and Pb, the FA-to-MF pathway will be feasible due to negligible C–O bond cleavage barrier, indicating that FA is likely an intermediate for MF production on Ni(211).

3.4 Conclusions

In this chapter, the potential of Ag, Pb, and Ni as electrocatalysts for ECRFF were evaluated by examining the FA and MF production routes using periodic DFT calculations. On all metal surfaces, multiple and parallel pathways leading to FA and MF have been modeled. A BEP relationship for C-O bond cleavage for furfural reduction to MF has also been established and used to estimate the energy barriers. Although the MF formation thermochemistry is favored over FA formation, the C–O bond cleavage barrier will likely hinder the reaction kinetics. Furthermore, the stepped surface does not necessarily promote C–O bond cleavage by lowering the reaction energy barrier.

Two key furfural hydrogenation intermediates, mh6 and mh7, are proven to be critical by influencing overall ECRFF activity and product selectivity. The mh6 intermediate is shown to be a common intermediate to produce both FA and MF and often guide the reaction as the more thermodynamically and kinetically favorable path. Hence, mh6 could be considered as an important descriptor to monitor the trends of ECRFF. Both mh6 and mh7 routes are competitive on Ni because of the strong interaction between the furan ring and Ni surface. Overall, the first hydrogenation step and the C-O bond cleavage are confirmed as likely rate-limiting steps for FA and MF formation. On Ag and Pb, FA is likely to desorb instead of participating further reaction to form MF due to the much higher C-O bond cleavage barrier. However, the FA-to-MF route becomes feasible pathway on Ni because the C–O bond cleavage energy barrier becomes comparable to FA desorption energy.

3.5 Acknowledgements

This work was supported by Start-up funding provided by Kansas State University. DFT calculations were performed thanks to the supercomputing resources and services from the Center for Nanoscale Materials (CNM) supported by the Office of Science of the US Department of Energy under the contract No. DE-AC02-06CH11357, the Beocat Research Cluster at Kansas State University, which is funded in part by NSF grants CNS-1006860 and the National Energy Research Scientific Computing Center (NERSC) under the contract No. DE-AC02-05CH11231.

Bibliography

[1]. Li, X.; Jia, P.; Wang, T., Furfural: A Promising Platform Compound for Sustainable Production of C_4 and C_5 Chemicals. *ACS Catalysis* **2016,** 6, 7621-7640.
[2]. Mariscal, R.; Maireles-Torres, P.; Ojeda, M.; Sadaba, I.; Lopez Granados, M., Furfural: A Renewable and Versatile Platform Molecule for the Synthesis of Chemicals and Fuels. *Energy & Environmental Science* **2016,** 9, (4), 1144-1189.
[3]. Lange, J.-P.; van der Heide, E.; van Buijtenen, J.; Price, R., Furfural-A Promising Platform for Lignocellulosic Biofuels. *ChemSusChem* **2012,** 5, (1), 150-166.
[4]. Huber, G. W.; Iborra, S.; Corma, A., Synthesis of Transportation Fuels from Biomass: Chemistry, Catalysts, and Engineering. *Chemical Reviews* **2006,** 106, (9), 4044-4098.
[5]. Nilges, P.; Schröder, U., Electrochemistry for Biofuel Generation: Production of Furans by Electrocatalytic Hydrogenation of Furfurals. *Energy & Environmental Science* **2013,** 6, (10), 2925-2931.
[6]. Jung, S.; Biddinger, E. J., Electrocatalytic Hydrogenation and Hydrogenolysis of Furfural and the Impact of Homogeneous Side Reactions of Furanic Compounds in Acidic Electrolytes. *ACS Sustainable Chemistry & Engineering* **2016,** 4, (12), 6500-6508.
[7]. Li, F.; Cao, B.; Ma, R.; Liang, J.; Song, H.; Song, H., Performance of Cu/TiO_2-SiO_2 Catalysts in Hydrogenation of Furfural to Furfuryl Alcohol. *The Canadian Journal of Chemical Engineering* **2016,** 94, (7), 1368-1374.
[8]. Kotbagi, T. V.; Gurav, H. R.; Nagpure, A. S.; Chilukuri, S. V.; Bakker, M. G., Highly Efficient Nitrogen-doped Hierarchically Porous Carbon Supported Ni Nanoparticles for the

Selective Hydrogenation of Furfural to Furfuryl Alcohol. *RSC Advances* **2016,** 6, (72), 67662-67668.

[9]. Shan, N.; Hanchett, M. K.; Liu, B., Mechanistic insights evaluating Ag, Pb, and Ni as electrocatalysts for furfural reduction from first-principles methods. *Journal of Physical Chemistry C* **2017,** 121, (46), 25768-25777.

[10]. Hori, Y.; Kikuchi, K.; Murata, A.; Suzuki, S., Production of Methane and Ethylene in Electrochemical Reduction of Carbon Dioxide at Copper Electrode in Aqueous Hydrogencarbonate Solution. *Chemistry Letters* **1986**, (6), 897-898.

[11]. Hori, Y.; Wakebe, H.; Tsukamoto, T.; Koga, O., Electrocatalytic Process of CO Selectivity in Electrochemical Reduction of CO_2 at Metal Electrodes in Aqueous Media. *Electrochimica Acta* **1994,** 39, (11), 1833-1839.

[12]. Watanabe, M.; Shibata, M.; Kato, A.; Azuma, M.; Sakata, T., Design of Alloy Electrocatalysts for CO_2 Reduction: III. The Selective and Reversible Reduction of on Cu Alloy Electrodes. *Journal of the Electrochemical Society* **1991,** 138, (11), 3382-3389.

[13]. Peterson, A. A.; Nørskov, J. K., Activity Descriptors for CO_2 Electroreduction to Methane on Transition-Metal Catalysts. *Journal of Physical Chemistry Letters* **2012,** 3, (2), 251-258.

[14]. Zhu, W.; Michalsky, R.; Metin, Ö.; Lv, H.; Guo, S.; Wright, C. J.; Sun, X.; Peterson, A. A.; Sun, S., Monodisperse Au Nanoparticles for Selective Electrocatalytic Reduction of CO_2 to CO. *Journal of the American Chemical Society* **2013,** 135, (45), 16833-16836.

[15]. Rosen, J.; Hutchings, G. S.; Lu, Q.; Rivera, S.; Zhou, Y.; Vlachos, D. G.; Jiao, F., Mechanistic Insights into the Electrochemical Reduction of CO_2 to CO on Nanostructured Ag Surfaces. *ACS Catalysis* **2015,** 5, (7), 4293-4299.

[16]. Choi, S. Y.; Jeong, S. K.; Kim, H. J.; Baek, I.-H.; Park, K. T., Electrochemical Reduction of Carbon Dioxide to Formate on Tin–Lead Alloys. *ACS Sustainable Chemistry & Engineering* **2016,** 4, (3), 1311-1318.

[17]. Lee, C. H.; Kanan, M. W., Controlling H^+ vs CO_2 Reduction Selectivity on Pb Electrodes. *ACS Catalysis* **2015,** 5, (1), 465-469.

[18]. Koleli, F.; Atilan, T.; Palamut, N.; Gizir, A. M.; Aydin, R.; Hamann, C. H., Electrochemical reduction of CO_2 at Pb- and Sn-electrodes in a fixed-bed reactor in aqueous K_2CO_3 and $KHCO_3$ media. *Journal of Applied Electrochemistry* **2003,** 33, (5), 447-450.

[19]. Azuma, M.; Hashimoto, K.; Hiramoto, M.; Watanabe, M.; Sakata, T., Electrochemical Reduction of Carbon Dioxide on Various Metal Electrodes in Low-Temperature Aqueous $KHCO_3$ Media. *Journal of the Electrochemical Society* **1990,** 137, (6), 1772-1778.

[20]. Albert, W. C.; Lowy, A., The Electrochemical Reduction of Furfural. *Journal of the Electrochemical Society* **1939,** 75, (1), 367-375.

[21]. Parpot, P.; Bettencourt, A. P.; Chamoulaud, G.; Kokoh, K. B.; Belgsir, E. M., Electrochemical Investigations of the Oxidation–reduction of Furfural in Aqueous Medium: Application to Electrosynthesis. *Electrochimica Acta* **2004,** 49, (3), 397-403.

[22]. Li, Z.; Kelkar, S.; Lam, C. H.; Luczek, K.; Jackson, J. E.; Miller, D. J.; Saffron, C. M., Aqueous Electrocatalytic Hydrogenation of Furfural Using a Sacrificial Anode. *Electrochimica Acta* **2012,** 64, 87-93.

[23]. Zhao, B.; Chen, M.; Guo, Q.; Fu, Y., Electrocatalytic Hydrogenation of Furfural to Furfuryl Alcohol Using Platinum Supported on Activated Carbon Fibers. *Electrochimica Acta* **2014,** 135, 139-146.

[24]. Green, S. K.; Lee, J.; Kim, H. J.; Tompsett, G. A.; Kim, W. B.; Huber, G. W., The Electrocatalytic Hydrogenation of Furanic Compounds in a Continuous Electrocatalytic Membrane Reactor. *Green Chemistry* **2013,** 15, (7), 1869-1879.
[25]. Wang, F.; Xu, M.; Wei, L.; Wei, Y.; Hu, Y.; Fang, W.; Zhu, C. G., Fabrication of La-doped TiO_2 Film Electrode and Investigation of Its Electrocatalytic Activity for Furfural Reduction. *Electrochimica Acta* **2015,** 153, 170-174.
[26]. Liu, B.; Cheng, L.; Curtiss, L.; Greeley, J., Effects of Van der Waals Density Functional Corrections on Trends in Furfural Adsorption and Hydrogenation on Close-Packed Transition Metal Surfaces. *Surface Science* **2014,** 622, 51-59.
[27]. Shi, Y.; Zhu, Y.; Yang, Y.; Li, Y.-W.; Jiao, H., Exploring Furfural Catalytic Conversion on Cu(111) from Computation. *ACS Catalysis* **2015,** 5, (7), 4020-4032.
[28]. Vorotnikov, V.; Mpourmpakis, G.; Vlachos, D. G., DFT Study of Furfural Conversion to Furan, Furfuryl Alcohol, and 2-Methylfuran on Pd(111). *ACS Catalysis* **2012,** 2, (12), 2496-2504.
[29]. Xiong, K.; Wan, W.; Chen, J. G., Reaction Pathways of Furfural, Furfuryl alcohol and 2-methylfuran on Cu(111) and NiCu Bimetallic Surfaces. *Surface Science* **2016,** 652, 91-97.
[30]. Pang, S. H.; Medlin, J. W., Adsorption and Reaction of Furfural and Furfuryl Alcohol on Pd(111): Unique Reaction Pathways for Multifunctional Reagents. *ACS Catalysis* **2011,** 1, (10), 1272-1283.
[31]. Sitthisa, S.; An, W.; Resasco, D. E., Selective Conversion of Furfural to Methylfuran over Silica-Supported NiFe Bimetallic Catalysts. *Journal of Catalysis* **2011,** 284, (1), 90-101.
[32]. Sitthisa, S.; Pham, T.; Prasomsri, T.; Sooknoi, T.; Mallinson, R. G.; Resasco, D. E., Conversion of Furfural and 2-methylpentanal on Pd/SiO_2 and $Pd\text{-}Cu/SiO_2$ Catalysts. *Journal of Catalysis* **2011,** 280, (1), 17-27.
[33]. Sitthisa, S.; Sooknoi, T.; Ma, Y.; Balbuena, P. B.; Resasco, D. E., Kinetics and Mechanism of Hydrogenation of Furfural on Cu/SiO_2 Catalysts. *Journal of Catalysis* **2011,** 277, (1), 1-13.
[34]. Wan, W. M.; Jenness, G. R.; Xiong, K.; Vlachos, D. G.; Chen, J. G. G., Ring-Opening Reaction of Furfural and Tetrahydrofurfuryl Alcohol on Hydrogen-Predosed Iridium(111) and Cobalt/Iridium(111) Surfaces. *Chemcatchem* **2017,** 9, (9), 1701-1707.
[35]. Roylance, J. J.; Kim, T. W.; Choi, K.-S., Efficient and Selective Electrochemical and Photoelectrochemical Reduction of 5-Hydroxymethylfurfural to 2,5-Bis(hydroxymethyl)furan using Water as the Hydrogen Source. *ACS Catalysis* **2016,** 6, (3), 1840-1847.
[36]. Kresse, G.; Hafner, J., Ab initio Molecular Dynamics for Open Shell Transitio Metals. *Physical Review B* **1993,** 48, (17), 13115-13118.
[37]. Kresse, G.; Furthmuller, J., Efficiency of *Ab initio* Total Energy Calculations for Metals and Semiconductors using A Plane-wave Basis Set. *Computational Materials Science* **1996,** 6, (1), 15-50.
[38]. Perdew, J. P.; Burke, K.; Ernzerhof, M., Generalized Gradient Approximation Made Simple. *Physical Review Letters* **1996,** 77, (18), 3865-3868.
[39]. Monkhorst, H. J.; Pack, J. D., Special Points for Brillouin Zone Integrations. *Physical Review B* **1976,** 13, (12), 5188-5192.
[40]. Methfessel, M.; Paxton, A. T., High-precision Sampling for Brillouin-zone Integration in Metals. *Physical Review B* **1989,** 40, (6), 3616-3621.
[41]. Kittel, C., *Introduction to Solid State Physics*. 7th ed.; John Wiley & Sons: 1996.
[42]. Margenau, H., Van der waals forces. *Reviews of Modern Physics* **1939,** 11, (1), 1-35.

[43]. Shan, N.; Zhou, M.; Hanchett, M. K.; Chen, J.; Liu, B., Practical Principles of Density Functional Theory for Catalytic Reaction Simulations on Metal Surfaces – from Theory to Applications. *Molecular Simulation* **2017,** 43, (10-11), 861-885.
[44]. Tonigold, K.; Groß, A., Adsorption of Small Aromatic Molecules on the (111) Surfaces of Noble Metals: A Density Functional Theory Study with Semiempirical Corrections for Dispersion Effects. *The Journal of Chemical Physics* **2010,** 132, (22), 224701.
[45]. Bilić, A.; Reimers, J. R.; Hush, N. S.; Hoft, R. C.; Ford, M. J., Adsorption of Benzene on Copper, Silver, and Gold Surfaces. *Journal of Chemical Theory and Computation* **2006,** 2, (4), 1093-1105.
[46]. Grimme, S., Semiempirical GGA-type Density Functional Constructed with A Long-range Dispersion Correction. *Journal of Computational Chemistry* **2006,** 27, (15), 1787-1799.
[47]. Jiří, K.; David, R. B.; Angelos, M., Chemical Accuracy for the van der Waals Density Functional. *Journal of Physics: Condensed Matter* **2010,** 22, (2), 022201.
[48]. Le, T. H.-M.; Liu, B.; Huynh, L. K., SurfKin: An Ab initio Kinetic Code for Modeling Surface Reactions. *Journal of Computational Chemistry* **2014,** 35, (26), 1890-1899.
[49]. Nørskov, J. K.; Rossmeisl, J.; Logadottir, A.; Lindqvist, L.; Kitchin, J. R.; Bligaard, T.; Jónsson, H., Origin of the Overpotential for Oxygen Reduction at a Fuel-Cell Cathode. *The Journal of Physical Chemistry B* **2004,** 108, (46), 17886-17892.
[50]. Liu, B.; Greeley, J., Decomposition Pathways of Glycerol via C–H, O–H, and C–C Bond Scission on Pt(111): A Density Functional Theory Study. *The Journal of Physical Chemistry C* **2011,** 115, (40), 19702-19709.
[51]. Man, I. C.; Su, H. Y.; Calle-Vallejo, F.; Hansen, H. A.; Martinez, J. I.; Inoglu, N. G.; Kitchin, J.; Jaramillo, T. F.; Nørskov, J. K.; Rossmeisl, J., Universality in Oxygen Evolution Electrocatalysis on Oxide Surfaces. *Chemcatchem* **2011,** 3, (7), 1159-1165.
[52]. Rossmeisl, J.; Chan, K.; Skúlason, E.; Björketun, M. E.; Tripkovic, V., On the pH dependence of electrochemical proton transfer barriers. *Catalysis Today* **2016,** 262, 36-40.
[53]. Abghoui, Y.; Garden, A. L.; Howalt, J. G.; Vegge, T.; Skúlason, E., Electroreduction of N_2 to Ammonia at Ambient Conditions on Mononitrides of Zr, Nb, Cr, and V: A DFT Guide for Experiments. *ACS Catalysis* **2016,** 6, (2), 635-646.
[54]. Cheng, T.; Xiao, H.; Goddard, W. A., Free-Energy Barriers and Reaction Mechanisms for the Electrochemical Reduction of CO on the Cu(100) Surface, Including Multiple Layers of Explicit Solvent at pH 0. *The Journal of Physical Chemistry Letters* **2015,** 6, (23), 4767-4773.

Chapter 4 - Glycerol Adsorption at the Metal-Water Interface

Chapter 4 is adapted with permission from:

Shan, N.; Liu, B. “Elucidating molecular interactions in glycerol adsorption at the metal-water interface with density functional theory”, *Langmuir*, 2019, Article ASAP with DOI: 10.1021/acs.langmuir.8b02385.

4.1 Introduction

Driven by the quest for sustainable fuels and chemicals, biomass-derived glycerol [1-5] and furanic compounds [6-8] are listed as key platform compounds. Glycerol, a C3 polyol consisting of three hydroxyl groups, exhibits an extremely versatile utility [9, 10]. Boosted by biodiesel production, glycerol production has nearly doubled during the period of 2001-2011 [11], and is expected to quadruple by 2025 [12]. Already a marketable chemical, the economic appeal strengthens the driving force for glycerol as an affordable feedstock for value-added commodities [12].

As summarized in recent reviews [2, 9, 10], hydrogen, propanediols (PDOs), glyceraldehyde, dihydroxyacetone, and numerous alcohols, and organic acids can be obtained through catalytic transformations of glycerol. Aqueous phase reforming (APR) has been demonstrated to be a viable route for hydrogen production at 498 – 543K and 25 – 50 bar, as illustrated in Figure 4.1 [13]. Platinum is a very effective glycerol APR catalyst, exhibiting promising hydrogen yield (~68%) [14] and selectivity (up to ~75%) [13]. Over Pt, cleavage of glycerol C–H, O–H, and C–C bonds, leading to hydrogen and CO or CO_2 (if coupled with water-gas shift reaction), are promoted, while routes involving C–O bond cleavage (producing alcohols and alkanes) are suppressed at the same time [15, 16]. Glycerol reforming pathways are sensitive to the intrinsic properties of transition metals. For instance, the C-O bond cleavage is promoted on Rh [17] and Ru [18], over which hydrogenolysis becomes the pre-dominant route at 80 bar and 473K. Hence, understanding key elementary steps during glycerol conversion is an integral part in the technological innovation of sustainable fuels and chemicals production based on this raw material.

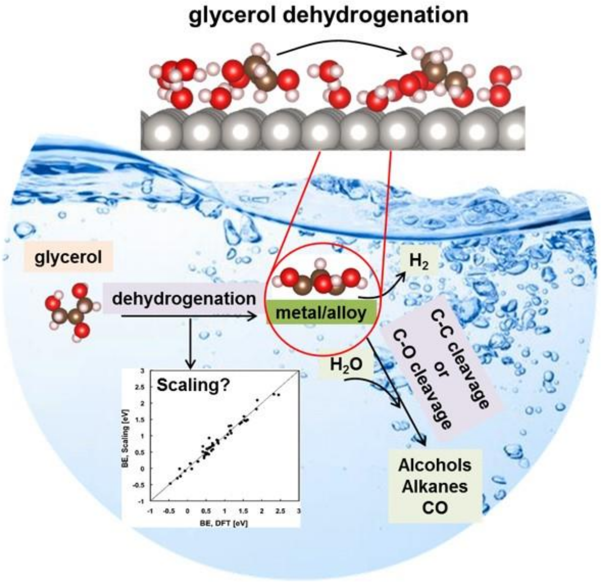

Figure 4.1 Glycerol conversions to chemicals on transition metals in aqueous phase. Adapted with permission from Ref [19]. Copyright 2018, American Chemical Society.

Both experimental and theoretical mechanistic deductions involving glycerol face challenges from multiple parallel reaction pathways including dehydrogenation, hydrogenolysis, or oxidation [9]. The identified pathways from independent quantum mechanical studies are in satisfactory agreements with experimental observations [15-17, 20-24], despite relatively simple models (uniform low-index single crystal active sites, simplified chemical environment) are used.

At 500 K and elevated pressure (> 25 bar), glycerol processing occurs in the liquid phase, with water being one of the most used solvents. Thus, water is intricately involved by modulating adsorption and desorption of chemical species, and transporting key reaction intermediates in-between environment and catalytic active sites. The significance of water in bulk solution and at the interface has long been recognized [25-28]. Specifically for catalytic reactions, the participating water is capable of modifying both reaction energetics and transition state energies in oxygen reduction reaction (ORR) [29, 30], NH_3 synthesis [31], electrochemical CO_2 reduction [32-34], and so on. For oxygenated hydrocarbons, Zope et al. [35] showed that ethanol oxidation on gold actually utilizes hydroxide ions generated from OOH in aqueous solutions rather than molecular oxygen via directly using isotopic $^{18}O_2$ and $H_2{}^{18}O$ probes.

Various theory and models have been proposed and implemented to enrich the toolset for implicit or explicit solvent structure description. The most recent progress has enabled first-principles methods to account for water overlayers or bulk solution phase at an unprecedented scale. In this work, relevant theoretical developments and outcome will be discussed. As can be seen, the literature survey has exposed that acquiring a full molecular perspective on the catalysis associated with glycerol remains extremely challenging because: (1) first-hand information on molecular interactions between adsorbate, solvent, and substrate for the construction of representative models is very elusive; and (2) the inevitable model sizes are too large for standard first-principles modeling approach.

Glycerol and its derivatives on metal surfaces in solvent-free systems are shown to follow empirical formulations derived from approximate bond-order conservation concepts, known as the scaling relationship [15, 16, 20, 36]. In the study, periodic density functional theory (DFT) calculations were employed primarily to reveal and to characterize the water-adsorbate, water-metal, and water-water interactions on well-defined metal-liquid interfaces–a step forward to directly tackle the molecular structures at the water-metal interface and to offer insights that could improve the efficiency to analyze a class of adsorbed oxygenated species.

4.1.1 Solvation Models

4.1.1.1 Implicit Solvation Models

In implicit solvation models, solute molecules in the dielectric medium are commonly treated as being immersed in a ‘solvent cavity’. If the continuum dielectric medium is considered as isotropic, the implicit solvation method is an appealing approach to lower the computational cost by reducing the total degrees of freedom of the system [25, 26]. The electrostatic contribution to the overall solvation free energy can be obtained numerically by discretizing the Poisson differential operator. Care should be given to the shape and size of such cavity, which should be able to reproduce the shape of the solute molecule to minimize distortions of the solvation field: too large cavities will dampen the solvation effects, while too small cavity may result in errors in interaction energy calculations at the solute-solvent interface. Comprehensive reviews of implicit solvation methods, including the rule to determine appropriate cavity, are presented by Tomasi, Cramer, and their coworkers [25, 26]. The so-called conductor-like screening model (a.k.a COSMO [37]) is a close family to the popular polarizable continuum model (PCM) [25], and has been successfully integrated into commercial softwares such as ADF [38]. To account for non-electrostatic effects, COSMO for real solvents (i.e., COSMO-RS) has been recently developed to compute solvation free energies of neutral solutes.

In an implicit solvation setting, Jeong et al. [39] obtained the conformational preference of glycerol at the M06-2Z/cc-pvtz level of theory in aqueous phase. It is shown that glycerol exists as an ensemble of many feasible configurations due to the weakened intramolecular hydrogen bonding. This is a contrast to the glycerol's gas phase configuration, in which glycerol strongly prefers the existence of an intramolecular hydrogen bonding between two terminal hydroxyl groups [15].

An implicit solvation scheme compatible to the Kohn-Sham framework was introduced by Fattebert and Gygi [40, 41], where the electrostatic energy term in the Hohenberg-Kohn formulation is revised using solution of the Poisson equation. Theory such as JDFT by Arias et al. [42] has been developed to study solid surfaces in solution. Hennig and coworkers [43, 44] implemented a self-consistent scheme, as in VASPsol, to account for both electrostatic and non-electrostatic (e.g., dispersion) effects on extended and discrete solid-liquid interface. Most recently, Garcia-Ratés and López [45] succeeded in developing a multigrid continuum model (i.e., MGCM), implemented in the Vienna *ab initio* Simulation Package (VASP), to compute the energetics of adsorbed water and methanol in solutions. With the newly developed MGCM, it is shown that the trend for methanol and water adsorption on Pt(111) can be reversed whether or not the implicit solvation is included [45].

Given the available methods for implicit solvation treatments, Deskins et al. [46] studied the adsorption of 41 species (i.e., C, O, S, N, CH_x, NH_x, etc.) on Pt(111) using three implicit models (i.e., VASPsol, JDFTx, and COSMO), and found that the absolute solvation energy values indeed vary. However, the relative solvation effect remains consistent. Despite the computational advantages, the description of the structural and dynamic properties of a solvated system might be inadequate due to the inherent treatment of the solvent in implicit solvation models. In many catalytic processes, the liquid phase is more than just a dielectric continuum background, as solvent molecules in the liquid phase often participate in chemical reactions.

4.1.1.2 Explicit Solvation Models

Full explicit solvation models describing adsorbed molecular species on solid surfaces require supercells filled with water molecules. In fact, solute-solvent interactions are often limited to within one solvation shell, resulting in a large portion of computing resource being used to account for the degrees of freedoms associated with solvent-solvent interactions. Thus, hybrid solvation models, blending the implicit treatments to account for interactions indirectly contributing to chemisorption, can be an effective way to improve computational efficiency. A schematic representation of various contributions to the adsorption of an immersed adsorbate (denoted as $E_{ads(aq)}$) on a metal surface is illustrated in Figure 4.2, where water-adsorbate, water-water, and water-metal interactions are explicitly indicated at the metal-water interface.

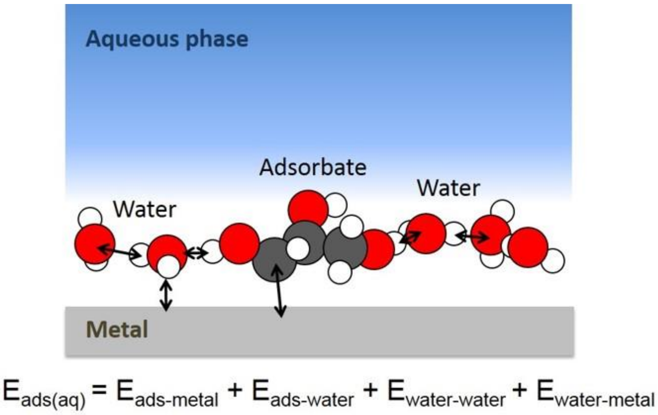

Figure 4.2 Schematic illustration of contributions to adsorptions of glycerol and derived intermediates on metal substrate in aqueous phase. Adapted with permission from Ref [19]. Copyright 2018, American Chemical Society.

For heterogeneous catalytic processes occurring at the interface, the direct interactions that require explicit modeling most likely take place in close proximity of the adsorbate and the surface as illustrated in Figure 4.2. Ice-like water bilayer models covering metal slabs are regarded representative to mimic water-metal interface for periodic DFT calculations. To a great extent, the rationale behind such models can be traced back to surface science studies of water structures on solid surfaces. Over thirty year ago, work by Thiel and Madey [47] revealed that the water structure on metal can be described as a ‘buckled’ bilayer arranged as hexagons with half of the water molecules binding directly on the surface. Aided by XPS and XAS, Ogasawara et al. [48] reported a flat water bilayer on Pt(111). Absorption spectroscopy obtained at low temperature (e.g., 84 K) further showed that water binds on Pt through the oxygen lone pair. The strong lateral interaction through hydrogen bonding is a main mechanism responsible for water clustering [49]. In Carrasco and Michaelides’ recent review [50], high resolution experimental STM and DFT calculations represent a powerful combination to gain molecular insights into behaviors of water clusters (including monomer, dimer, trimer, tetramer, and hexamer), as well as 1-D, 2-D, and 3-D water networks on the surface. With access to atomic-scale resolution measurements on well-defined surfaces, it becomes easier to build representative molecular models, and paves the way to develop more sophisticated molecular modeling.

With the accumulation of experimental data, the early bilayer theory is being challenged as the water overlayer configurations are actually quite diverse. Over Pt(111), configurations with mixed pentagonal, hexagonal, and heptagonal water rings have been observed through high-resolution STM and later confirmed by DFT calculations [51, 52].

The wetting behavior is another indicator of the interaction between water overlayer and metal surfaces. On Pt, adsorbed water molecules remain largely intact. On the other hand, water dissociation is known to occur on Ru(0001) [53]. On Cu(110), 2-D water structure is also shown to consist of hydroxyl groups from partial dissociation of water, at a molar ratio of $H_2O:OH = 2:1$ [54]. Schnur and Groß [27] showed that the presence of metal substrates add substantial polarization on the water overlayer. Also, some metastable states of the overlayer are stabilized. As shown by Neurock and coworkers [28], it takes 0.16 – 0.3 eV for water bilayer to overcome the energy barrier to switch from the 'up' orientation to the 'down' orientation.

The ordered water overlayer above the metal surface can be perturbed by adsorbates. For instance, with pre-adsorbed H atoms on Pt(111), it has been shown that the water bilayer moves away from the surface [27]. Also, a greater order has been predicted, especially when compared to the overlayer directly above Pt(111) without the pre-adsorbed hydrogen atoms. This observation indicates that, near the water-metal interface, solvent structures are influenced by competing water–water and water-metal interactions.

Understanding the influence of water on adsorbate is a key interest for modeling of catalytic process in the aqueous phase. On bimetallic Pt-Ru (111), Desai and Neurock [55] pointed out that although the active site (Ru) responsible for water dissociation is unaffected without the inclusion of explicit solvent molecules, the dissociation step becomes more energetically favorable (0.27 eV) compared to that without the presence of accompanying water molecules (0.55 eV). This suggests that the product state, with dissociated H and OH, is stabilized to a greater extent. Moreover, the transition-state complex structure can also be stabilized as the activation energy is lowered from 1.09 eV in the vapor phase to 0.28 eV.

Extended analysis from the stabilization of a single elementary state to the entire reaction pathway would provide a more faithful description of the thermodynamic landscape in the solvated environment. Taking CO_2 electroreduction as an example, Peterson and co-workers have proposed that, in the solvent-free environment, the formation of formyl group (CHO), rather than COH, is the electrochemical potential limiting step for CH_4 production [56-58]. With a water bilayer model, Shi and Nørskov [59] also showed that CHO is more stable than COH, which is also independently confirmed by Jónsson and Skúlason [60, 61]. However, the energy barrier for CHO formation via CO protonation in the water-assisted H shuttling mechanism invoked by the explicit solvent model is higher [33, 62]. On the other hand, under the consideration of the water-assisted H shuttling, it has been found that the O-H bond formation barrier, as in CO-to-COH, is noticeably lowered [33]. Because a specific geometric orientation facilitating proton transfer is required, implicit solvation models are inadequate. Therefore, many proton transfer processes (e.g., hydrogen evolution [63], hydrogen oxidation [64], and protonation) necessitate explicit solvation modeling.

To further reduce the cost of computation required by explicit solvation modeling, models describing solvation effect using few water molecules in direct contact with adsorbates have been suggested [33, 65, 66]. Sautet et al. [67] pointed out that the intramolecular hydrogen bonds within the carbon skeleton and intermolecular hydrogen bond formed between water-adsorbate can modulate the reactivity of O-H or C-O bond dissociations for adsorbed alcohols.

The extent of solvation based on the use of a finite number of water molecules has to be verified. Based on methanol adsorption, Garcia-Ratés et al. [68] identified different roles of water molecules surrounding methanol. The water molecule in direct coordination with the hydroxyl group provides the main source of stabilization of adsorbed alcohol; however, such coordination could also limit the binding of the hydroxyl group to the surface. For water molecules away from the hydroxyl group, there is a residual effect on the decomposition pathway of methanol. As a tradeoff, Garcia-Ratés et al. [68] proposed a hybrid model that contains two water molecules explicitly coordinating with the adsorbed methanol, and further increase of the number of water molecules will not improve the model. Solvent elsewhere can be treated as a continuum medium using MGCM discussed in the previous section (as illustrated in Figure 4.2) [45].

4.1.2 Molecular Adsorption and Linear Scaling Relationship

In order to decipher the chemistries for glycerol conversion, the ability to identify key intermediates associated with respective dehydrogenation, hydrogenolysis, or oxidation pathways efficiently is crucial [9]. Modeling of catalytic conversion of glycerol using first-principles is already challenged by the large number of reaction intermediates in a pool of 80 species (based on dehydrogenation chemistry alone) [15].

In the past few years, the adsorption patterns of chemisorbed glycerol ($C_3H_8O_3$) and its various dehydrogenenation intermediates on several transition metal and metal alloys have been studied using periodic DFT calculations [15, 16]. The oxygenated hydrocarbons considered under this scope also include methanol (CH_3OH), ethylene glycol (a C2 polyol), and erythritol (a C4 polyol), as well as their C-H and O-H bond scission intermediates. The structures of mono-dehydrogenated intermediates ($C_3H_7O_3$, i.e., glycerol minus one hydrogen atom), as well as glyceraldehyde, and dihydroxyacetone (glycerol minus two hydrogen) on Pt(111), are illustrated in Figure 4.3(a).

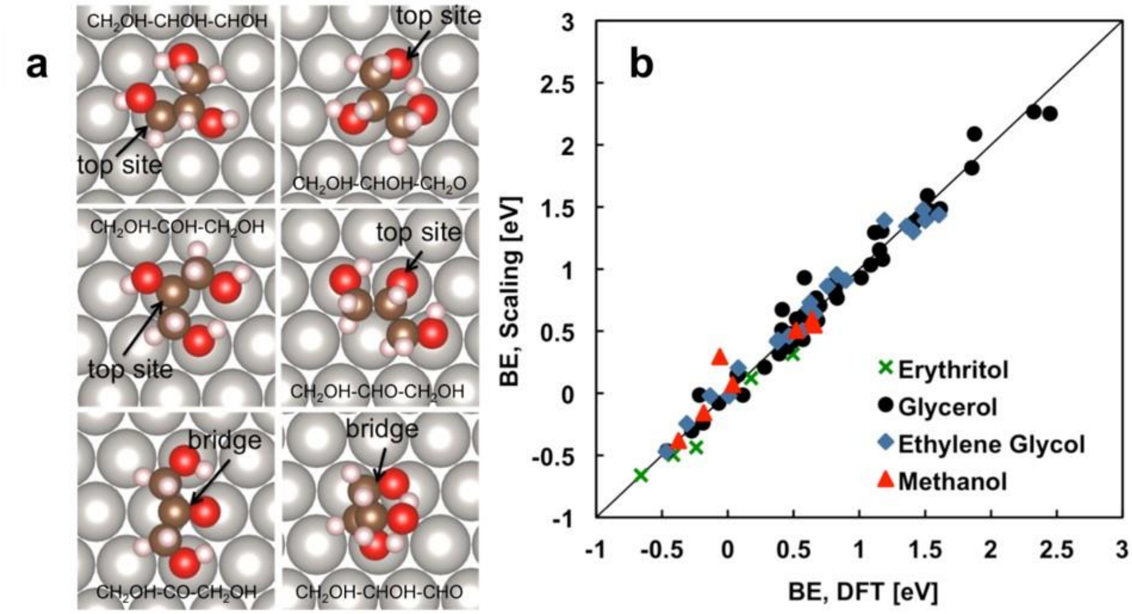

Figure 4.3 (a) Adsorption configurations of selected glycerol dehydrogenation intermediates on Pt(111) from periodic DFT calculations. C, O, H, and Pt are depicted in brown, red, pink, and grey, respectively. The preferred binding site in each case is indicated by the arrow. (b) Comparison of the predicted binding energies from an empirical scaling scheme and DFT calculations for methanol (red triangles), ethylene glycol (blue diamonds), glycerol (black circles), and erythritol (green crosses) dehydrogenation intermediates on Pt(111). Adapted with permission from Ref [19]. Copyright 2018, American Chemical Society.

A general rule has been established to predict the preferred binding sites (i.e., top, bridge, 3-fold as indicated in Figure 4.3(a)) and molecular configuration without the consideration of solvent effect. Over Pt(111), each species is found to favor the configuration that satisfies the gas-phase valencies of the respective binding C and O atoms. For C and O, the respective valencies are 4 and 2, as in methane and water molecules. As illustrated in Figure 4.3(a), all $C_3H_7O_3$ species prefer the Pt top site, while glyceraldehyde and dihydroxyacetone bind at the bridge site to satisfy both C and O in the ketone or the aldehyde functional group. In addition, the orientation and arrangement of the hydroxyl groups should also be considered because: (1) intramolecular hydrogen bonding among these hydroxyl groups stabilizes the overall structure; (2) additional stabilization can be gained from the molecular orientation that maximizes the interactions between hydroxyl groups and the metal substrate. When glycerol becomes significantly dehydrogenated, these rules can be broken occasionally due to molecular strain or highly delocalized bonding. Besides Pt, such rules are generally applicable to other transition metals such as Pd, Rh, Ni. However, over Au, Ag, and Cu, noticeable deviations have been observed in part due to very weak binding of C=C, or C=O bonds on these metal surfaces.

The valency rule for adsorbed molecular species is not a new concept. Classical bond-order conservation formulations can be found in works by Shustorovich [69, 70], Kua and Goddard [71], and Abild-Pedersen et al. [72] A common consensus is that the predictable behavior of these adsorbates can be exploited to accelerate the search for stable adsorption configurations, which otherwise would be an extremely tedious and time-consuming task for DFT calculations. For metals (e.g., Pt, Pd) that exhibit high level of agreement with the rule, actual calculations can even be omitted.

The so-called scaling relationship for glycerol and its intermediates developed previously on Pt(111) in a solvent free condition is expressed by Equations (36) and (37) [15, 16].

$$BE_{C_3H_xO_3^*} = \sum_i p_{Ci}v_{Ci} + \sum_i p_{Oi}v_{Oi} + \sum_{i,j} p_{CiOj}v_{Ci}v_{Oj} + \sum_{i,j} p_{CiCj}v_{Ci}v_{Cj} + BE_{C_3H_8O_3} \tag{36}$$

$$v_i = \frac{n_{max} - n_{bond}}{n_{max}}, \tag{37}$$

where v_{Ci} and v_{Oi} describe the degree of undersaturation of central C and O atoms in $C_3H_xO_3$, as represented by Equation (37), where n_{max} is 4 for C and 2 for O based on the gas-phase valence rule, and n_{bond} represents the total neighbors to which the central C/O atom is bonded (counting H, C, and O only). The last term, $BE_{C_3H_8O_3}$, in Equation (36) is the binding energy of gas phase glycerol on Pt(111). In Equation (1), p_{Ci}, p_{Oi}, p_{CiOj}, and p_{CiCj} are fitting parameters obtained from DFT calculations [15]. As illustrated by Figure 4.3(b), the scheme has been proven to predict binding energies of polyols (ethylene glycol, erythritol, and methanol all with C:O = 1:1 in these molecules) quite well, with an averaged error of 0.11 eV, using the same set of parameters derived only from glycerol intermediates on Pt(111). Whether such a scaling relationship can be adopted to predict energetic trends in adsorbed oxygenated hydrocarbon immersed in liquid water in a similar manner is an appealing topic to explore.

Recent efforts to understand interactions between liquid water and sugar alcohol adsorbates have been reported by Getman and co-workers in a series of combined periodic DFT and molecular dynamics simulations [73, 74]. It has been shown that water molecules near adsorbates re-orient to form hydrogen bonds. It is also pointed out that the significant hydrogen bonding phenomena will pose challenges to surface-bound polyol species.

Set on the explicit solvation approach, two measures have been taken in order to simplify the model structures to the extent that hydrogen bonding configurations can be systematically investigated. (1) The solvation contribution to adsorption energies can be broken down as water-metal, water-adsorbate, and water-water interactions. (2) Only the first water overlayer is included in the model.

The binding energy, generally represented as $C_3H_xO_3^*(aq)$, x = 0–8 in the presence of n explicit H_2O molecules, is denoted as $BE_{C_3H_xO_3^*(aq),DFT}$ and calculated as in Equation (38).

$$BE_{C_3H_xO_3^*(aq),DFT} = E_{C_3H_xO_3^*(aq)} - E_* + \frac{8-x}{2}E_{H_2(g)} - E_{glycerol(g)} - nE_{H_2O(g)}, \tag{38}$$

In Equation (38), the total energy of adsorbate on Pt(111) is $E_{C_3H_xO_3^*(aq)}$. Clean Pt(111) surface, gas phase H_2, glycerol, and H_2O are used as the zero potential energy reference, represented by E_* , $E_{H_2(g)}$, $E_{glycerol(g)}$, and $E_{H_2O(g)}$, respectively. This definition can be interpreted as the energetic tendency for $C_3H_xO_3$ to form covalent bond(s) upon adsorption, and by removal of $(8-x)$ hydrogen atoms as a stoichiometric number of gas phase hydrogen molecules. In addition, energy changes associated with the formation of water-water, water-adsorbate, and water-Pt(111) pair interactions are also included.

The first four terms on the right-hand side of Equation (36) remain the same as that in the solvent-free system. Except for glycerol, these valency-dependent (non-zero v_{Ci} and v_{Oi}) adsorptions are likely covalent in nature. The solvation effect can be collectively expressed by ξ, as shown in Equation (39).

$$\xi = \varepsilon_{ads-H_2O} + \varepsilon_{M-H_2O} + \varepsilon_{H_2O-H_2O}, \tag{39}$$

where contributions from water-adsorbate, water-metal, and water-water interactions are represented by ε_{ads-H_2O}, ε_{M-H_2O}, and $\varepsilon_{H_2O-H_2O}$, respectively. Computational details and quantification of each item are discussed in the following sections.

The binding energy of glycerol in aqueous phase, $BE_{C_3H_8O_3(aq)}$, can be written as Equation (40). By using the scaling scheme, the binding energy becomes Equation (41).

$$BE_{C_3H_8O_3(aq)} = \varepsilon_{gly-M} + \xi \tag{40}$$

$$BE_{C_3H_xO^*_{3(aq)}} = \sum_i p_{Ci}v_{Ci} + \sum_i p_{Oi}v_{Oi} + \sum_{i,j} p_{CiOj}v_{Ci}v_{Oj} + \sum_{i,j} p_{CiCj}v_{Ci}v_{Cj} + BE_{C_3H_8O_3(aq)} \tag{41}$$

where ε_{gly-M} is the binding energy of glycerol on metal (M). On Pt(111) in vacuum, this value is -0.46 eV, which is reported in Ref [15].

According to Equation (40), it can also be deduced that, if the variations of the solvation effect were small for different adsorbates, ξ should remain approximately constant. The net effect on solvated binding energy ($BE_{C_3H_xO_3(aq)}$) shall in principle follow the original scaling trend dictated by Equation (36), but with a constant shift.

4.2 Computational Details

Periodic DFT calculations have been employed to obtain optimized structures. The results reported here were obtained using the Vienna *Ab initio* Simulation Package (VASP) [75, 76]. The computational parameters remain the same as in Ref [15]. in order to maintain consistency with scaling relationship development. The electronic one-particle wave function was expanded up to an energy cutoff of 380 eV. Convergence tests on the energy cutoff (up to 450 eV) using co-adsorbed glycerol and water molecules show that the binding energy change is within 10 meV. A Monkhorst-pack k-point mesh of 4 × 4 × 1 was used to sample the reciprocal first Brillouin zone [77]. The convergence criteria for self-consistent iteration and the ionic relaxation are 1×10^{-6} eV and 0.02 eV/Å, respectively. The Methfessel-Paxton smearing at k_BT = 0.2 eV was used, and the total energies were then extrapolated to 0 K. Dipole correction were included in all calculations.

The close-packed planar platinum surface is modeled with the Pt(111) facet using a 3-layer $p(4 \times 4)$ supercell. The bottom two layers were fixed to the optimized platinum bulk lattice value at 3.98 Å. The top layer of Pt(111), adsorbate, and water molecules were allowed to relax. The binding energies reported here are not corrected to account for van der Waals interactions. In polar solvents (e.g., water), electrostatic interactions dominate (over van der Waals interactions) in systems consisting of polar or ionic solutes [78]. Nevertheless, van der Waals interactions described at the DFT-D3 level have been shown to alter the adsorption structures of adsorbed alcohols such as ethanol even without the presence of solvent [79-84]. In order to fully integrate this non-covalent effect, it is possible that the scaling relationship needs to be further verified.

4.3 Interactions Between Water and Pt(111)

Compared to the covalent interactions between surface and adsorbate, water-metal interactions are relatively weak. Periodic DFT calculations reported in the literature show that the adsorption energies of a single water molecule on the (111) facet of transition metals vary between -0.1 to -0.4 eV in the order of Au < Ag < Cu < Ni < Pd < Pt < Ru < Rh [85-88]. The absolute value and exact order are sensitive to bulk lattice constant, size of unit cell and computational method. An isolated water molecule binds parallel to metal tops site via the lone pair electrons located on oxygen.

Our calculation showed the binding energy of an isolated H_2O molecule on Pt(111) is -0.31 eV, with the distance between O and Pt being 2.30 Å, as indicated in Figure 4.4(a), and is in good agreement with prior report in the literature [28]. This value is also equivalent to the Pt-H_2O interaction energy. Hence, the value is assigned to ε_{Pt-H_2O}, as in Equation (42).

$$\varepsilon_{Pt-H_2O} = -0.31\ eV \tag{42}$$

To mimic the water-water interaction, a second water molecule is added to the first H_2O adsorbate, creating a water dimer. The optimized structure of the second water is positioned in a tilted H-down position as illustrated in Figure 4.4(b), resembling a sub-unit of the H-down water bilayer in Figure 4.4(c). A hydrogen bond, with a bond length of 1.61 Å highlighted in a violet bar in Figure 4.4(b), is formed between the two waters.

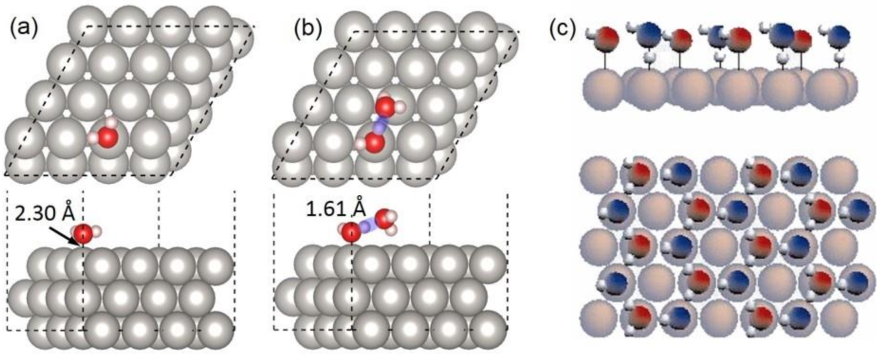

Figure 4.4 Adsorptions of (a) single H_2O, and (b) two adjacent H_2O molecules on Pt(111). The O–Pt bond distance (2.30 Å) in (a), and H–O bond distance (1.61 Å) in (b) are listed. The hydrogen bond between two H_2O molecules is indicated by the violet bar. Supercell boundaries are shown in black dashed lines. O, H, and Pt atoms are shown in red, pink and grey, respectively. (c) Illustration of the 'H-down' water bilayer configuration on Pt(111). Adapted with permission from Ref [19]. Copyright 2018, American Chemical Society.

The overall binding energy of these co-adsorbed H_2O molecules is -0.91 eV, relative to water molecules in the gas phase. By excluding the contribution from the first H_2O molecule, i.e., ε_{Pt-H_2O} (-0.31 eV), and the interaction between Pt(111) and the second water and Pt(111) (i.e., -

0.07 eV, obtained from a static calculation after the removal of the first H_2O), the net water-water interaction is -0.53 eV. The negative sign indicates that the interaction between this water dimer stabilizes the water dimer structure. This value is actually higher than the interaction between two water molecules (-0.24 eV) in the gas phase, suggesting that the substrate further enhances the clustering of co-adsorbed water molecules. Here, $\varepsilon_{H_2O-H_2O}$ assumes the value of -0.53 eV, as in Equation (43).

$$\varepsilon_{H_2O-H_2O} = -0.53\ eV \tag{43}$$

4.4 Interactions Between Water and Adsorbed Glycerol on Pt(111)

In the absence of water, we have shown that glycerol binds at the top site via the oxygen atom in one of the terminal hydroxyl groups on Pt(111) [15]. It has been confirmed that the nature of such interaction originates from oxygen's lone pair electrons. For glycerol, an intramolecular hydrogen bond exists between the two terminal hydroxyl groups, as indicated by the green bars in Figure 4.5(a-f), while the middle hydroxyl group tilts away from the surface in the opposite direction.

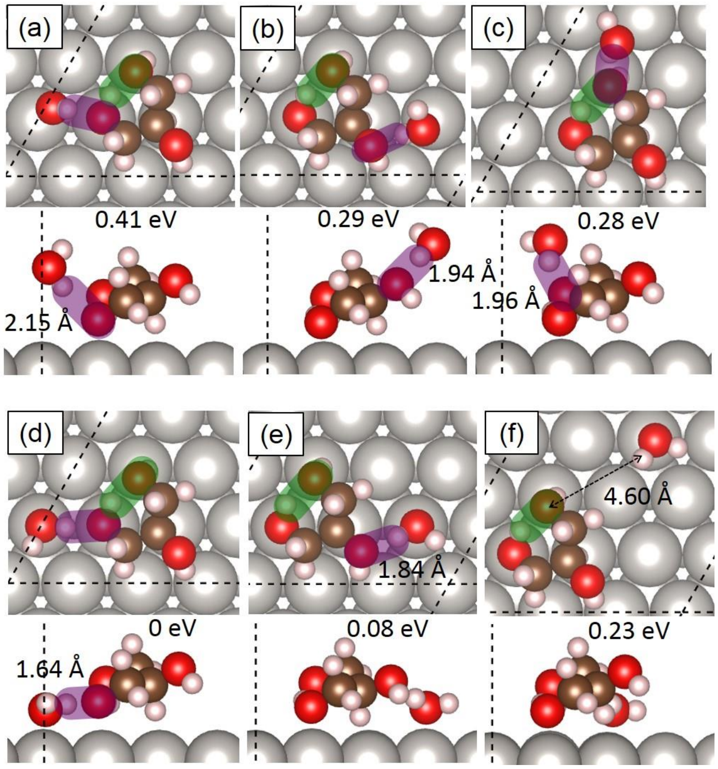

Figure 4.5 Top and side views of glycerol and water co-adsorbed on Pt(111) in various scenarios (a-f). C, O, H, and Pt atoms are shown in brown, red, pink and grey, respectively. The intramolecular hydrogen bond is highlighted with green bars; intermolecular hydrogen bonds between water and glycerol are highlighted in purple, with bond lengths labeled. Supercell boundaries are shown in black dashed lines. The relative energies were listed in eV in each image. Adapted with permission from Ref [19]. Copyright 2018, American Chemical Society.

The structure of adsorbed glycerol on Pt(111) without solvent is used as the starting point. Water (i.e., the first H_2O added) is used to probe the potential energy surrounding the adsorbed glycerol. In configurations Figure 4.5(a-c), water is deliberately separated from Pt(111) to minimize its interactions with the substrate. A close distance is maintained so that water is still capable of interacting with one of the hydroxyl groups (highlighted by purple bars). The intermolecular hydrogen bond lengths in configurations (a-c) are 2.15, 1.94, and 1.96 Å, respectively. In configurations (d) and (e), water molecules are placed directly above Pt(111) so that water-metal interactions can be enabled. In both cases, water still prefers to bind on the Pt top site while maintaining the intermolecular hydrogen bonding with glycerol, at a distance of 1.64 Å and 1.84 Å, respectively. The intramolecular hydrogen bonding shown in green bars, in both cases, is preserved. In Figure 4.5(f), the water molecule co-adsorbed with glycerol is deliberately separated at a distance of 4.60 Å (as indicated by the double-headed arrow), to minimize a direct adsorbate-water interaction.

Table 4.1 Binding energies of co-adsorbed of glycerol and single H_2O molecule ($\boldsymbol{BE_{C_3H_8O_3^*(aq),DFT}}$ in eV) on Pt(111). Adapted with permission from Ref [19]. Copyright 2018, American Chemical Society.

Configuration	(a)	(b)	(c)	(d)	(e)	(f)
$BE_{C_3H_8O_3^*(aq),DFT}$	-0.66	-0.78	-0.79	-1.07	-0.99	-0.84

Binding energies ($BE_{C_3H_8O_3^*(aq),DFT}$) of obtained from configurations (a-f) are summarized in Table 4.1, determined from Equation (38) at *n* = 1 and x = 8. The most energetically favorable configuration is (d), in which the overall binding energy is -1.07 eV. Configuration (a), on the other hand, is the least energetically favored. This result signifies the importance of water-metal interactions at the interface, and showed that the adsorbate does not exclude co-adsorbed water in its proximity. The binding energy of configuration (f) is 0.23 eV higher than configuration (d). This difference can be considered as the interaction energy between glycerol and water, assuming that the values ε_{Pt-H_2O}, are similar. Hence, ε_{gly-H_2O} for glycerol-water interaction, as in Equation

(44), can be approximate as -0.23 eV. Again, the minus sign indicates that this interaction stabilizes the co-adsorbed structure.

$$\varepsilon_{gly-H_2O} = -0.23\ eV \tag{44}$$

To include water-water interactions, the number of water molecules (n) is increased incrementally (up to 12). The most stable structure for each n value is illustrated in Figure 4.6(a-g). At $n = 2$ in Figure 4.6(b), the second water molecule (highlighted in a yellow circle) prefers the location that enables the formation of an intermolecular hydrogen bond (highlighted in blue) with the first water molecule. In addition, the second water molecule is in the H-down position, resembling the structure identified in Figure 4.4(b). This way, all co-adsorbed species are in their preferred configuration. Thus, the system consists of two intermolecular hydrogen bonds (i.e., water-water and water-glycerol), and one intramolecular hydrogen bond from the structure of adsorbed glycerol.

At $n = 3$ in Figure 4.6(c), the third water (highlighted in a yellow circle) is added to extend the water chain, resulting one additional intermolecular hydrogen bond (blue bar). Moreover, it can be seen that the extended structure enables this water to interact with the glycerol's own periodic image (through the middle hydroxyl group) in the neighboring supercell. Hence, a continuous (1-D) network centered on the adsorbate that is inter-connected its periodic images via water molecules, is established.

At $n = 4$ in Figure 4.6(d), the fourth water molecule (highlighted in the dashed yellow circle) continues to contribute to the growth of the established water network by interacting with the other terminal hydroxyl group facilitated by the periodicity of the supercell. At this stage, a close-loop structure, in an approximate hexagonal shape (highlighted in purple to guide visualization), is formed. All the hydroxyl groups available in glycerol are now able to coordinate with one water molecule.

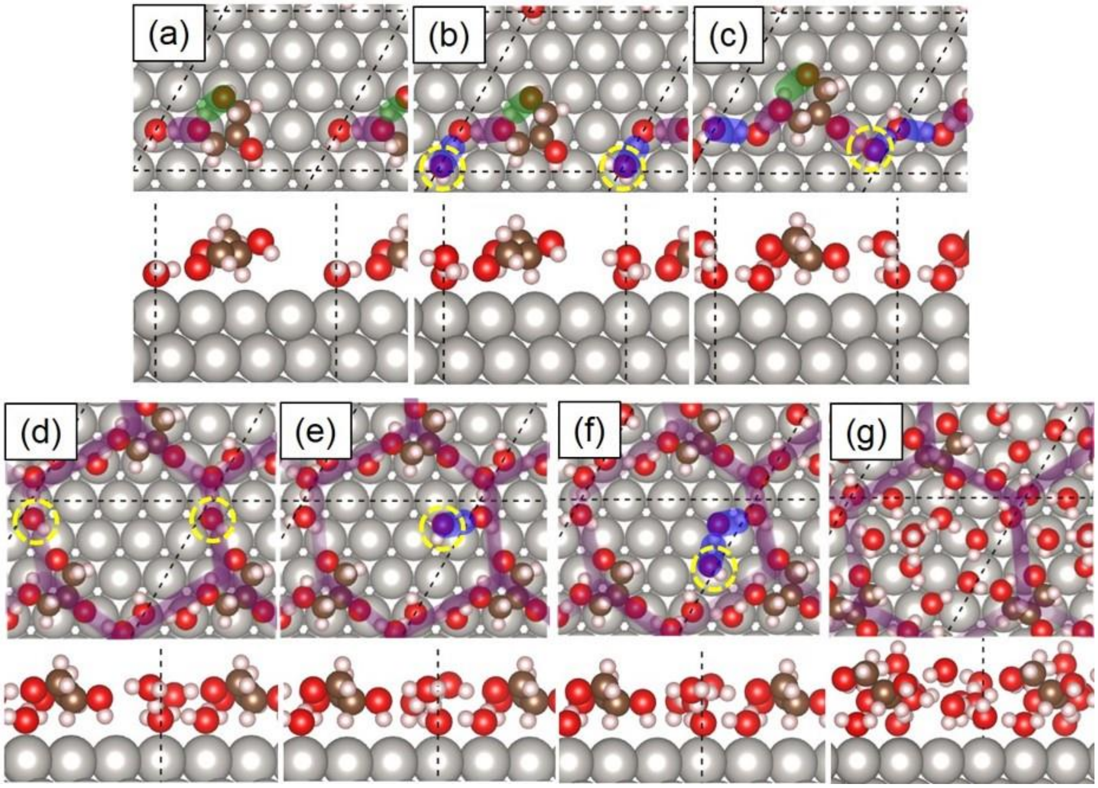

Figure 4.6 Co-adsorption of glycerol on Pt(111)with (a) 1 H_2O, (b) 2 H_2O, (c) 3 H_2O, (d) 4 H_2O, (e) 5 H_2O, (f) 6 H_2O, and (g) 12 H_2O molecules. C, O, H, and Pt atoms are in brown, red, pink and grey, respectively. Green, purple, and blue bars in (a-c) indicate the intramolecuar hydrogen bond, glycerol-water, and water-water hydrogen bonding, respectively. Supercell boundaries are shown in black dashed lines. Adapted with permission from Ref [19]. Copyright 2018, American Chemical Society.

The additions of the fifth and sixth water molecules are depicted in Figure 4.6(e-f), respectively. Since there is no free hydroxyl group in glycerol to accept additional water molecules, the fifth and sixth water can only be added to the existing water network. All intermolecular hydrogen bonds are indicated with blue bars. In Figure 4.6(f), with six water molecules, a secondary five-member-ring is formed.

When twelve water molecules are added, the remaining open space of Pt(111) is being occupied, resulting a surface now fully covered with glycerol and a water overlayer, as illustrated in Figure 4.6(g), consisting of five- or six-membered water rings. Such water formation has been reported by Nie and coworkers [51], who confirmed the existence of a mixture of five-, six-, and seven-membered rings with the $\sqrt{37}$ and $\sqrt{39}$ periodic wetting arrangement on Pt(111) from scanning tunneling topography measurements and DFT calculations.

It can be seen that the growth initiates from the adsorbed glycerol, and then expands from its anchoring hydroxyl groups. As the number of water molecules increases, the water structure evolves from a linear structure to a hexagonal network through water-water interactions. The first-layer water molecules still maintain a close contact with Pt(111). Intermolecular hydrogen bonding between hydroxyl groups and water molecules is satisfied.

Table 4.2 Calculated $\boldsymbol{BE_{C_3H_8O_3^*(aq),DFT}}$ (in eV) on Pt(111) at different *n* values. Adapted with permission from Ref [19]. Copyright 2018, American Chemical Society.

n	1	2	3	4	5	6	12
$BE_{C_3H_8O_3^*(aq),DFT}$	-1.07	-1.65	-2.23	-2.90	-3.32	-3.82	-7.62

The binding energies of adsorbed glycerol ($BE_{C_3H_8O_3^*(aq),DFT}$) calculated from Equation (38) with n H_2O molecules, as illustrated in Figure 4.6(a-g), are tabulated in Table 4.2. The values of $BE_{C_3H_8O_3^*(aq),DFT}$ incrementally decrease by approximately 0.5—0.6 eV with each additional

H_2O added, coinciding with the value of $\varepsilon_{H_2O-H_2O}$. The differential binding energies per H_2O are also plotted in Figure 4.7 (black stars). The upward trend indicates that the energetic gain diminishes with each additional water as fewer favorable locations are available to form hydrogen bonding. Additional water molecules is expected to form the second water overlayer.

4.5 Intermediates on Pt(111) and Scaling Relationship

4.5.1 Adsorptions of Glycerol Dehydrogenation Intermediates on Pt(111)

Glycerol dehydrogenation via C-H or O-H bond scission is a main route for the production of hydrogen, as well as numerous value-added chemicals such as dihydroxyacetone, lactic acid, 1,2-propanediol, alcohols and alkanes [89, 90]. In this work, four mono-dehydrogenated ($C_3H_7O_3$) and up to ten di-dehydrogenated intermediates ($C_3H_6O_3$) were chosen. Among the $C_3H_6O_3$ species, dihydroxyacetone (CH_2OH-CO-CH_2OH) and glyceraldehyde (CH_2OH-CHOH-CHO) are two stable and also marketable dehydrogenation products, which can be produced selectively from electrooxidation [4].

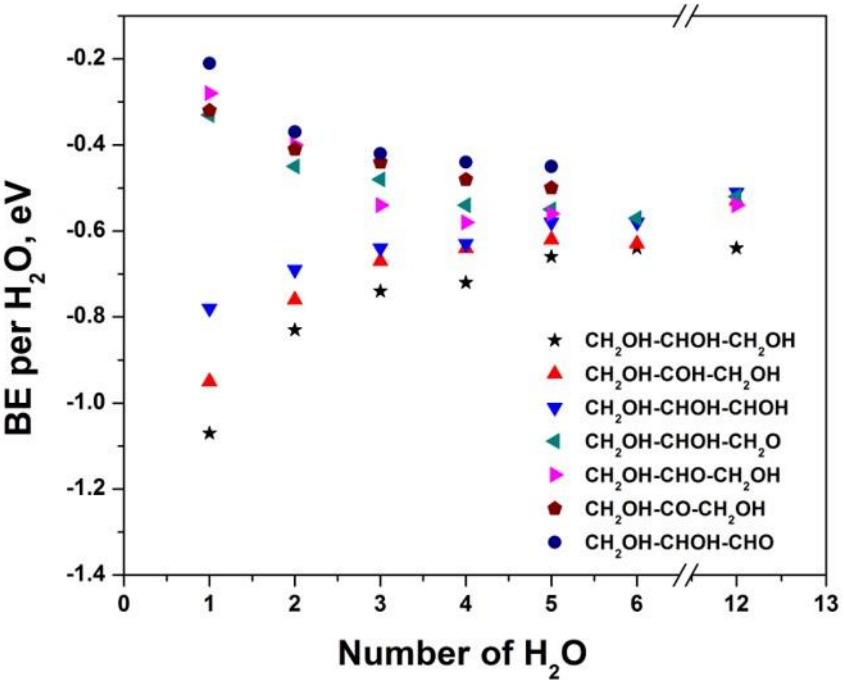

Figure 4.7 DFT-calculated $BE_{C_3H_xO_3^*(aq),DFT}$ (x = 0-8) per H_2O at different numbers of H_2O on Pt(111). Adapted with permission from Ref [19]. Copyright 2018, American Chemical Society.

Optimized configurations for each selected $C_3H_xO_3$ intermediate (x = 6, 7) were obtained on Pt(111), using structures from vapor phase calculations for relaxation. Water molecules were introduced in a similar manner, largely informed by the patterns observed in Figure 4.6. For the majority of intermediates, we found that five water molecules are needed to form closed network structures on the surface. The most stable configurations for $C_3H_7O_3$ and $C_3H_6O_3$ co-adsorbed with five water molecules are illustrated in Figures 4.8-4.9, respectively.

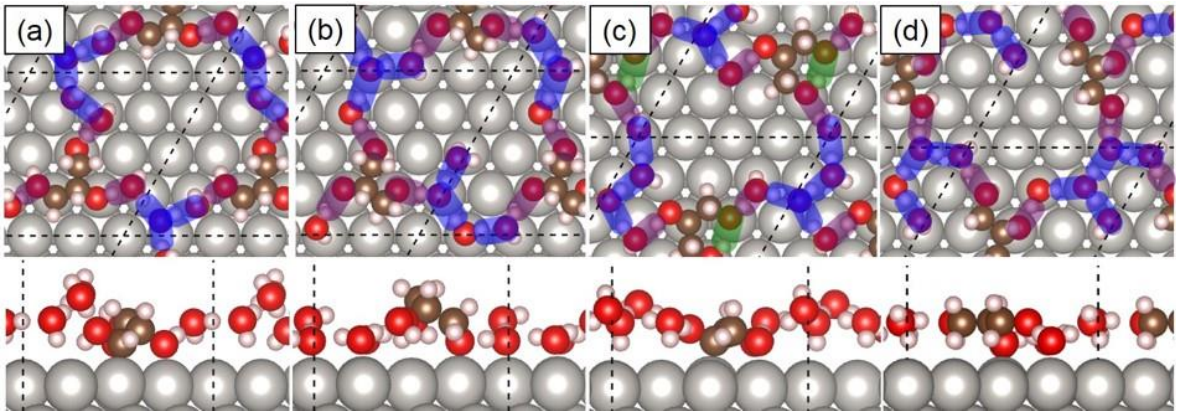

Figure 4.8 Top and side views of the four $\boldsymbol{C_3H_7O_3}$ intermediates, (a) CH_2OH-CHOH-CHOH, (b) CH_2OH-CHOH-CH_2O, (c) CH_2OH-COH-CH_2OH, and (d) CH_2OH-CHO-CH_2OH, with five water molecules on Pt(111) in their most stable configurations. C, O, H, and Pt atoms are shown in brown, red, pink and grey, respectively. Green, purple, and blue bars highlight intramolecuar hydrogen bond, adsorbate-water, and water-water interaction, respectively. Supercell boundaries are shown in black dashed lines. Adapted with permission from Ref [19]. Copyright 2018, American Chemical Society.

The binding sites for all four $C_3H_7O_3$ intermediates remain unchanged at the top site of Pt(111), as illustrated in Figure 4.8(a-d). Again, the intramolecuar hydrogen bond, adsorbate-water, and water-water interactions are distinguished by the green, purple, and blue bars. Through co-adsorbed water molecules, adsorbates forms familiar continuous networks with their periodic images across the unit cell boundaries. Despite the ideal situation facilitated by such a specific periodic boundary condition, we believe the predicted molecular structures presented in Figures 4.8 and 4.9 still provide the insights into the direct interactions among adsorbate, solvent, and substrate at the interface that cannot be probed straightforwardly otherwise. As highlighted in purple in Figure 4.8, all three hydroxyl groups have to be involved in establishing connections linked by water molecules through hydrogen bonding. Similar observations were made for many of the $C_3H_6O_3$ intermediates illustrated in Figure 4.9 as well.

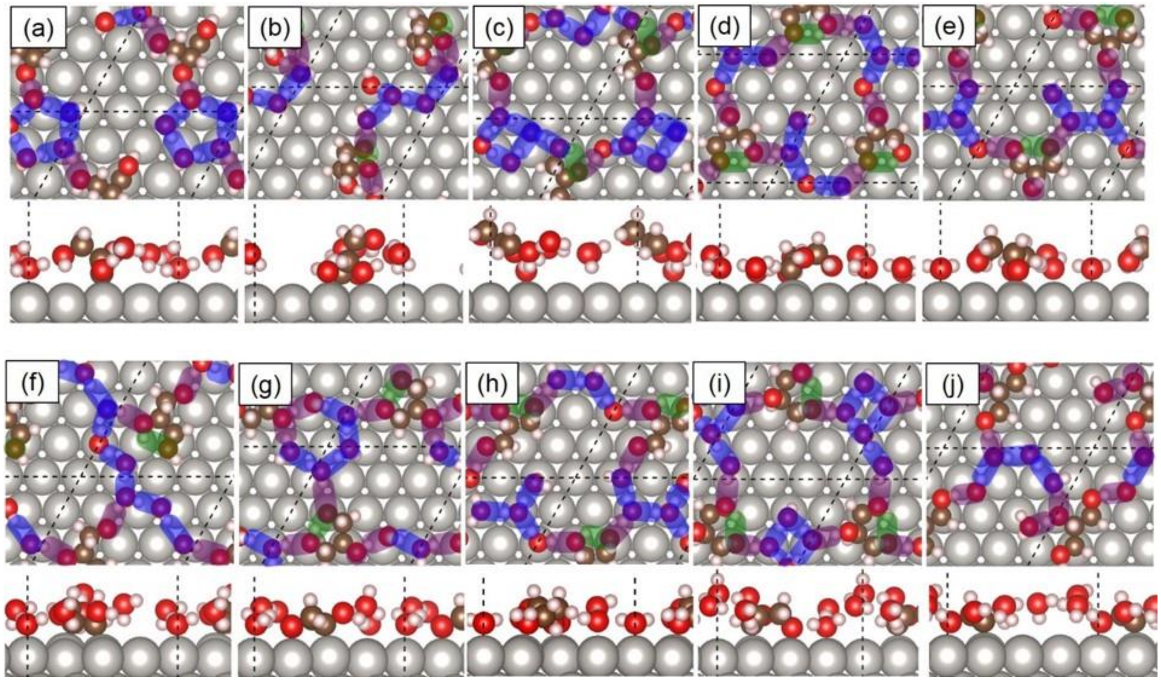

Figure 4.9 Top and side views of ten selected $\boldsymbol{C_3H_6O_3}$, co-adsorbed with five water molecules on Pt(111) in their most stable configurations. (a) CH_2OH-CHOH-COH, (b) CH_2OH-CHOH-CHO, (c) CH_2OH-CO-CH_2OH, (d) CH_2OH-CHO-CHOH, (e) CH_2OH-CHO-CH_2O, (f) CH_2OH-COH-CHOH, (g) CH_2OH-COH-CH_2O, (h) CH_2O-CHOH-CH_2O, (i) CHOH-CHOH-CH_2O, and (j) CHOH-CHOH-CHOH. C, O, H, and Pt are in brown, red, pink and grey, respectively. Green, purple, and blue bars highlight intramolecuar hydrogen bond, adsorbate-water, and water-water interaction, respectively. Supercell boundaries are shown in black dashed lines. Adapted with permission from Ref [19]. Copyright 2018, American Chemical Society.

The binding energies, calculated from Equation (38), for the four $C_3H_7O_3$, dihydroxyacetone, and glyceraldehyde with $n = 0, 1, 5$ co-adsorbed water molecules, are tabulated in Table 4.3. At $n = 0$ (solvent free), it is known that the intermediates from C-H bond scission are more stable than those from O-H bond scission (with the same stoichiometry) on Pt(111) [15]. At $n = 1$, binding for all intermediates becomes stronger (i.e., more negative) due to the attractive interactions (ε_{gly-H_2O} and ε_{Pt-H_2O}) provided by the water on a rather open surface. At $n = 5$, $BE_{C_3H_xO_3^*(aq),DFT}$ become less negative for the two intermediates that bind with C, but are still lower (more negative) than those when no water was added. The molecular perspective obtained indicates that the energetic difference during glycerol dehydrogenation could be diminished due to the solvation effect.

The calculated $BE_{C_3H_xO_3^*(aq),DFT}$ per H_2O for these dehydrogenation intermediates are also shown in Figure 4.7. It becomes clear that, with the increase of water molecules, binding energies of glycerol and intermediates that bind with C become less negative; but an opposite trend is observed for intermediates that bind with unsaturated O. In the high water coverage limit considered, binding energies for selected intermediates converge to within 0.2 eV.

Table 4.3 Comparisons for $\boldsymbol{BE_{C_3H_xO_3^*(aq),DFT}}$ (x = 6, 7, in eV) at n = 0, 1, 5 using Equation (38). Adapted with permission from Ref [19]. Copyright 2018, American Chemical Society.

Species	$BE_{C_3H_xO_3^*(aq),DFT}$, $n = 0$	$BE_{C_3H_xO_3^*(aq),DFT}$, $n = 1$	$BE_{C_3H_xO_3^*(aq),DFT}$, $n = 5$
CH_2OH-COH-CH_2OH	-0.27	-0.95	-0.62
CH_2OH-CHOH-CHOH	-0.19	-0.78	-0.58
CH_2OH-CHOH-CH_2O	0.41	-0.33	-0.55
CH_2OH-CHO-CH_2OH	0.45	-0.28	-0.57
CH_2OH-CO-CH_2OH	0.48	-0.32	-0.50
CH_2OH-CHOH-CHO	0.53	-0.21	-0.45

4.5.2 Scaling Relationship for Solvated Systems

It is mentioned that a scaling relationship based on valences of unsaturated C and/or O exists in a solvent-free environment [15]. Here, we set out to re-examine this formulation, i.e., Equations (37) and (41), by incorporating water-adsorbate, water-metal, and water-water interactions. $BE_{C_3H_xO_3^*(aq),DFT}$, denoted as BE (DFT) in Figure 4.10, are evaluated based on Equation (38), at $n = 5$.

Because configuration of each adsorbate does not vary significantly, the covalent interaction in $BE_{C_3H_xO_3^*(aq)}$ between adsorbate and metal can be assumed intact. The ξ term in Equation (39) is composed of contributions from four hydrogen bonding between water molecules ($4\varepsilon_{H_2O-H_2O}$), two hydrogen bonding between glycerol and water ($2\varepsilon_{gly-H_2O}$,), and water-Pt(111) interactions from two water molecules ($2\varepsilon_{Pt-H_2O}$). By simple summation, ξ is calculated as -3.20 eV. Combined with ε_{gly-M}, $BE_{C_3H_8O_3^*(aq)}$ is -3.66 eV from Equation (40).

The comparison between BE (DFT) and $BE_{C_3H_xO^*_{3(aq)}}$ from Equation (41), donated as BE(scaling), are shown in Figure 4.10(a). The standard errors associated with the scaling for $C_3H_7O_3$ and $C_3H_6O_3$ are 0.20 eV and 0.17 eV, respectively. It can be seen that all BE (DFT) have shifted downward by 0.34 eV from the parity line ($y = x$), which originates from the difference between $BE_{C_3H_8O_3^*(aq),DFT}$ (-3.32 eV, $n = 5$) and the glycerol binding energy obtained from Equation (40) (-3.66 eV). In fact, the shift can be eliminated when $BE_{C_3H_8O_3^*(aq),DFT}$, is used in Equation (41) to generate the scaling relationship, as shown in Figure 4.10(b).

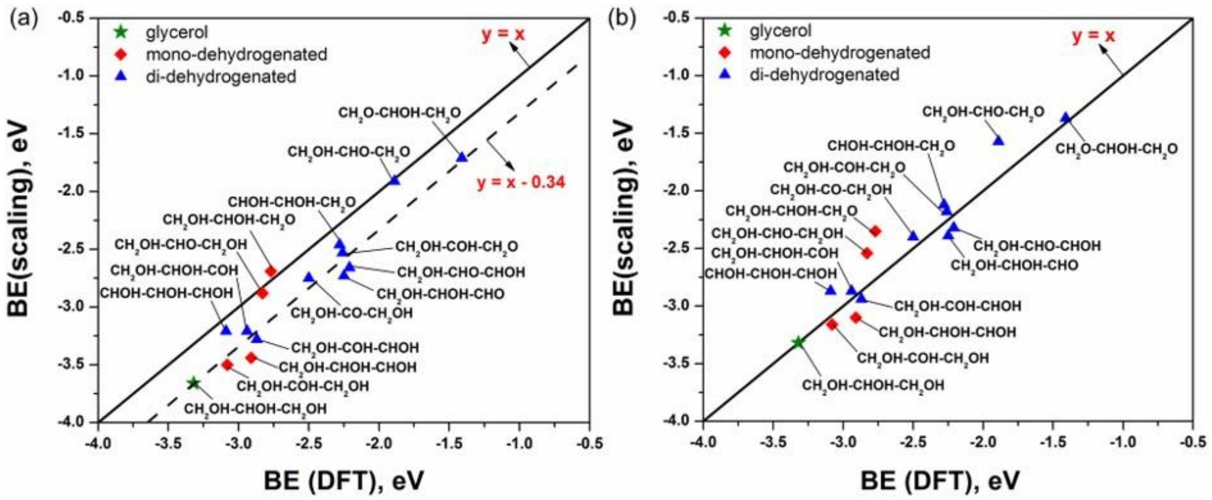

Figure 4.10 Relationship between DFT calculations from Equation (3) and scaling based on Equations (37, 39-41), for glycerol (green star), $\boldsymbol{C_3H_7O_3}$ (red diamonds) and $\boldsymbol{C_3H_6O_3}$ (blue triangles) with five H_2O molecules on Pt(111). Adapted with permission from Ref [19]. Copyright 2018, American Chemical Society.

The observed constant energy shift has provoked a widely adapted notion in the computational community that solvent often indiscriminately affects the binding energies of structurally similar adsorbates. The accompanying energetic analysis confirms this long-standing belief for adsorbed glycerol and its intermediates. It should also be pointed out that, despite the fact of a general agreement, the binding of CH$_2$OH-CHOH-CH$_2$O, CH$_2$OH-CHO-CH$_2$OH, and CH$_2$OH-CHO-CH$_2$O, as in Figure 4.8(b), 4.8(d), and 4.9(e) show noticeable deviation from the scaling relationship and their values are underestimated. The underlying cause of such deviation can be attributed to significant variation in the adsorption configurations of these adsorbates from glycerol. This can be interpreted that certain adsorbates on solid surface are likely undergo structure transformation upon solvation. In order to reconcile with the predictions of the scaling relationship, new configurations for these intermediates must be tested.

4.6 Conclusions

In this work, we tackled an important aspect of catalytic glycerol processing in the aqueous phase environment by investigating the adsorption patterns of glycerol and its dehydrogenation intermediates at the metal-liquid interface. By using the explicit solvation approach, extensive network structures established by adsorbates and co-adsorbed water molecules were elucidated through periodic DFT calculations. As a result, specific metal-water, water-water and adsorbate-water interactions on Pt(111) are described using simple pairwise interaction energy concepts. We found that although interaction of water with polar adsorbates, metal, and other water molecules are always attractive in nature, the net impact on adsorption energies vary. Compared to the solvent free systems, stronger binding intermediates generally experience a 'weakening' effect, while, on the other hand, weaker binding intermediates benefits from the existence of water to bind on Pt(111). Here, the scaling relationship has been re-evaluated by including various solvent-related molecular interactions. It is believed that this strategy shall continue to play an important role in minimizing unnecessary computational costs while detailed molecular information is still required for structural and mechanistic analyses.

4.7 Acknowledgements

This work is financially supported by Start-up funding provided by Kansas State University. N.S. would also like to thank the summer support from the Erickson Fellowship. We are grateful for the supercomputing service provided by K-State Beocat Research Cluster funded in part by NSF grants CHE-1726332, CNS-1006860, EPS-1006860, and EPS-0919443; Center for Nanoscale Materials (CNM) at Argonne National Laboratory supported by the Office of Science of the US Department of Energy under the contract No. DE-AC02-06CH11357; and the National

Energy Research Scientific Computing Center (NERSC) under the contract No. DE-AC02-05CH11231.

Bibliography

[1]. Garcia, R.; Besson, M.; Gallezot, P., Chemoselective catalytic-oxidation of glycerol with air on platinum metals. *Applied Catalysis a-General* **1995,** 127, (1-2), 165-176.
[2]. Chheda, J. N.; Huber, G. W.; Dumesic, J. A., Liquid-phase catalytic processing of biomass-derived oxygenated hydrocarbons to fuels and chemicals. *Angewandte Chemie-International Edition* **2007,** 46, 7164-7183.
[3]. Zhou, C.-H.; Beltramini, J. N.; Fan, Y.-X.; Lu, G. Q., Chemoselective catalytic conversion of glycerol as a biorenewable source to valuable commodity chemicals. *Chemical Society Reviews* **2008,** 37, (3), 527-549.
[4]. Kwon, Y.; Schouten, K. J. P.; Koper, M. T. M., Mechanism of the catalytic oxidation of glycerol on polycrystalline gold and platinum electrodes. *ChemCatChem* **2011,** 3, (7), 1176-1185.
[5]. Simoes, M.; Baranton, S.; Coutanceau, C., Electrochemical valorisation of glycerol. *Chemsuschem* **2012,** 5, (11), 2106-2124.
[6]. Nilges, P.; Schröder, U., Electrochemistry for Biofuel Generation: Production of Furans by Electrocatalytic Hydrogenation of Furfurals. *Energy & Environmental Science* **2013,** 6, (10), 2925-2931.
[7]. Parpot, P.; Bettencourt, A. P.; Chamoulaud, G.; Kokoh, K. B.; Beigsir, E. M., Electrochemical investigations of the oxidation-reduction of furfural in aqueous medium - Application to electrosynthesis. *Electrochimica Acta* **2004,** 49, (3), 397-403.
[8]. Green, S. K.; Lee, J.; Kim, H. J.; Tompsett, G. A.; Kim, W. B.; Huber, G. W., The Electrocatalytic Hydrogenation of Furanic Compounds in a Continuous Electrocatalytic Membrane Reactor. *Green Chemistry* **2013,** 15, (7), 1869-1879.
[9]. Liu, B.; Gao, F., Navigating glycerol conversion roadmap and heterogeneous catalyst selection aided by density functional theory: A review. *Catalysts* **2018,** 8, (2).
[10]. Pagliaro, M.; Ciriminna, R.; Kimura, H.; Rossi, M.; Della Pina, C., From glycerol to value-added products. *Angewandte Chemie-International Edition* **2007,** 46, (24), 4434-4440.
[11]. Quispe, C. A. G.; Coronado, C. J. R.; Carvalho, J. A., Glycerol: production, consumption, prices, characterization and new trends in combustion. *Renewable & Sustainable Energy Reviews* **2013,** 27, 475-493.
[12]. Ciriminna, R.; Della Pina, C.; Rossi, M.; Pagliaro, M., Understanding the glycerol market. *European Journal of Lipid Science and Technology* **2014,** 116, (10), 1432-1439.
[13]. Cortright, R. D.; Davda, R. R.; Dumesic, J. A., Hydrogen from catalytic reforming of biomass-derived hydrocarbons in liquid water. *Nature* **2002,** 418, 964.
[14]. Luo, N.; Fu, X.; Cao, F.; Xiao, T.; Edwards, P. P., Glycerol aqueous phase reforming for hydrogen generation over Pt catalyst – Effect of catalyst composition and reaction conditions. *Fuel* **2008,** 87, (17), 3483-3489.
[15]. Liu, B.; Greeley, J., Decomposition Pathways of Glycerol via C–H, O–H, and C–C Bond Scission on Pt(111): A Density Functional Theory Study. *The Journal of Physical Chemistry C* **2011,** 115, (40), 19702-19709.

[16]. Liu, B.; Greeley, J., Density functional theory study of selectivity considerations for C–C versus C–O bond scission in glycerol decomposition on Pt(111). *Topics in Catalysis* **2012,** 55, (5), 280-289.

[17]. Auneau, F.; Michel, C.; Delbecq, F.; Pinel, C.; Sautet, P., Unravelling the Mechanism of Glycerol Hydrogenolysis over Rhodium Catalyst through Combined Experimental–Theoretical Investigations. *Chemistry – A European Journal* **2011,** 17, (50), 14288-14299.

[18]. Maris, E. P.; Davis, R. J., Hydrogenolysis of glycerol over carbon-supported Ru and Pt catalysts. *Journal of Catalysis* **2007,** 249, (2), 328-337.

[19]. Shan, N.; Liu, B., Elucidating Molecular Interactions in Glycerol Adsorption at the Metal–Water Interface with Density Functional Theory. *Langmuir* **2018**.

[20]. Liu, B.; Greeley, J., A density functional theory analysis of trends in glycerol decomposition on close-packed transition metal surfaces. *Physical Chemistry Chemical Physics* **2013,** 15, (17), 6475-6485.

[21]. Chen, Y.; Salciccioli, M.; Vlachos, D. G., An efficient reaction pathway search method applied to the decomposition of glycerol on platinum. *The Journal of Physical Chemistry C* **2011,** 115, (38), 18707-18720.

[22]. Salciccioli, M.; Chen, Y.; Vlachos, D. G., Density Functional Theory-Derived Group Additivity and Linear Scaling Methods for Prediction of Oxygenate Stability on Metal Catalysts: Adsorption of Open-Ring Alcohol and Polyol Dehydrogenation Intermediates on Pt-Based Metals. *The Journal of Physical Chemistry C* **2010,** 114, (47), 20155-20166.

[23]. Coll, D.; Delbecq, F.; Aray, Y.; Sautet, P., Stability of intermediates in the glycerol hydrogenolysis on transition metal catalysts from first principles. *Physical Chemistry Chemical Physics* **2011,** 13, (4), 1448-1456.

[24]. García-Muelas, R.; López, N., Collective Descriptors for the Adsorption of Sugar Alcohols on Pt and Pd(111). *The Journal of Physical Chemistry C* **2014,** 118, (31), 17531-17537.

[25]. Tomasi, J.; Persico, M., Molecular-interactions in solution - an overview of methods based on continuous distributions of the solvent. *Chemical Reviews* **1994,** 94, (7), 2027-2094.

[26]. Cramer, C. J.; Truhlar, D. G., Implicit solvation models: equilibria, structure, spectra, and dynamics. *Chemical Reviews* **1999,** 99, (8), 2161-2200.

[27]. Schnur, S.; Groß, A., Properties of metal–water interfaces studied from first principles. *New Journal of Physics* **2009,** 11, (12), 125003.

[28]. Taylor, C. D.; Neurock, M., Theoretical insights into the structure and reactivity of the aqueous/metal interface. *Current Opinion in Solid State and Materials Science* **2005,** 9, (1), 49-65.

[29]. Markovic, N. M. P. N. R.; Ross, P. N., New electrocatalysts for fuel cells from model surfaces to commercial catalysts. *CATTECH* **2000,** 4, (2), 110-126.

[30]. Stamenkovic, V.; Mun Bongjin, S.; Mayrhofer Karl, J. J.; Ross Philip, N.; Markovic Nenad, M.; Rossmeisl, J.; Greeley, J.; Nørskov Jens, K., Changing the activity of electrocatalysts for oxygen reduction by tuning the surface electronic structure. *Angewandte Chemie* **2006,** 118, (18), 2963-2967.

[31]. Kyriakou, V.; Garagounis, I.; Vasileiou, E.; Vourros, A.; Stoukides, M., Progress in the electrochemical synthesis of ammonia. *Catalysis Today* **2017,** 286, 2-13.

[32]. Hori, Y.; Wakebe, H.; Tsukamoto, T.; Koga, O., Electrocatalytic Process of CO Selectivity in Electrochemical Reduction of CO_2 at Metal Electrodes in Aqueous Media. *Electrochimica Acta* **1994,** 39, (11), 1833-1839.

[33]. Nie, X.; Luo, W.; Janik, M. J.; Asthagiri, A., Reaction mechanisms of CO_2 electrochemical reduction on Cu(111) determined with density functional theory. *Journal of Catalysis* **2014,** 312, 108-122.

[34]. Lim, R. J.; Xie, M. S.; Sk, M. A.; Lee, J. M.; Fisher, A.; Wang, X.; Lim, K. H., A review on the electrochemical reduction of CO_2 in fuel cells, metal electrodes and molecular catalysts. *Catalysis Today* **2014,** 233, 169-180.

[35]. Zope, B. N.; Hibbitts, D. D.; Neurock, M.; Davis, R. J., Reactivity of the gold/water Interface during selective oxidation catalysis. *Science* **2010,** 330, (6000), 74-78.

[36]. Liu, B.; Zhou, M.; Chan, M. K. Y.; Greeley, J. P., Understanding polyol decomposition on bimetallic Pt-Mo catalysts - A DFT study of glycerol. *ACS Catalysis* **2015,** 5, (8), 4942-4950.

[37]. Klamt, A., The COSMO and COSMO-RS solvation models. *Wiley Interdisciplinary Reviews: Computational Molecular Science* **2018,** 8, (1), e1338.

[38]. te Velde, G.; Bickelhaupt, F. M.; Baerends, E. J.; Fonseca Guerra, C.; van Gisbergen, S. J. A.; Snijders, J. G.; Ziegler, T., Chemistry with ADF. *Journal of Computational Chemistry* **2001,** 22, (9), 931-967.

[39]. Jeong, K.-H.; Byun, B.-J.; Kang, Y.-K., Conformational preferences of glycerol in the gas phase and in water. *Bulletin of the Korean Chemical Society* **2012,** 33, (3), 917-924.

[40]. Fattebert, J. L.; Gygi, F., Density functional theory for efficient ab initio molecular dynamics simulations in solution. *Journal of Computational Chemistry* **2002,** 23, (6), 662-666.

[41]. Fattebert, J. L.; Gygi, F., First-principles molecular dynamics simulations in a continuum solvent. *International Journal of Quantum Chemistry* **2003,** 93, (2), 139-147.

[42]. Petrosyan, S. A.; Rigos, A. A.; Arias, T. A., Joint density-functional theory: *Ab initio* study of Cr_2O_3 surface chemistry in solution. *Journal of Physical Chemistry B* **2005,** 109, (32), 15436-15444.

[43]. Fishman, M.; Zhuang, H. L.; Mathew, K.; Dirschka, W.; Hennig, R. G., Accuracy of exchange-correlation functionals and effect of solvation on the surface energy of copper. *Physical Review B* **2013,** 87, (24), 245402.

[44]. Mathew, K.; Sundararaman, R.; Letchworth-Weaver, K.; Arias, T. A.; Hennig, R. G., Implicit solvation model for density-functional study of nanocrystal surfaces and reaction pathways. *The Journal of Chemical Physics* **2014,** 140, (8), 084106.

[45]. Garcia-Ratés, M.; López, N., Multigrid-Based methodology for implicit solvation models in periodic DFT. *Journal of Chemical Theory and Computation* **2016,** 12, (3), 1331-1341.

[46]. Iyemperumal Satish, K.; Deskins, N. A., Evaluating solvent effects at the aqueous/Pt(111) interface. *ChemPhysChem* **2017,** 18, (16), 2171-2190.

[47]. Thiel, P. A.; Madey, T. E., The interaction of water with solid-surfaces - fundamental-aspects. *Surface Science Reports* **1987,** 7, (6-8), 211-385.

[48]. Ogasawara, H.; Brena, B.; Nordlund, D.; Nyberg, M.; Pelmenschikov, A.; Pettersson, L. G. M.; Nilsson, A., Structure and bonding of water on Pt(111). *Physical Review Letters* **2002,** 89, (27), 276102.

[49]. Ogasawara, H.; Yoshinobu, J.; Kawai, M., Water-adsorption on Pt(111) - from isolated molecule to 3-dimensional cluster. *Chemical Physics Letters* **1994,** 231, (2-3), 188-192.

[50]. Carrasco, J.; Hodgson, A.; Michaelides, A., A molecular perspective of water at metal interfaces. *Nature Materials* **2012,** 11, 667.

[51]. Nie, S.; Feibelman, P. J.; Bartelt, N. C.; Thürmer, K., Pentagons and heptagons in the first water layer on Pt(111). *Physical Review Letters* **2010,** 105, (2), 026102.

[52]. Feibelman, P. J.; Bartelt, N. C.; Nie, S.; Thurmer, K., Interpretation of high-resolution images of the best-bound wetting layers on Pt(111). *Journal of Chemical Physics* **2010,** 133, (15).

[53]. Feibelman, P. J., Partial dissociation of water on Ru(0001). *Science* **2002,** 295, (5552), 99-102.

[54]. Forster, M.; Raval, R.; Hodgson, A.; Carrasco, J.; Michaelides, A., c(2 x 2) water-hydroxyl layer on Cu(110): a wetting layer stabilized by bjerrum defects. *Physical Review Letters* **2011,** 106, (4), 046103.

[55]. Desai, S. K.; Neurock, M., First-principles study of the role of solvent in the dissociation of water over a Pt-Ru alloy. *Physical Review B* **2003,** 68, (7), 075420.

[56]. Peterson, A. A.; Abild-Pedersen, F.; Studt, F.; Rossmeisl, J.; Nørskov, J. K., How copper catalyzes the electroreduction of carbon dioxide into hydrocarbon fuels. *Energy & Environmental Science* **2010,** 3, (9), 1311-1315.

[57]. Durand, W. J.; Peterson, A. A.; Studt, F.; Abild-Pedersen, F.; Nørskov, J. K., Structure effects on the energetics of the electrochemical reduction of CO_2 by copper surfaces. *Surface Science* **2011,** 605, (15), 1354-1359.

[58]. Peterson, A. A.; Nørskov, J. K., Activity Descriptors for CO_2 Electroreduction to Methane on Transition-Metal Catalysts. *Journal of Physical Chemistry Letters* **2012,** 3, (2), 251-258.

[59]. Shi, C.; Chan, K.; Yoo, J. S.; Nørskov, J. K., Barriers of electrochemical CO_2 reduction on transition metals. *Organic Process Research & Development* **2016,** 20, (8), 1424-1430.

[60]. Hussain, J.; Skúlason, E.; Jónsson, H., Computational study of electrochemical CO_2 reduction at transition metal electrodes. *Procedia Computer Science* **2015,** 51, 1865-1871.

[61]. Skúlason, E.; Jónsson, H., Atomic scale simulations of heterogeneous electrocatalysis: Recent advances. *Advances in Physics: X* **2017,** 2, (3), 481-495.

[62]. Nie, X.; Esopi, M. R.; Janik, M. J.; Asthagiri, A., Selectivity of CO_2 reduction on copper electrodes: The role of the kinetics of elementary steps. *Angewandte Chemie International Edition* **2013,** 52, (9), 2459-2462.

[63]. Skulason, E.; Karlberg, G. S.; Rossmeisl, J.; Bligaard, T.; Greeley, J.; Jonsson, H.; Norskov, J. K., Density functional theory calculations for the hydrogen evolution reaction in an electrochemical double layer on the Pt(111) electrode. *Physical Chemistry Chemical Physics* **2007,** 9, (25), 3241-3250.

[64]. Skulason, E.; Tripkovic, V.; Bjorketun, M. E.; Gudmundsdottir, S.; Karlberg, G.; Rossmeisl, J.; Bligaard, T.; Jonsson, H.; Norskov, J. K., Modeling the electrochemical hydrogen oxidation and evolution reactions on the basis of density functional theory calculations. *Journal of Physical Chemistry C* **2010,** 114, (42), 18182-18197.

[65]. Hartnig, C.; Grimminger, J.; Spohr, E., Adsorption of formic acid on Pt(111) in the presence of water. *Journal of Electroanalytical Chemistry* **2007,** 607, (1), 133-139.

[66]. Zhang, Y.-C.; Ren, R.-P.; Liu, S.-Z.; Zuo, Z.-J.; Lv, Y.-K., Theoretical study on the influence of a secondary metal on the Cu(110) surface in the presence of H_2O for methanol decomposition. *RSC Advances* **2016,** 6, (18), 15127-15136.

[67]. Michel, C.; Auneau, F.; Delbecq, F.; Sautet, P., C–H versus O–H bond dissociation for alcohols on a Rh(111) surface: a strong assistance from hydrogen bonded neighbors. *ACS Catalysis* **2011,** 1, (10), 1430-1440.

[68]. Garcia-Ratés, M.; García-Muelas, R.; López, N., Solvation effects on methanol decomposition on Pd(111), Pt(111), and Ru(0001). *The Journal of Physical Chemistry C* **2017,** 121, (25), 13803-13809.
[69]. Shustorovich, E., Activation Barrier for Adsorbate Surface Diffusion, Heat of Chemisorption, and Adsorbate Registry: Theoretical Interrelations. *Journal of the American Chemical Society* **1984,** 106, (22), 6479-6481.
[70]. Shustorovich, E.; Sellers, H., The UBI-QEP method: a practical theoretical approach to understanding chemistry on transition metal surfaces. *Surface Science Reports* **1998,** 31, (1-3), 1-119.
[71]. Kua, J.; Faglioni, F.; Goddard, W. A., Thermochemistry for hydrocarbon intermediates chemisorbed on metal surfaces: $CH_{n-m}(CH_3)_m$ with n=1, 2, 3 and m $\leqslant$ n on Pt, Ir, Os, Pd, Ph, and Ru. *Journal of the American Chemical Society* **2000,** 122, (10), 2309-2321.
[72]. Abild-Pedersen, F.; Greeley, J.; Studt, F.; Rossmeisl, J.; Munter, T. R.; Moses, P. G.; Skulason, E.; Bligaard, T.; Nørskov, J. K., Scaling properties of adsorption energies for hydrogen-containing molecules on transition-metal surfaces. *Physical Review Letters* **2007,** 99, (1), 016105-016101.
[73]. Bodenschatz, C. J.; Sarupria, S.; Getman, R. B., Molecular-level details about liquid H_2O interactions with co and sugar alcohol adsorbates on Pt(111) calculated using density functional theory and molecular dynamics. *The Journal of Physical Chemistry C* **2015,** 119, (24), 13642-13651.
[74]. Xie, T.; Sarupria, S.; Getman, R. B., A DFT and MD study of aqueous-phase dehydrogenation of glycerol on Pt(111): Comparing chemical accuracy versus computational expense in different methods for calculating aqueous-phase system energies. *Molecular Simulation* **2017,** 43, (5-6), 370-378.
[75]. Kresse, G.; Hafner, J., Ab *initio* molecular dynamics for open shell transition metals. *Physical Review B* **1993,** 48, (17), 13115-13118.
[76]. Kresse, G.; Furthmuller, J., Efficiency of *Ab initio* Total Energy Calculations for Metals and Semiconductors using A Plane-wave Basis Set. *Computational Materials Science* **1996,** 6, (1), 15-50.
[77]. Monkhorst, H. J.; Pack, J. D., Special Points for Brillouin Zone Integrations. *Physical Review B* **1976,** 13, (12), 5188-5192.
[78]. Kiran, M.; Ravishankar, S.; Kendra, L.-W.; Arias, T. A.; Richard, G. H., Implicit solvation model for density-functional study of nanocrystal surfaces and reaction pathways. *The Journal of Chemical Physics* **2014,** 140, (8), 084106.
[79]. Tereshchuk, P.; Da Silva, J. L. F., Density functional investigation of the adsorption of ethanol–water mixture on the Pt(111) surface. *The Journal of Physical Chemistry C* **2013,** 117, (33), 16942-16952.
[80]. Tereshchuk, P.; Chaves, A. S.; Da Silva, J. L. F., Glycerol adsorption on platinum surfaces: a density functional theory investigation with van der waals corrections. *The Journal of Physical Chemistry C* **2014,** 118, (28), 15251-15259.
[81]. Fernández, P. S.; Fernandes Gomes, J.; Angelucci, C. A.; Tereshchuk, P.; Martins, C. A.; Camara, G. A.; Martins, M. a. E.; Da Silva, J. L. F.; Tremiliosi-Filho, G., Establishing a link between well-ordered Pt(100) surfaces and real systems: how do random superficial defects influence the electro-oxidation of glycerol? *ACS Catalysis* **2015,** 5, (7), 4227-4236.
[82]. Fernández, P. S.; Tereshchuk, P.; Angelucci, C. A.; Gomes, J. F.; Garcia, A. C.; Martins, C. A.; Camara, G. A.; Martins, M. a. E.; Da Silva, J. L. F.; Tremiliosi-Filho, G., How do random

superficial defects influence the electro-oxidation of glycerol on Pt(111) surfaces? *Physical Chemistry Chemical Physics* **2016,** 18, (36), 25582-25591.

[83]. Amaral, R. C.; Tereshchuk, P.; Seminovski, Y.; Da Silva, J. L. F., The role of low-coordinated sites on the adsorption of glycerol on defected Pt_n/Pt(111) substrates: a density functional investigation within the D3 van der waals correction. *The Journal of Physical Chemistry C* **2017,** 121, (6), 3445-3454.

[84]. Tereshchuk, P.; Amaral, R. C.; Seminovski, Y.; Da Silva, J. L. F., Glycerol adsorption on a defected Pt_6/Pt(100) substrate: a density functional theory investigation within the D3 van der Waals correction. *RSC Advances* **2017,** 7, (28), 17122-17127.

[85]. Phatak, A. A.; Delgass, W. N.; Ribeiro, F. H.; Schneider, W. F., Density functional theory comparison of water dissociation steps on Cu, Au, Ni, Pd, and Pt. *The Journal of Physical Chemistry C* **2009,** 113, (17), 7269-7276.

[86]. Zhou, M.; Liu, B., DFT investigation on the competition of the water–gas shift reaction versus methanation on clean and potassium-modified nickel(1 1 1) surfaces. *Chemcatchem* **2015,** 7, (23), 3928-3935.

[87]. Michaelides, A., Density functional theory simulations of water–metal interfaces: Waltzing waters, a novel 2D ice phase, and more. *Applied Physics A* **2006,** 85, (4), 415-425.

[88]. Tereshchuk, P.; Da Silva, J. L. F., Ethanol and water adsorption on close-packed 3d, 4d, and 5d transition-metal surfaces: a density functional theory Investigation with van der Waals correction. *The Journal of Physical Chemistry C* **2012,** 116, (46), 24695-24705.

[89]. Crotti, C.; Kaspar, J.; Farnetti, E., Dehydrogenation of glycerol to dihydroxyacetone catalyzed by iridium complexes with P-N ligands. *Green Chemistry* **2010,** 12, (7), 1295-1300.

[90]. Hakim, S. S. M. A.; S., T. A.; Kenichi, K.; Takashi, T.; Ken-ichi, S., Oxidant-free Dehydrogenation of Glycerol to Lactic Acid by Heterogeneous Platinum Catalysts. *Chemcatchem* **2017,** 9, (14), 2816-2821.

Chapter 5 - Ammonia Synthesis on Mn_4N

Chapter 5 is adapted with permission from:

Shan, N.; Chikan, V.; Pfromm, P; Liu, B. "Fe and Ni dopants facilitating ammonia synthesis on Mn_4N and mechanistic insights from first-principles methods", *Journal of Physical Chemistry C*, 2018, *122*(11), 6109–6116.

5.1 Introduction

Ammonia is the backbone of today's economy due to its use in agriculture that supports almost half the world's population [1]. The Haber-Bosch process accounts for most of the ammonia production and consumes more than 1% of the global energy use [2]. Ammonia synthesis based on Haber-Bosch (at pressures up to 300 bar and temperatures up to 500 °C) is an energy-intensive process. In the last few decades, alternative solutions for ammonia synthesis using electrochemical [3, 4], or photocatalytic [5] methods have been explored. Steinfeld and co-workers demonstrated a two-step solar-driven cyclic process for NH_3 synthesis [6-8], in which aluminum oxide (Al_2O_3) was firstly reduced by N_2 to form aluminum nitride (AlN), which then reacts with water to produce NH_3. The reduced nitride can be recycled to participate in nitridation in the next cycle. While the reaction was conducted at ambient pressure, high temperature (1000 – 2000 °C) was required to reduce Al_2O_3.

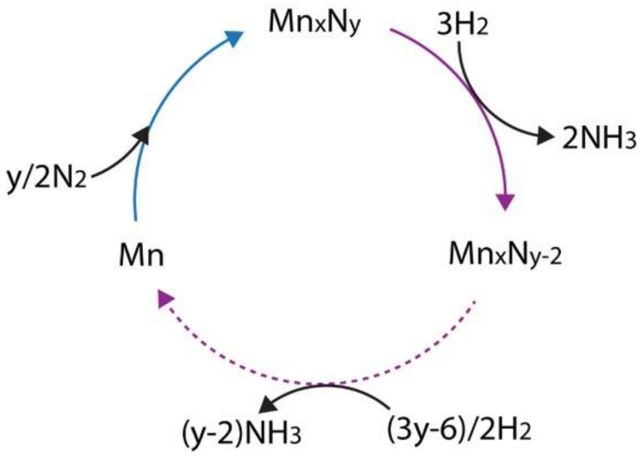

Figure 5.1 Nitridation (in blue) and reduction (in purple) cycle describing manganese nitride (Mn_xN_y) and ammonia (NH_3) formation for step-catalysis process. Adapted with permission from Ref [9]. Copyright 2018, American Chemical Society.

Nitrides based on transition metals (e.g., Cr, Mn and Fe) have been extensively examined experimentally in our previous work to generate NH_3 with H_2 [10-12]. It is concluded that manganese nitride was most promising due to relatively favorable nitridation and reduction thermodynamics. The nitridation and reduction cycle involving manganese nitrides is schematically shown in Figure 5.1. The stoichiometry is included as coefficient for each main species. Complete reduction to pure Mn is represented by the dashed line. Moreover, the electronic structures of metal nitrides (such as Mn_2N and Sr_2N) were also explored using density functional theory (DFT) calculations in relation to metal nitridation and NH_3 production [13]. It has also been shown that nitrogen vacancy formation energy can be used as the descriptor to characterize nitride activity. To tune the activity of metal nitride, doping of Mn_2N with different metals, including Sc, Ti, V, Cr, Fe, Co, Ni, Cu and Zn, have been evaluated [14], indicating that the local electronic structure of Fe-doped Mn_2N destabilizes lattice nitrogen, and facilitates the extraction of lattice nitrogen to produce NH_3. More recently, Group III–VII transition metal mononitrides have also been investigated for applications in electrochemical synthesis of ammonia, which could expand the utilization of metal nitrides for NH_3 production [15-18].

Although experiments indicated manganese nitrides are promising nitrogen carriers for ammonia synthesis [13, 14], an avenue to evaluate their performance remains missing. This will further hinder the improvement of manganese nitrides for ammonia synthesis by chemical doping or alloying. Mn_4N is an ideal starting-point material to tackle this issue. First, Mn_4N, along with $Mn_6N_{2.58}$, exists as one of manganese-based nitride phases involved in the cyclic transformation (see Figure 5.1), as observed by Michalsky and Pfromm [12, 13]. Second, Mn_4N has a simple face-centered cubic crystal structure (Figure 5.2(a)). Both its crystallographic and magnetic properties have been well documented, compared to other phases especially $Mn_6N_{2.58}$ [19, 20].

This study aims to provide detailed molecular mechanisms describing NH_3 production based on the Mn_4N phase of manganese nitride using DFT. Using the established reaction thermodynamics on the selected pure Mn_4N, suggestions have been made to tune the properties of Mn_4N with Fe and Ni dopant. Brønsted–Evans–Polanyi (BEP) relationship and linear scaling relationship have been developed to reveal the reaction kinetic and energetic trends for a series of doped Mn_4N as guidance for novel materials design.

5.2 Computational Details

Spin-polarized DFT calculations were performed using the Vienna Ab initio Simulation Package (VASP) [21, 22]. The electron-electron exchange-correlation energies were determined with generalized gradient approximation Perdew-Burke-Ernzerhof (GGA-PBE) functional [23]. The projector augmented-wave (PAW) method [24] was used to describe electron-ion interactions.

The Mn_4N nitride phase has a face-centered-cubic bulk structure [19, 25], shown in Figure 5.2(a). The bulk was optimized with a plane-wave cutoff energy of 420 eV, and a 16×16×16

Monkhorst-Pack k-point mesh [26]. The lattice constant was converged to 3.74 Å and the calculated magnetic moments are 3.31 μ_B for Mn(I) and -0.90 μ_B for Mn(II), respectively (labelled in Figure 5.2(a)). These values are in good agreement with corresponding experimental values, i.e. 3.86 Å, 3.85 μ_B and -0.9 μ_B [19]. Potential self-interaction errors (SIE) for Mn_4N were also considered by performing GGA+U calculations. The calculated results with various U values indicate that standard DFT calculations (very small U) can adequately account for the structural and magnetic properties of Mn_4N.

A 4-layer, (1 × 1) $Mn_4N(111)$ slab was employed for periodic DFT calculations. The bottom two layers were fixed to the optimized bulk value. The first Brillouin-Zone of such a slab is sampled with a 4×4×1 Monkhorst-pack k-point mesh. The cutoff energy for the plane waves basis set was set to be 380 eV for slab models. Self-consistent iterations were converged up to 1×10^{-6} eV, while the ionic steps were converged when the force on each atom is less than 0.02 eV/Å. Dipole corrections were included in all slab calculations.

Climbing image nudged elastic band (CI-NEB) [27] and dimer methods [28] were employed in search of the transition state of an elementary reaction step. A 5-layer slab with first three layers relaxing was used for transition state searching. The reaction free energies (ΔG) were estimated based on $\Delta G = \Delta E + \Delta ZPE - T\Delta S$, where ΔE, ΔZPE, and $T\Delta S$ represent the electronic energy, zero point energy, and entropy terms, respectively. Vibrational frequencies were calculated using simple harmonic approximations. The entropy is estimated using standard statistical mechanical approach and computational details have been discussed in our previous work [29, 30].

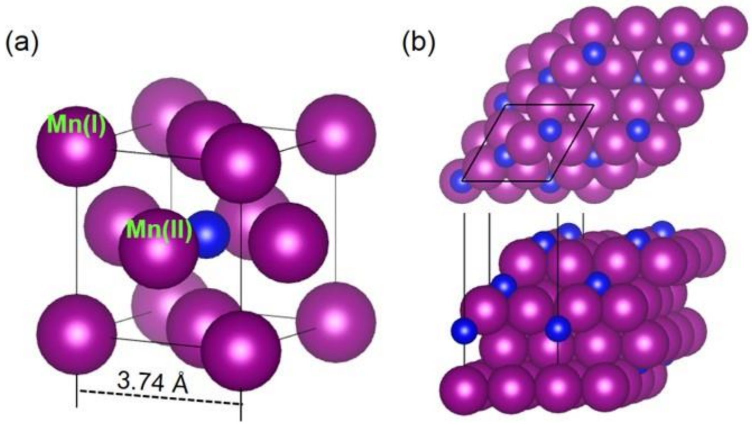

Figure 5.2 (a) Optimized bulk structure of the Mn_4N phase of manganese nitride, two types of Mn atoms (I) and (II) are labelled. The lattice parameter of the cubic conventional cell is indicated. (b) The top (upper) and side (lower) views of N-terminated Mn_4N close-packed (111) surface. Mn and N are in magenta and blue, respectively. Black lines represent the periodic boundaries of the p(1x1) unit cell of the Mn_4N (111) facet. Adapted with permission from Ref [9]. Copyright 2018, American Chemical Society.

In a similar manner to the Mars-van Krevelen mechanism [31], the top layer lattice N atom directly participates in NH_3 production and will be consumed on the surface. Sublayer lattice N atom diffuses onto the surface enabling continuous ammonia synthesis. In this work, reaction energy of N diffusion ($E_{r\ vac}$), diffusion barrier of sublayer lattice N ($E_{a\ vac}$), binding energy of N ($E_{N\ vac}$), and adsorption energy of NH_x (E_{ads}, x=1, 2), are defined in Equations (45-48):

$$E_{r\ vac} = E_{FS} - E_{IS} \tag{45}$$

$$E_{a\ vac} = E_{TS} - E_{IS} \tag{46}$$

$$E_{N\ vac} = E_N^* - E_{vac}^* - \frac{1}{2}E_{N_2(gas)} \tag{47}$$

$$E_{ads} = E^{*}_{NH_x} - E^{*}_{vac} - E_{NH_x(gas)} \tag{48}$$

where the asterisk (*) suggests the open surface site. E_{IS}, E_{TS} and E_{FS} are the energies of the initial state (IS), transition state (TS) and final state (FS) of N diffusion, respectively. Herein, initial state denotes the slab with N atom in the sublayer, whereas final state denotes the slab with a sublayer N vacancy. Configurations corresponding to these reaction states are shown in Figure 5.3(a-b). E^{*}_{vac} (Figure 5.3(c)) is the energy of surface with a N vacancy on the surface, E^{*}_{N} (Figure 5.2(b)) and $E^{*}_{NH_x}$ (x = 1, 2) represent total energies of the slabs with N and NH_x on the surface, and $E_{N_2(gas)}$ and $E_{NH_x(gas)}$ are the energies of N_2 and NH_x in the vacuum.

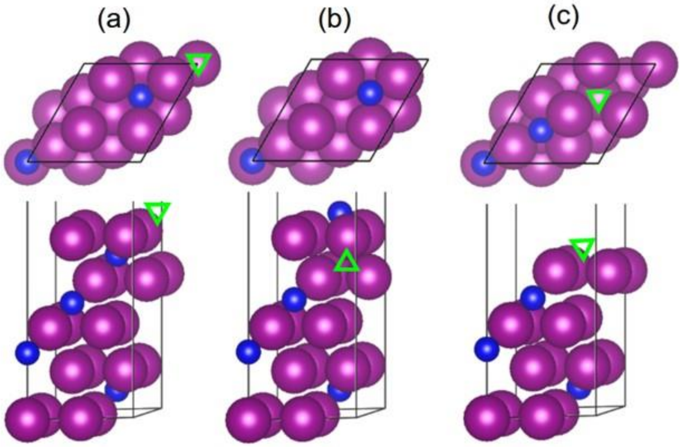

Figure 5.3 The (a) initial state (IS), (b) final state (FS) of sublayer lattice N diffusion, and (c) surface N vacancy. Surface N vacancy site is shown with a downward green triangle, while sublayer N vacancy is indicated with an upward green triangle. Mn and N are in magenta and blue, respectively. Black lines represent the periodic boundaries of the *p*(1x1) unit cell. Adapted with permission from Ref [9]. Copyright 2018, American Chemical Society.

5.3 Theoretical Modeling of NH_3 Production with Step-Catalysis

5.3.1 Properties of Mn_4N

Asymmetric surface terminations can result from the cleavage of Mn_4N, as illustrated in Figure 5.2(b), i.e., N-terminated surface and Mn-terminated surface. The N-terminated surface was chosen as the reference so that the first reduction step begins with the surface N.

The atomic H prefers to bind 3-fold site on pure $Mn_4N(111)$, while NH^*, NH_2^* and NH_3^* prefer to bind on the 3-fold, bridge and top site, respectively. The reaction scheme describing the first NH_3 molecule formation can be expressed by steps (R11-R15), where 'g', and 'v' represent the gas phase and N vacancy site, respectively. In this study, the reduction sequence is assumed to start with gaseous H_2 dissociative adsorption forming H^* (shown in step R11). The adsorbed hydrogen atoms (H^*) then combine with N on $Mn_4N(111)$ stepwise to produce NH_3^*, as represented by R12-R14. NH_3^* desorbs leaving a vacancy ($(v)_t$) on $Mn_4N(111)$ surface, as in step R15. Additional N will be provided via diffusions of $N_{(s)}$ on the sublayer in the Mn_4N sublayer lattice (R16).

$$\frac{1}{2}H_{2(g)} + * \rightarrow H^* \tag{R11}$$

$$H^* + N_{(t)} \rightarrow NH^* \tag{R12}$$

$$NH^* + H^* \rightarrow NH_2^* + * \tag{R13}$$

$$NH_2^* + H^* \rightarrow NH_3^* + * \tag{R14}$$

$$NH_3^* \rightarrow NH_{3(g)} + *(v)_t \tag{R15}$$

$$N_{(s)} + \ *(v)_t \rightarrow N_{(t)} + *(v)_s \tag{R16}$$

In order to control the reaction proceeding toward ammonia production, experiment has to be carried out at elevated temperatures, sometimes up to 700 °C, and 1 bar [13]. In addition, the produced NH_3 needs to be extracted continuously, shifting the equilibrium toward NH_3 formation.

Here, the reaction free energies, estimated at 700 °C and 1 bar for the reduction of stoichiometric Mn_4N at its close-packed (111) facet, are shown in Figure 5.4. This reaction condition was determined according to the experimental work reported in Ref [13]. Clean surface (Figure 5.2(b)) and gas phase H_2 were used as the zero energy reference state (note: nitrogen is supplied by Mn_4N). Optimized geometries of reaction intermediates at their preferred sites are illustrated in top panels of Figure 5.4. The process to produce two NH_3 is expressed according to the stoichiometry of $3H_{2(g)} + 2N_{(lat)} \rightarrow 2NH_{3(g)}$, utilizing one top-layer lattice N ($N_{(t)}$) and one sublayer lattice N ($N_{(s)}$).

On Mn_4N(111), hydrogen dissociative adsorption (R11) is endergonic (0.26 eV/H atom). The formation of NH* (R12) is an exergonic step (-0.33 eV) resulting in one N–H bond formation. Subsequent NH_2* and NH_3* formations are also endergonic (at respective 0.83 and 0.66 eV). The release of NH_3 is an exergonic step (-0.68 eV), mainly due to the gain of entropy. Once the original $N_{(t)}$ is consumed, the lattice N in the sublayer is expected to diffuse onto the surface, overcoming an energy barrier of 1.12 eV. Hence, as shown in Figure 5.4, the reduction sequences between each NH_3 production being considered are connected by one step of lattice N diffusion from the sublayer onto the top layer (R16). This nitrogen transport step is crucial as it ensures the supply of N species for continuous NH_3 formation. With the formation of a new $N_{(t)}$ species, a sublayer nitrogen vacancy, $(v)_s$, is formed at the same time. In the second NH_3 formation sequence, hydrogen dissociative adsorption is slightly endergonic (0.02 eV). The corresponding free energies for NH*, NH_2*, and NH_3* formations are 0.23, 1.06, and 0.27 eV, respectively. It can be noted that the formation of NH* becomes more endergonic compared to the same step in the first sequence. It is also interesting to note that the formation of second NH_3 becomes less endergonic (0.27 vs. 0.66 eV). The observed variations in the reaction free energies can be considered as the influence of the sublayer nitrogen vacancy, $(v)_s$. Overall, the formation of the second NH_3 is still an endergonic process.

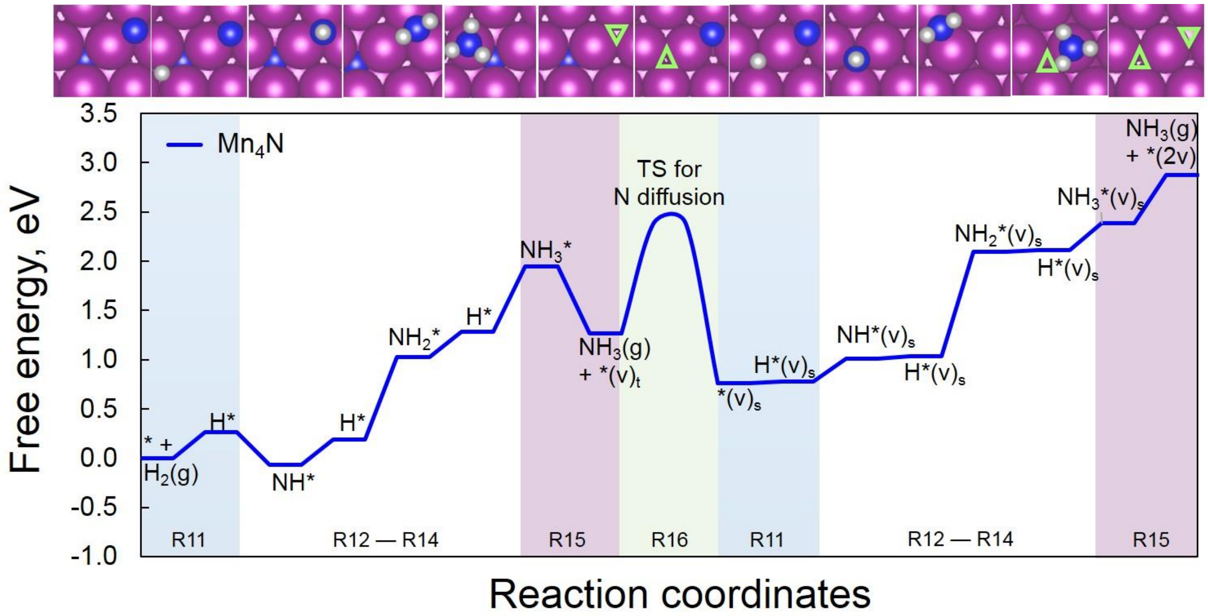

Figure 5.4 Free energy diagram for Mn_4N(111) surface reduction by H_2 (two NH_3 molecules produced based on the stoichiometry of $3H_{2(g)} + 2N_{(lat)} \rightarrow 2NH_{3(g)}$ at 700 °C and 1 bar. Optimized structures corresponding to each intermediate elementary step are also shown. Surface N vacancy site is shown with a downward green triangle, while sublayer N vacancy site is indicated with an upward green triangle. The vacancy sites are not shown for N*, NH*, and NH_2*, as they are underneath the adsorbates and hidden. Mn, N, and H are in magenta, blue and grey, respectively. Adapted with permission from Ref [9]. Copyright 2018, American Chemical Society.

According to the proposed mechanism (R11-R16), two potential performance-limiting factors influencing NH_3 formation activity have been identified: (1) binding energies of $H/NH_2/NH_3$ on Mn_4N surfaces, and (2) sublayer lattice N diffusion barrier ($E_{a\,vac}$). The first factor can influence the overall NH_3 formation free energy ($\Delta G_{NH_3^*}$), whereas the second factor determines the kinetics of nitrogen-supply to the surface. With the pure Mn_4N model, lower both $\Delta G_{NH_3^*}$ and $E_{a\,vac}$ will improve manganese nitride performance in favor of NH_3 formation on the thermodynamic and kinetic aspects.

5.3.2 Behaviors of Mn_4N Doped with Fe and Ni

Doped manganese nitride showed the enhanced activity for ammonia synthesis experimentally [14]. Given the weaker bonding strength with nitrogen in the nitride phase, Fe and Ni have been selected as candidates to tune the electronic properties of manganese nitride to increase the yield of ammonia. The top and side views of doped models are depicted in Figure 5.5(a-b). In the structure with single Fe atom dopant, the Mn atom is substituted in either the sublayer or the top layer, denoted by $Fe_s@Mn_4N$ and $Fe_t@Mn_4N$, respectively. Similarly, Ni-doped Mn_4N was denoted by $Ni_s@Mn_4N$ and $Ni_t@Mn_4N$. Free energies diagrams (at 700 °C and 1 bar) for the reductions of the Fe-doped Mn_4N nitrides ($Fe_s@Mn_4N$ and $Fe_t@Mn_4N$) are shown in Figure 5.6, where the free energies for pure Mn_4N system (blue dashed lines) are included as a reference system.

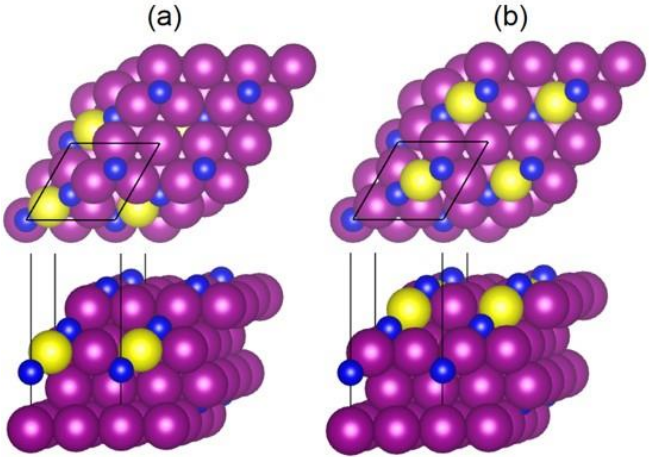

Figure 5.5 Top and side views of (a) sublayer, (b) top layer doped $Mn_4N(111)$ surface models with the N-termination. Mn, N, and the dopant atom are in magenta, blue, and yellow, respectively. Black lines represent the periodic boundaries of the *p*(1x1) unit cell. Adapted with permission from Ref [9]. Copyright 2018, American Chemical Society.

On $Fe_s@Mn_4N$, free energies for elementary steps of R11–R15 in the first NH_3 formation sequence show negligible variations from those on pure Mn_4N (i.e., green versus blue dashed paths). Optimized structures on preferred sites of H*, NH*, NH_2*, and NH_3* resemble closely to those obtained on pure $Mn_4N(111)$. This behavior indicates that, with Fe in the sublayer, the impact on the interactions between H*, and NH_x* (x=1, 2, 3) intermediates with top-layer Mn atoms, in terms of Mn–H and Mn–N bond strength, is negligible.

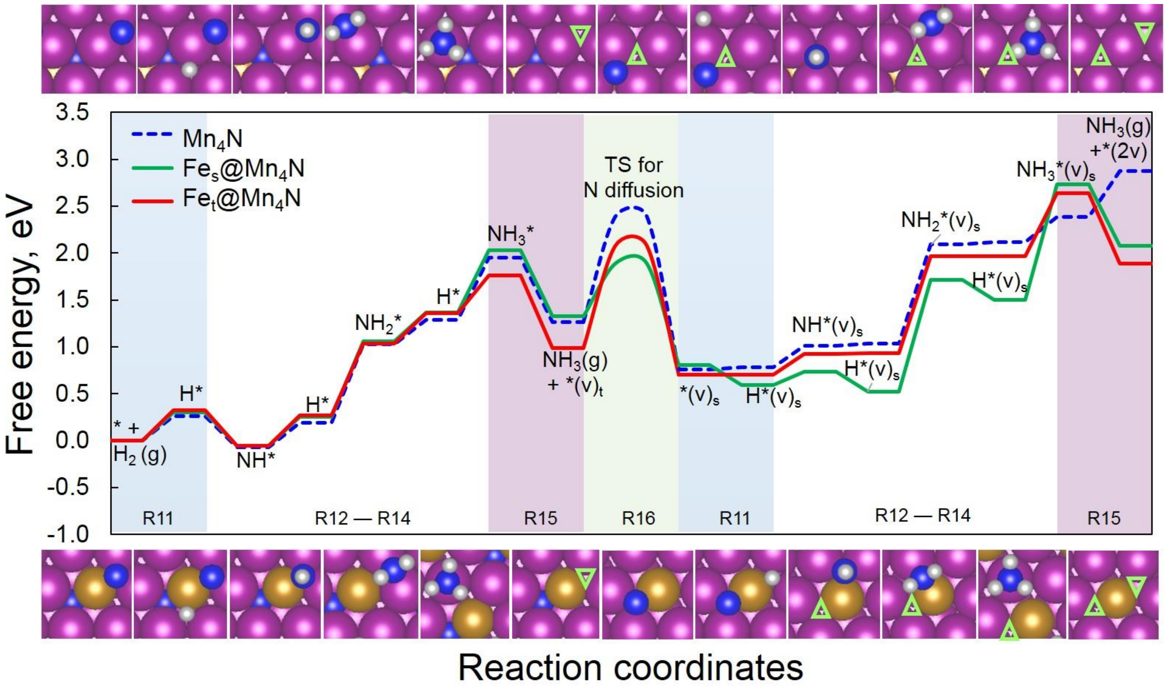

Figure 5.6 Free energy diagrams for the reduction of pure Mn_4N (blue dashed lines), Fe_s@Mn_4N (green), and Fe_t@Mn_4N (red) at 700 °C and 1 bar. Similarly, optimized structures for each intermediate step on the close-packed surface of Fe_s@Mn_4N (top panels) and Fe_t@Mn_4N (bottom panels) are shown. Surface N vacancy is represented with a downward green triangle, while the sublayer N vacancy is represented with an upward green triangle. Mn, Fe, N, and H are in magenta, gold, blue, and grey, respectively. Adapted with permission from Ref [9]. Copyright 2018, American Chemical Society.

Nevertheless, the energy barrier ($E_{a\,vac}$) for Step R16, involving the doped sublayer Fe atom, is lowered from 1.12 eV (Figure 5.7(a)) to 0.56 eV (Figure 5.7(b)), suggesting that the sublayer Fe facilitates the diffusion of $N_{(s)}$ onto the surface. For $N_{(s)}$ to move onto the top layer, this nitrogen atom is required to break the bond with the neighbor atoms (Mn or dopant) in the second-layer. Since the Fe-N bond is weaker than the Mn-N bond [14], the required energy that contributes to the overall energy barrier is expected to be lower. Moreover, at the transition state and its proximity (in Figure 5.7(b)), the surface Mn atom is noticeably distorted from its normal lattice position, thus, the mechanical hindrance for the diffusion of the $N_{(s)}$ species can also be minimized.

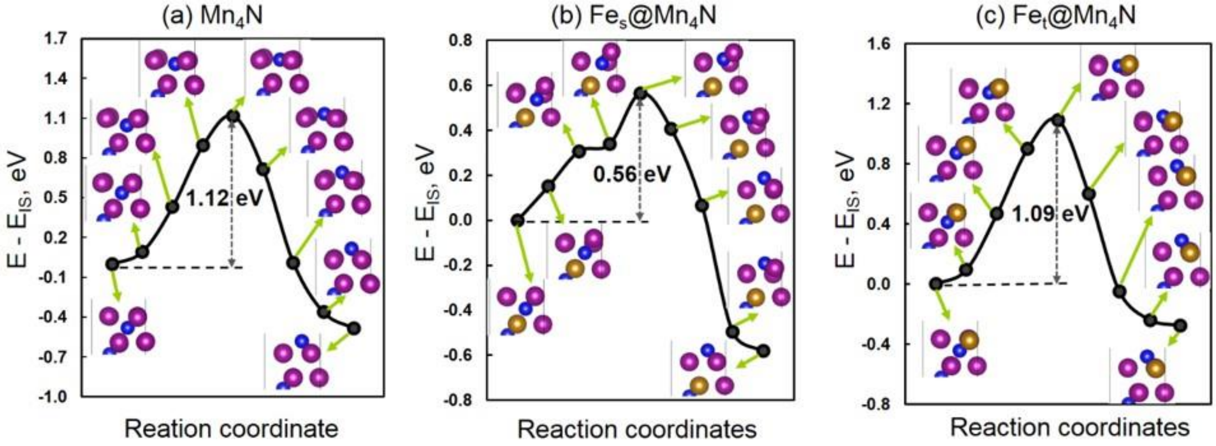

Figure 5.7 Potential energy surfaces for diffusions of N(s) from sublayer to surface on (a) pure Mn_4N, (b) $Fe_s@Mn_4N$, and (c) $Fe_t@Mn_4N$. The total energy of the initial state (E_{IS}) is chosen as the energy reference. The snapshot image corresponding to each intermediate state is shown. Mn, Fe, Ni, and N are in magenta, gold, green, and blue, respectively. Adapted with permission from Ref [9]. Copyright 2018, American Chemical Society.

Once a new $N_{(t)}$ becomes available, the second reduction sequence continues by following Steps R11-R15. According to Figure 5.6 (green), the dissociative adsorption of hydrogen (R11) becomes exergonic (-0.22 eV). The free energy for this step is over 0.5 eV lower than that in the first reduction cycle (0.30 eV). Although NH*, NH_2* formations (R12 and R13) are still endergonic (0.15 and 1.19 eV), the overall free energies for the second reduction circle becomes much less endergonic than on pure Mn_4N due to the more favorable H binding. NH_3* formation on $Fe_s@Mn_4N$ is more endergonic (1.23 eV) than that on pure Mn_4N (0.27 eV). Unlike Mn_4N, the second NH_3 release step (R15) is exergonic by -0.66 eV (versus 0.49 eV on pure Mn_4N surface). This, again, can be attributed to Fe doping, as the Fe–N bond is weaker than the Mn-N bond, and the reduction of iron nitrides tends to be more thermodynamically favorable [13].

On $Fe_t@Mn_4N$ (the red path in Figure 5.6), a surface Mn atom is substituted by one Fe atom. The hydrogen dissociative adsorption (R11) becomes slightly less favorable than on pure Mn_4N (0.33 versus 0.26 eV), where the dissociated H atom binds at the 3-fold site consisting of the surface Fe dopant. However, formations of NH* and NH_2* (R12 and R13) become slightly more favorable with free energies of -0.38 eV and 0.76 eV compared to corresponding steps on pure Mn_4N (-0.33 eV and 0.83 eV), respectively. As shown in bottom panels of Figure 5.6, NH* and NH_2* bind in the proximity to the surface Fe. Similarly, the NH_3* formation (R14) becomes thermodynamically favored as free energy is lowered from 0.66 eV (on pure Mn_4N) to 0.40 eV.

The energy barrier for $N_{(s)}$ diffusion ($E_{a\ vac}$) is 1.09 eV in $Fe_t@Mn_4N$, only slightly lower than in pure Mn_4N (1.12 eV). As shown in Figure 5.7(c), $N_{(s)}$ needs to break the Mn–N bond with the Mn atom in the sublayer in order to diffuse onto the surface, whereas the Fe-N bond is retained. In addition, no dislocation of surface atoms near the transition state is observed.

Although the surface Fe dopant does not enhance the lattice N diffusion as $Fe_s@Mn_4N$, the free energies for the second reduction cycle become more thermodynamically favored than pure Mn_4N, especially for the release the second NH_3 (-0.75 vs. 0.49 eV on pure Mn_4N). This means that Fe-doping can indeed reduce the endergonicity of ammonia formation regardless of the doping location. Furthermore, it can be expected that Mn_4N modified with elements forming weaker bonds with nitrogen can achieve the similar effects.

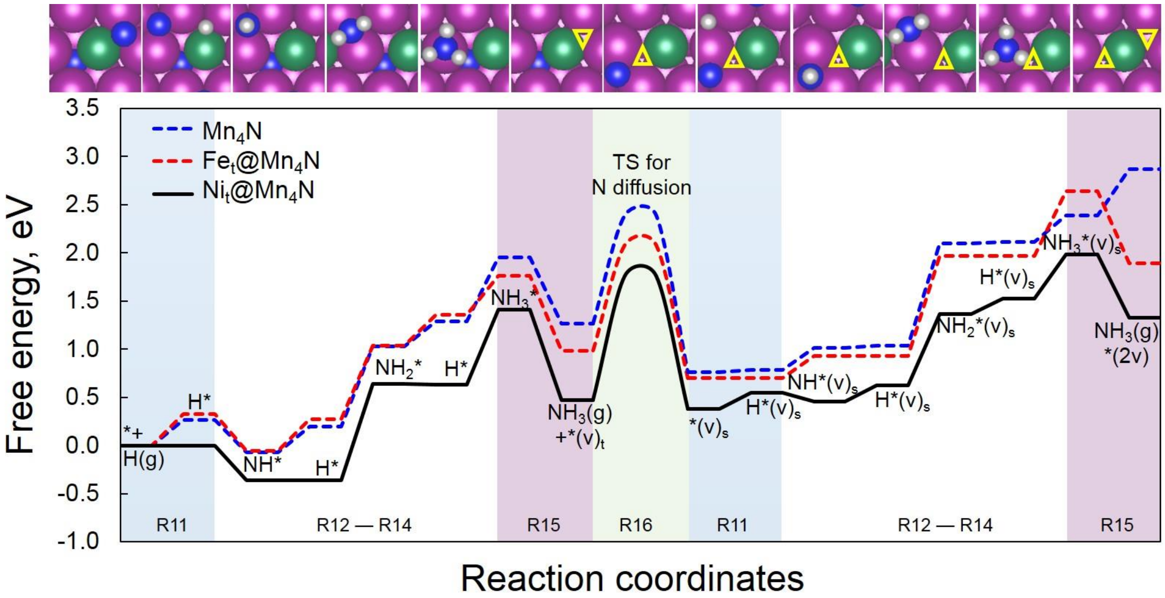

Figure 5.8 Free energy diagrams for the reduction of pure Mn_4N (blue dashed lines), $Fe_t@Mn_4N$ (red dashed lines), and $Ni_t@Mn_4N$ (black) at 700 °C and 1 bar. Similarly, optimized structures for intermediate steps on the close-packed surface of $Ni_t@Mn_4N$ (top panels) are shown. Surface N vacancy is represented with a downward yellow triangle, while the sublayer N vacancy is represented with an upward yellow triangle. Mn, Ni, N, and H are in magenta, green, blue and grey, respectively. Adapted with permission from Ref [9]. Copyright 2018, American Chemical Society.

While Fe-doping provides the means to lower the overall NH_3 formation endergonicity, modification of Mn_4N by tuning the hydrogen dissociative adsorption step (R11) would, in principle, further enhance ammonia formation by shifting the overall reaction toward the thermodynamically favored direction. In this case, Ni (with stronger Ni–H bonding) has been selected to tune Mn_4N via similar substitutions of the sublayer and the top-layer Mn atoms.

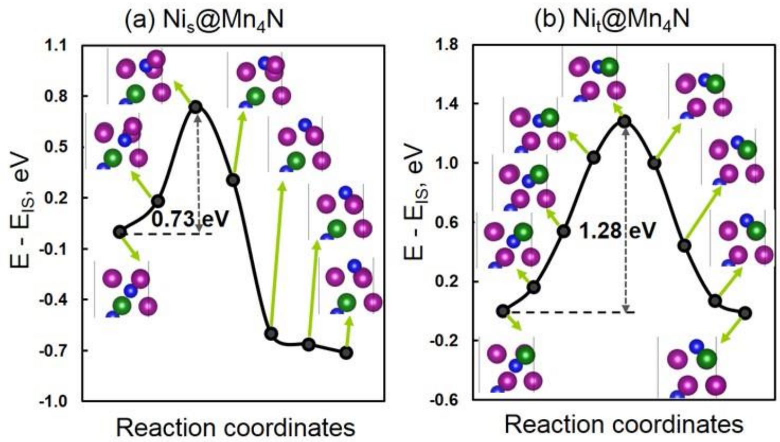

Figure 5.9 Potential energy surfaces for diffusions of N(s) from sublayer to surface. (a) Ni_s@Mn_4N, and (b) Ni_t@Mn_4N. The total energy of the initial state (E_{IS}) is chosen as the energy reference. The snapshot image corresponding to each intermediate state is shown. Magenta, green, and blue colors represent Mn, Ni, and N, respectively. Adapted with permission from Ref [9]. Copyright 2018, American Chemical Society.

Free energies for the hydrogen reduction of Mn_4N doped with Ni at its top-layer (Ni_t@Mn_4N) are shown in Figure 5.8 (black). Pure Mn_4N (blue dashed lines) and Fe_t@Mn_4N (red dashed lines) were included as references. Comparisons of free energies between pure Mn_4N, sublayer Ni doping (Ni_s@Mn_4N) and Ni_t@Mn_4N are shown in Figure B.1 in Appendix B. On Ni_t@Mn_4N, hydrogen dissociative adsorption (R11) is almost thermal neutral (-0.001 eV at 700 °C and 1 bar), where the dissociated H* adsorbs at the 3-fold site next to the Ni dopant (the 2nd top panel of Figure 5.8), reflecting the direct involvement of doped top-layer Ni atom. The R11 step has become approximately 0.3 eV lower in free energy than both Mn_4N and Fe_t@Mn_4N. The adsorption patterns for NH_x* (x = 1–3) resemble those on both Mn_4N and Fe_t@Mn_4N. Therefore, the trends for R12–R14 steps are similar as expected. The stronger Ni–H bonding substantially reduces the overall free energies for the first NH_3 production. In the second reduction cycle, although the free energy of the R11 step shifts upward to 0.16 eV (as H binding becomes weaker) when compared to Mn_4N (0.02 eV), the overall free energy for the second NH_3 formation remains more favorable than Mn_4N. As shown in Figure 5.8, the overall free energy (forming two molecules of NH_3) is 1.55 eV lower than on Mn_4N, and 0.57 eV lower than on Fe_t@Mn_4N.

Regarding N diffusion, the same principle can be applied to understand $N_{(s)}$ diffusion energy barrier in Step R16 for Ni-doped Mn_4N. As shown in Figure 5.9(a), compared to pure Mn_4N, $E_{a\,vac}$ is lowered from 1.12 eV to 0.73 eV on Ni_s@Mn_4N, suggesting that, like the Fe dopant in the Mn_4N sublayer, the sublayer Ni also facilitates $N_{(s)}$ diffusion onto the top layer, because of the weaker Ni-N bond than the Mn-N bond. Similarly, the surface Mn atom is found distorted from its normal lattice position (Figure 5.9(a)). On Ni_t@Mn_4N, the $E_{a\,vac}$ has increased to 1.28 eV from 1.12 eV. This is due to the fact that $N_{(s)}$ needs to break the stronger Mn-N bond than Ni-N bond in Ni_t@Mn_4N.

In order to reveal potential trends and predict the behavior of Mn_4N doped with Fe and Ni, a correlation between the reaction energy of N diffusion ($E_{r\,vac}$) and diffusion barrier ($E_{a\,vac}$) can be represented within the formulation of the well-established Brønsted–Evans–Polanyi (BEP) relationship, as shown in Figure 5.10(a). The slope and intersection are 0.96 (dimensionless) and 1.34 eV, respectively. As aforementioned, by referencing to pure Mn_4N, lower N diffusion barriers can be expected if weaker bonds (e.g., Fe-N and Ni-N bonds) need to be broken during N diffusion. On the other hand, Cr-N bond is much stronger than the Mn-N bond [13]. As a result, a decreased N diffusion barrier was observed for Cr_t@Mn_4N instead, since the weaker Mn-N bond broke for the sublayer N to diffuse onto the surface. In addition, for Cr_s@Mn_4N, the stronger Cr-N bond has to break, thus resulting in high barrier.

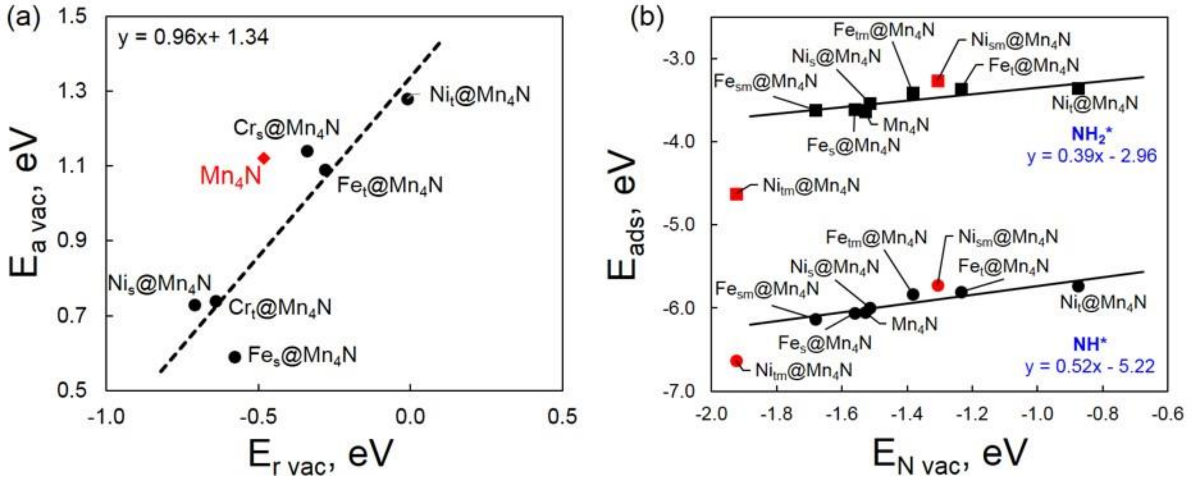

Figure 5.10 (a) Brønsted–Evans–Polanyi (BEP) relationship for N diffusion, where $E_{r\ vac}$ is the reaction energy of N diffusion based on Equation (1). Pure Mn_4N is shown in red diamond. (b) Scaling relationships (black) between N binding energies ($E_{N\ vac}$) and adsorption energies of NH* (circle) and NH_2* (square). Ni_{sm}@Mn_4N and Ni_{tm}@Mn_4N are included as outliners (in red) that do not follow the linear scaling. Adapted with permission from Ref [9]. Copyright 2018, American Chemical Society.

Finally, linear scaling relationships between $E_{N\ vac}$ and E_{ads} for NH_x* (x =1, 2) on pure and various doped Mn_4N, calculated according to Equations (47-48), were shown in Figure 5.10(b), where data from calculations on Fe_s@Mn_4N, Fe_t@Mn_4N, Ni_s@Mn_4N, and Ni_t@Mn_4N were employed. Moreover, in order to test the limits of these scaling relationships for doped Mn_4N systems, sub- and top-monolayer configurations composed of Fe, denoted as Fe_{sm}@Mn_4N and Fe_{tm}@Mn_4N, were included (see Figure B.2). With Mn_4N as the host material, linear correlations indeed exist between the two sets of quantities associated with NH* and NH_2*. Slopes of the two linear scaling relationships from fitting are 0.52 and 0.39 for NH* and NH_2* (standard error being 0.07 eV), respectively, close to the previous finding [32]. The slopes are also within reasonable agreement with theoretical slopes, i.e., 0.67 and 0.33 for respective NH* and NH_2* based on (n_{max} – x)/n_{max}, where n_{max} = 3, established on transition metals [33].

However, unlike metals, chemical properties of nitrides (e.g., Mn_4N) will be susceptible to the existence of sublayer N vacancies, which are likely to complicate the trends for reaction energetics prediction. As shown in Figure B.3, linear scaling relationships on Mn_4N and Fe- and Ni-doped Mn_4N surfaces with one sublayer N vacancy show varying slopes and intercepts for NH_x (x = 1, 2). It is also interesting to note large deviations on Ni_{sm}@Mn_4N and Ni_{tm}@Mn_4N surfaces in Figure 5.10(b) (denoted with red symbols). This observation suggests that linear scaling relationships can be broken for certain configurations, possibly for mixed alloy nitrides as well. Nevertheless, these exceptions could offer exciting opportunities to design new nitride materials for NH_3 production.

5.4 Conclusions

Step-catalysis with metal nitride as the nitrogen source is regarded as a sustainable avenue for ammonia production. While manganese nitrides are regarded promising for ammonia synthesis, theoretical insights become even more necessary by providing the mechanism to guide the discovery and design of novel materials. In this chapter, Mn_4N has been studied with DFT calculations to improve NH_3 production. The mechanism, describing hydrogen dissociative adsorption, lattice N diffusion, and ammonia formation, has been shown in details. Thermodynamic analysis showed that the binding of atomic H and lattice N diffusion energy barrier are critical for the performance of manganese nitrides. Fe- and Ni-doped in the sublayer of Mn_4N are revealed to facilitate N diffusion, whereas both the sublayer and top layer Ni dopants are able to lower the overall endergonicity as a result of hydrogen reduction. Furthermore, the energetic and kinetic behaviors of various configurations of doped Mn_4N have been summarized in terms of the BEP and linear scaling relationships, setting up the groundwork for future studies.

5.5 Acknowledgements

This study was supported financially by the U.S. Department of Energy, Office of Science, Office of DOE EPSCoR, under Award Number(s) DOE EPSCoR DE-FOA-0001572. Theoretical calculations were carried out thanks to the supercomputing resources and services from the Centre for Nanoscale Materials (CNM) supported by the Office of Science of the US Department of Energy under the contract No. DE-AC02-06CH11357, the Beocat Research Cluster at Kansas State University, which is funded in part by NSF grants CNS-1006860 and the National Energy Research Scientific Computing Centre (NERSC) under the contract No. DEAC02-05CH11231.

Bibliography

[1]. Smil, V., Detonator of the Population Explosion. *Nature* **1999,** 400, (6743), 415-415.

[2]. Erisman, J. W.; Sutton, M. A.; Galloway, J.; Klimont, Z.; Winiwarter, W., How A Century of Ammonia Synthesis Changed the World. *Nature Geosci* **2008,** 1, (10), 636-639.

[3]. Amar, I. A.; Lan, R.; Petit, C. T. G.; Tao, S., Solid-state Electrochemical Synthesis of Ammonia: A Review. *Journal of Solid State Electrochemistry* **2011,** 15, (9), 1845-1860.

[4]. Licht, S.; Cui, B. C.; Wang, B. H.; Li, F. F.; Lau, J.; Liu, S. Z., Ammonia Synthesis by N_2 and Steam Electrolysis in Molten Hydroxide Suspensions of Nanoscale Fe_2O_3. *Science* **2014,** 345, (6197), 637-640.

[5]. Schrauzer, G. N.; Guth, T. D., Photocatalytic Reactions. 1. Photolysis of Water and Photoreduction of Nitrogen on Titanium Dioxide. *Journal of the American Chemical Society* **1977,** 99, (22), 7189-7193.

[6]. Galvez, M. E.; Halmann, M.; Steinfeld, A., Ammonia Production via A Two-step Al_2O_3/AlN Thermochemical Cycle. 1. Thermodynamic, Environmental, and Economic Analyses. *Industrial and Engineering Chemistry Research* **2007,** 46, (7), 2042-2046.

[7]. Gálvez, M. E.; Frei, A.; Halmann, M.; Steinfeld, A., Ammonia Production via a Two-Step Al_2O_3/AlN Thermochemical Cycle. 2. Kinetic Analysis. *Industrial and Engineering Chemistry Research* **2007,** 46, (7), 2047-2053.

[8]. Gálvez, M. E.; Hischier, I.; Frei, A.; Steinfeld, A., Ammonia Production via a Two-Step Al_2O_3/AlN Thermochemical Cycle. 3. Influence of the Carbon Reducing Agent and Cyclability. *Industrial and Engineering Chemistry Research* **2008,** 47, (7), 2231-2237.

[9]. Shan, N.; Chikan, V.; Pfromm, P.; Liu, B., Fe and Ni Dopants Facilitating Ammonia Synthesis on Mn4N and Mechanistic Insights from First-Principles Methods. *The Journal of Physical Chemistry C* **2018,** 122, (11), 6109-6116.
[10]. Michalsky, R.; Pfromm, P. H., Thermodynamics of metal reactants for ammonia synthesis from steam, nitrogen and biomass at atmospheric pressure. *AIChE Journal* **2012,** 58, (10), 3203-3213.
[11]. Michalsky, R.; Parman, B. J.; Amanor-Boadu, V.; Pfromm, P. H., Solar thermochemical production of ammonia from water, air and sunlight: Thermodynamic and economic analyses. *Energy* **2012,** 42, (1), 251-260.
[12]. Michalsky, R.; Pfromm, P. H., An Ionicity Rationale to Design Solid Phase Metal Nitride Reactants for Solar Ammonia Production. *The Journal of Physical Chemistry C* **2012,** 116, (44), 23243-23251.
[13]. Michalsky, R.; Avram, A. M.; Peterson, B. A.; Pfromm, P. H.; Peterson, A. A., Chemical looping of metal nitride catalysts: low-pressure ammonia synthesis for energy storage. *Chemical Science* **2015,** 6, (7), 3965-3974.
[14]. Michalsky, R.; Pfromm, P. H.; Steinfeld, A., Rational Design of Metal Nitride Redox Materials for Solar-driven Ammonia Synthesis. *Interface Focus* **2015,** 5, (3), 20140084.
[15]. Abghoui, Y.; Garden, A. L.; Howalt, J. G.; Vegge, T.; Skúlason, E., Electroreduction of N_2 to Ammonia at Ambient Conditions on Mononitrides of Zr, Nb, Cr, and V: A DFT Guide for Experiments. *ACS Catalysis* **2016,** 6, (2), 635-646.
[16]. Abghoui, Y.; Skúlason, E., Computational Predictions of Catalytic Activity of Zincblende (110) Surfaces of Metal Nitrides for Electrochemical Ammonia Synthesis. *The Journal of Physical Chemistry C* **2017,** 121, (11), 6141-6151.
[17]. Abghoui, Y.; Skúlason, E., Onset Potentials for Different Reaction Mechanisms of Nitrogen Activation to Ammonia on Transition Metal Nitride Electro-catalysts. *Catalysis Today* **2017,** 286, (Supplement C), 69-77.
[18]. Abghoui, Y.; Skúlason, E., Electrochemical Synthesis of Ammonia via Mars-van Krevelen Mechanism on the (111) Facets of Group III–VII Transition Metal Mononitrides. *Catalysis Today* **2017,** 286, (Supplement C), 78-84.
[19]. Fruchart, D.; Givord, D.; Convert, P.; l'Heritier, P.; Senateur, J. P., The Non-collinear Component in the Magnetic Structure of Mn_4N. *Journal of Physics F: Metal Physics* **1979,** 9, (12), 2431.
[20]. Feng, W. J.; Sun, N. K.; Du, J.; Zhang, Q.; Liu, X. G.; Deng, Y. F.; Zhang, Z. D., Structural Evolution and Magnetic Properties of Mn–N Compounds. *Solid State Communications* **2008,** 148, (5), 199-202.
[21]. Kresse, G.; Hafner, J., Ab initio Molecular Dynamics for Open Shell Transitio Metals. *Physical Review B* **1993,** 48, (17), 13115-13118.
[22]. Kresse, G.; Furthmuller, J., Efficiency of *Ab initio* Total Energy Calculations for Metals and Semiconductors using A Plane-wave Basis Set. *Computational Materials Science* **1996,** 6, (1), 15-50.
[23]. Perdew, J. P.; Burke, K.; Ernzerhof, M., Generalized Gradient Approximation Made Simple. *Physical Review Letters* **1996,** 77, (18), 3865-3868.
[24]. Blochl, P. E., Projector Augmented Wave Method *Physical Review B* **1994,** 50, (24), 17953-17979.
[25]. Takei, W. J.; Heikes, R. R.; Shirane, G., Magnetic Structure of Mn_4N-Type Compounds. *Physical Review* **1962,** 125, (6), 1893-1897.

[26]. Monkhorst, H. J.; Pack, J. D., Special Points for Brillouin Zone Integrations. *Physical Review B* **1976,** 13, (12), 5188-5192.

[27]. Henkelman, G.; Uberuaga, B. P.; Jonsson, H., A climbing image nudged elastic band method for finding saddle points and minimum energy paths. *Journal of Chemical Physics* **2000,** 113, (22), 9901-9904.

[28]. Henkelman, G.; Jónsson, H., A Dimer Method for Finding Saddle Points on High Dimensional Potential Surfaces using Only First Derivatives. *The Journal of Chemical Physics* **1999,** 111, (15), 7010-7022.

[29]. Le, T. N.-M.; Liu, B.; Huynh, L. K., SurfKin: An Ab initio Kinetic Code for Modeling Surface Reactions. *Journal of Computational Chemistry* **2014,** 35, (26), 1890-1899.

[30]. Shan, N.; Zhou, M.; Hanchett, M. K.; Chen, J.; Liu, B., Practical Principles of Density Functional Theory for Catalytic Reaction Simulations on Metal Surfaces – from Theory to Applications. *Molecular Simulation* **2017,** 43, (10-11), 861-885.

[31]. Mars, P.; van Krevelen, D. W., Oxidations Carried Out by Means of Vanadium Oxide Catalysts. *Chemical Engineering Science* **1954,** 3, (Supplement 1), 41-59.

[32]. Fernández, E. M.; Moses, P. G.; Toftelund, A.; Hansen, H. A.; Martínez, J. I.; Abild-Pedersen, F.; Kleis, J.; Hinnemann, B.; Rossmeisl, J.; Bligaard, T.; Nørskov, J. K., Scaling Relationships for Adsorption Energies on Transition Metal Oxide, Sulfide, and Nitride Surfaces. *Angewandte Chemie International Edition* **2008,** 47, (25), 4683-4686.

[33]. Abild-Pedersen, F.; Greeley, J.; Studt, F.; Rossmeisl, J.; Munter, T. R.; Moses, P. G.; Skulason, E.; Bligaard, T.; Nørskov, J. K., Scaling properties of adsorption energies for hydrogen-containing molecules on transition-metal surfaces. *Physical Review Letters* **2007,** 99, (1), 016105-016101.

Chapter 6 - Screening of Mn Nitride Alloys for Enhanced NH_3 Formation

6.1 Introduction

Metal (e.g., Ti, Ca, Al, Ce, Mo) nitrides were considered by Mittasch and Frankenburg for ammonia production originally decades ago in heterogeneous Haber-Bosch processes [1]. Recently, the scope of transition metal nitrides for ammonia productions has been extended in usage involved in electrochemical or other ammonia synthesis routes as well [2-17]. Mn stands out due to its relative favorable thermodynamics and kinetics to form stable nitride [5, 18]. However, the strong Mn-N bonding (∼-1.8 eV on Mn(211)) can still slow down ammonia formation and remains a challenge for the extraction of lattice N [18]. Experimental evidences indicated that typically 3.1−8 mol% lattice N in Mn nitrides has been converted into NH_3 at 400−700 °C 1 atm pressure [5, 19].

Efforts have been made to modify Mn nitrides in order to improve NH_3 synthesis activity. Michalsky and co-workers pointed out that formation energy of lattice N vacancy can be used as a descriptor because it reflects how easily lattice nitrogen can be extracted [6]. $Mn_2N(0001)$ has been doped with other transition metals and suggested that Fe-doped $Mn_2N(0001)$ boosted NH_3 production by destabilizing lattice N [5]. In Chapter 5, theoretical modeling has suggested that Mn_4N with sublayer Fe or Ni dopant can indeed weaken Mn-N bonding and facilitate lattice N diffusion [10]. In this chapter, systematic investigation will be carried out to generate a broad understanding on how modifications of Mn nitride configurations will impact ammonia formation. The goal is to provide the necessary theoretical guidance for future experimental synthesis.

In Chapter 5, we found that, even for Fe- or Ni-doped Mn_4N, ammonia production still remains too endergonic. The binding energies of NH_x (x = 0, 1, 2) were used as the descriptors to screen for the optimal catalytic behavior. The formed NH is a stable intermediate, once formed, it prefers to remain on the active site rather than proceeding to form NH_2, and NH_3. Therefore, we recognize that NH binding needs to be further weakened, without sacrificing the thermodynamic favorability for NH_2 and NH_3 formations.

It has been found that the binding energies of NH_x (x = 0, 1, 2) species followed linear scaling relationships on certain metal nitrides (e.g., TiN, W_2N and Mo_2N) [20]. Recently, the linear relationships of NH and NH_2 bindings with respect to N binding were also developed for Mn_4N and doped Mn_4N [10]. This trend suggests that any effort to weaken NH binding would likely weaken NH_2 and NH_3 binding as well. Therefore, the intrinsic linear scaling relationship needs to be *broken*.

Several candidates that are likely to break the linear scaling trend have been identified [10]. For example, the NH binding on Ni_{tm}@Mn_4N shifts toward the opposite direction and becomes stronger than that on Mn_4N. In this chapter, we consider a broader range of configurations derived from both Mn_4N and Mn_2N nitride phases. Periodic DFT calculations were performed to generate a comprehensive understanding of the behaviors of N, NH, NH_2, and NH_3 bindings on these models. The Mars-van Krevelen and Eley-Rideal mechanisms have been proposed to aid the evaluation of the reactivity on the proposed surface models for ammonia formation. Specifically, single heteroatom doping and alloying based on the two phases of Mn nitrides, Mn_4N and Mn_2N, were included in the current study. The scaling relationship can then be used as a guidance to assist the search for the optimal configuration.

6.2 Computational Details

Periodic DFT calculations were performed with the Vienna Ab initio Simulation Package (VASP) [21, 22]. The electron-electron exchange-correlation energies were determined within the generalized gradient approximation (GGA) employing the Perdew–Burke–Ernzerhof (PBE) functional [23]. The projector augmented-wave (PAW) method [24] was used to treat the core electrons of elements. Geometry optimizations were converged until the force on each atom was less than 0.02 eV/Å, while convergence criterion for self-consistent iterations were set up to 1×10^{-6} eV. A 400 eV plane-wave cut-off was used. Dipole corrections and spin-polarization were also included in all slab calculations.

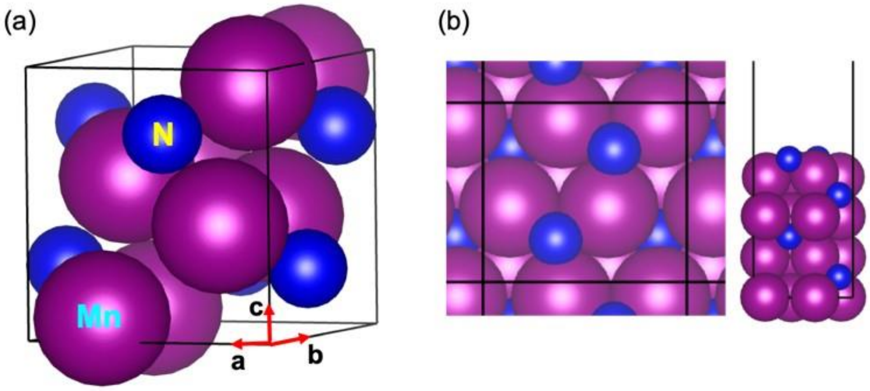

Figure 6.1 (a) Optimized structure of Mn_2N bulk, (b) top and side views of $Mn_2N(200)$. Mn, and N atoms are in magenta and blue, respectively. Black lines represent the periodic boundaries.

The structures of different Mn nitride phases have been investigated experimentally [25, 26] and theoretically [27]. Mn_4N, an ε-phase of manganese nitride, was studied in Chapter 5 [10]. In this chapter, the ζ-phase (represented stoichiometrically as Mn_2N) [25] at higher N content, is included. The lattice constants of Mn_2N bulk were converged to 4.47 (along the a-axis), 5.46 (b-axis) and 4.82 (c-axis) Å, as shown in Figure 6.1(a). The magnetic moment of each Mn atom, which is equivalent in the lattice, is 2.0 μ_B. The calculated values are in good agreement with those reported in the literature, i.e., 4.54 Å, 5.67 Å, 4.91 Å and 1.6 μ_B, respectively [28]. A four-layer, (1 × 1) $Mn_2N(200)$ slab (Figure 6.1(b)) was employed, with the top two layers allowed to relax. The Brillouin-zone was sampled using a 4 × 4 × 1 k-point mesh based on the Monkhorst-Pack scheme.

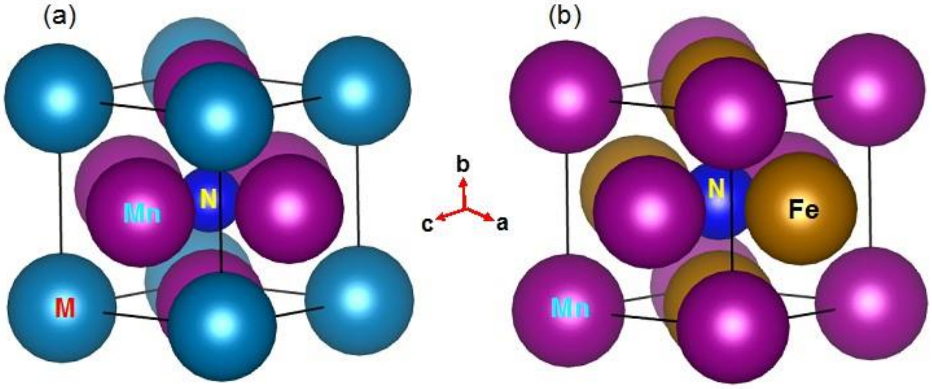

Figure 6.2 Bulk structures of (a) Mn_3NM alloy and (b) Mn_2NFe_2 alloy. Mn, N, M, and Fe are in magenta, blue, dark azure, and gold, respectively. Black lines represent the periodic boundaries.

Binary Mn_3NM and Mn_2NM_2 alloyed nitrides (M represents the secondary metal) were considered in current work. Specifically, Mn_3NNi and Mn_3NGa alloys have been synthesized and reported in the literature [29, 30]. However, no experimental reports on Mn_3NFe and Mn_2NFe_2 have been found. In this work, Mn_3NFe was assumed to inherit from the face-centered cubic (FCC) bulk structures of Mn_3NNi (or Mn_3NGa) with a = b = c, which is shown in Figure 6.2(a). Mn_2NFe_2 was built by substituting two Mn atoms in Mn_4N bulk and the most stable structure is shown in Figure 6.2(b). The lattice constants were converged to 3.83, 3.78, and 3.85 Å for cubic Mn_3NNi,

Mn_3NGa, and Mn_3NFe lattices, respectively, which are in good agreement with experimental measurements (see Table 6.1) [29, 30]. For Mn_2NFe_2, the lattice constants were computed as 3.77 Å in ‘a’ and ‘b’ axis and 3.79 Å for ‘c’ axis.

Table 6.1 Lattice constants (in Å) of Mn_3NM (M = Ni, Ga and Fe) and Mn_2NFe_2.

System	Experimental values (Å)	DFT calculations (Å, this work)
Mn_3NNi	3.89 (a = b = c) [29]	3.83 (a = b = c)
Mn_3NGa	3.90 (a = b = c) [30]	3.78 (a = b = c)
Mn_3NFe		3.85 (a = b = c)
Mn_2NFe_2		a = b = 3.77, c = 3.79

Dopant metals (Ni or Fe, in sky blue) in the top-layer of $Mn_2N(200)$ are depicted in Figure 6.3(a). Four-layer (111) slabs were obtained by cutting Mn_3NNi and Mn_2NFe_2 bulk. The top and side views of $Mn_3NNi(111)$ and $Mn_2NFe_2(111)$ are displayed in Figure 6.3(b-c).

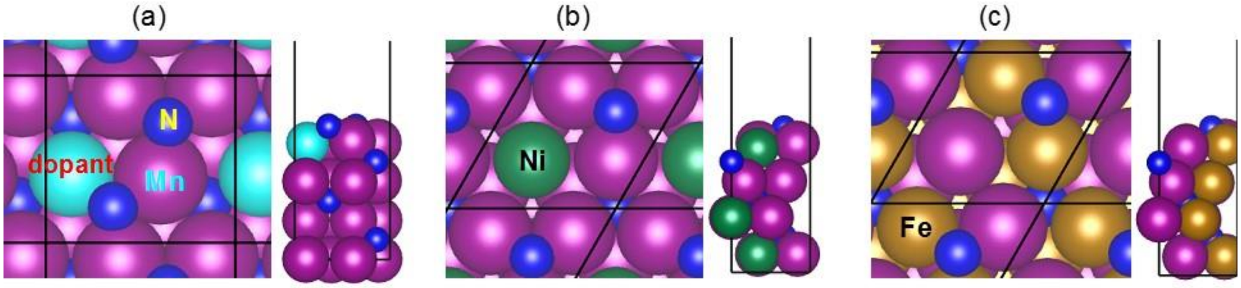

Figure 6.3 Top and side views of (a) doped $Mn_2N(200)$ in the top-layer, (b) $Mn_3NNi(111)$, and (c) $Mn_2NFe_2(111)$. Mn, N, dopant, Ni and Fe are in magenta, blue, turquoise, green, and gold, respectively. Black lines represent the periodic boundaries of the (1x1) unit cell.

It is critical that sublayer lattice N can be utilized efficiently. Therefore, sublayer N diffusion will also be an important factor to consider in this study. The diffusion energy barriers will be calculated using the Climbing image nudged elastic band (CI-NEB) [31] and dimer methods [32]. A 5-layer slab was used for transition state search, with the top three layers allowed to relax.

Binding energies (BEs) of N, NH, and NH_2 are defined by Equations (49-50)

$$BE_A = E_{A^*} - E_{*(v)_t} - E_{A(g)} \tag{49}$$

$$BE_N = E_{N^*} - E_{*(v)_t} - \frac{1}{2}E_{N_2(g)} \tag{50}$$

where E_{A^*}, $E_{*(v)_t}$, and $E_{A(g)}$ represent the total energies of adsorbate A, clean surface, and gaseous A in vacuum, respectively. For atomic N binding, the total energy of $E_{N_2(g)}$ was used instead, as shown in Equation (50).

The free energy change (ΔG) associated with each elementary step in ammonia formation includes zero-point energy (ΔZPE) correction, and the entropy change ($T\Delta S$). The entropies is then obtained using standard statistical mechanical approach [33, 34]. Translational and rotational entropy terms were included for gas phase species. Vibrational frequencies were calculated based on simple harmonic approximations.

6.3 Scaling Relationships for NH and NH_2 Binding

In Chapter 5, we showed that, in order to boost NH_3 production, NH_2 and NH_3 adsorptions have to be strengthened without too strong NH adsorptions. In this spirit, a broader range of configurations including sublayer and top-layer doping Mn_4N and Mn_2N, Mn_3NM alloys and Mn_2NFe_2 were considered in addition to the systems reported previously [10]. The mathematical formulas of these scaling relationships are represented by Equations (51-52). The calculated data of new added configurations were used for validations of existed scaling relationships without new fitting (Figure 6.5(a)).

$$BE_{NH} = 0.52 \times BE_N - 5.22 \tag{51}$$

$$BE_{NH_2} = 0.39 \times BE_N - 2.96 \tag{52}$$

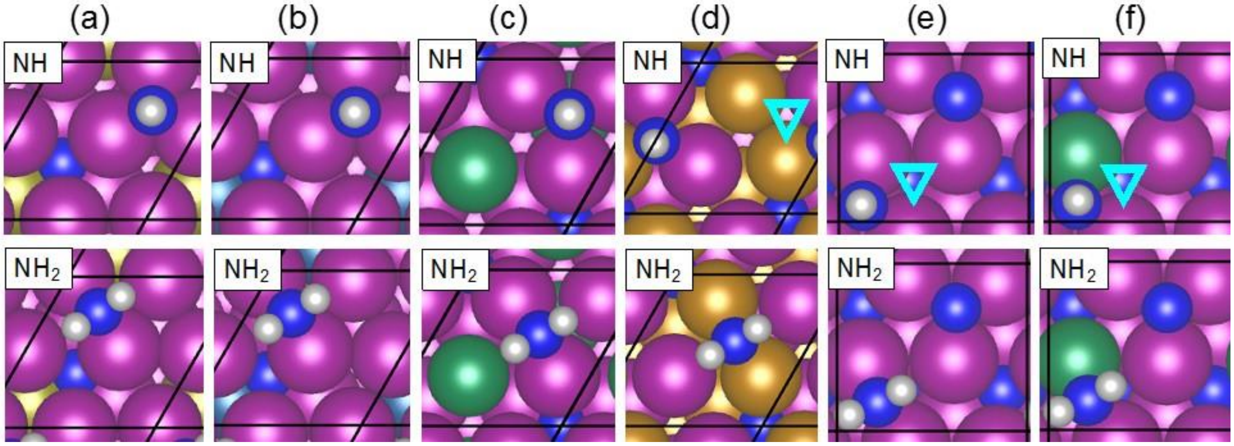

Figure 6.4 Adsorptions of NH (top panels) and NH_2 (bottom panels) on (a) $Mo_s@Mn_4N$, (b) $Co_s@Mn_4N$, (c) Mn_3NNi, (d) Mn_2NFe_2, (e) Mn_2N, and (f) $Ni_t@Mn_2N$. Mn, N, Mo, Co, Ni and Fe are in magenta, blue, olive, dark cerulean, green and gold, respectively. Black lines represent the periodic boundaries of the (1x1) unit cell. Surface lattice N vacancies in (d-f) are indicated in sky blue downward triangle, and it was hidden at the underneath of adsorbate in (a-c).

It is desirable that NH_2 binding could be improved without further strengthening NH binding at the same time. Thus the correlation between binding energies of NH and NH_2 were recognized in Figure 6.5(b) based on the data coming from Ref [10]. The slope and intersection are 0.79 (dimensionless) and 1.17 eV, respectively (see Equation (53)). The coefficient of determination, R^2, is 0.95, indicating a great fitting between NH and NH_2 bindings on Mn_4N and Fe- and Ni-doped Mn_4N.

$$BE_{NH_2} = 0.79 \times BE_{NH} + 1.17 \tag{53}$$

The geometries of NH adsorptions on Mn_4N doped with other metal species (Mo and Co) also resemble to those over Mn_4N, where NH occupies the 3-fold site. NH adsorptions on $Mo_s@Mn_4N$ and $Co_s@Mn_4N$ are illustrated in the top panels of Figure 6.4(a-b). NH_2 binds on the bridge site between the two Mn atoms on $Mo_s@Mn_4N$ and $Co_s@Mn_4N$ (bottom panels of Figure 6.4(a-b)). On Mn_3NNi, NH prefers the 3-fold site and NH_2 prefers the bridge site as well, as shown in Figure 6.4(c). However, as shown in the bottom panels of Figure 6.4(d), the bridge site between the two Fe atoms is more favorable for NH_2 binding on Mn_2NFe_2. The most stable site for NH binding on Mn_2NFe_2, Mn_2N, and $Ni_t@Mn_2N$ is one of the 3-fold sites on the surface instead of the surface lattice N vacancy site (downward sky blue triangle). On $Mn_2N(200)$, NH_2 binds on the bridge site near the surface lattice N vacancy (bottom panel of Figure 6.4(e)). With the Ni atom doped on the surface of Mn_2N ($Ni_t@Mn_2N$), NH_2 will prefer to bind at the Mn-Ni bridge site.

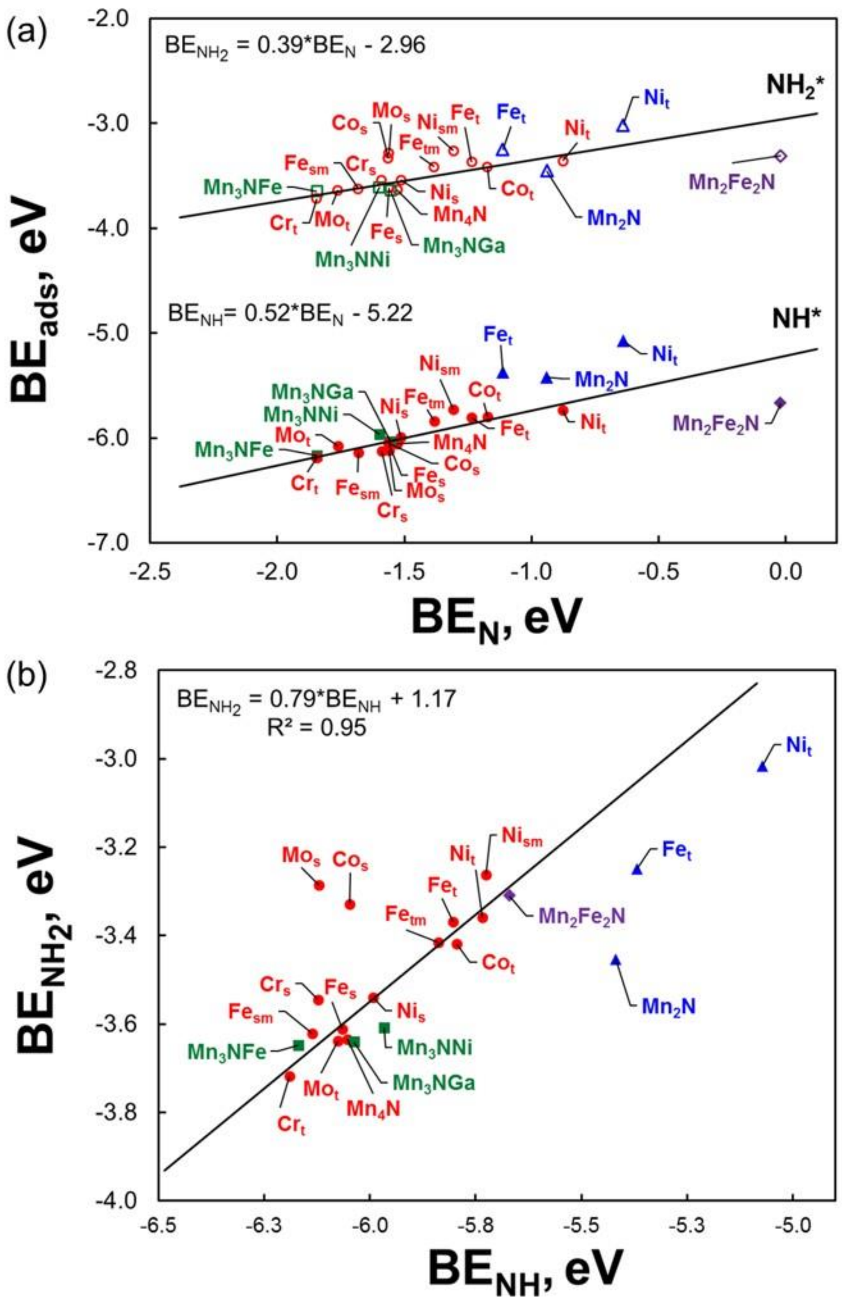

Figure 6.5 (a) Scaling relationships between N* and NH* (solid symbols), NH_2* (open symbols) binding energies on Mn_4N (red circles), Mn_2N (blue triangles), Mn_3NM (M = Ni, Fe and Ga, green squares), and Mn_2Fe_2N (purple diamond). (b) Correlation between the binding energies of NH* and NH_2*. Subscripts 't', 's' and 'sm' denote top layer, sublayer doping, and sub-monolayer, respectively.

As discussed in Chapter 5, the linear scaling between NH and NH_2 will have to be broken so that simultaneous strengthening of NH_2 binding and weakening of NH species becomes possible. In this study, we define the deviation as $\left|BE - BE_{fitted}\right|$, where BE is obtained from DFT calculation and BE_{fitted} from the estimation based on linear scaling relationship. Further, we consider the deviation as significant if its value is larger than the standard error.

For NH adsorption, the standard error is 0.07 eV. A few new configurations have been identified: Cr_s@Mn_4N, Mo_s@Mn_4N, Mn_3NNi, Mn_2NFe_2, Mn_2N, Fe_t@Mn_2N, and Ni_t@Mn_2N. For NH_2 bindings, the standard error is also 0.07 eV. Hence, configurations of Mo_s@Mn_4N, Co_s@Mn_4N, Mn_2N, Fe_t@Mn_2N, Ni_t@Mn_2N and Mn_2NFe_2 in Figure 6.5(a) are identified. Furthermore, only Mn_2N and Mn_2NFe_2 satisfy the criterion of strengthen NH_2 adsorptions.

A linear correlation based on the binding energies of NH and NH_2 on Mn_4N and Fe-/Ni-doped Mn_4N is shown Figure 6.5(b), with a standard error of 0.03 eV. It can be seen that large deviations can be observed for Mo_s@Mn_4N, Co_s@Mn_4N, Cr_s@Mn_4N, Mn_3NNi, Mn_3NGa, Mn_3NFe, Mn_2N, Fe_t@Mn_2N and Ni_t@Mn_2N. Among these configurations, Mn_3NNi, Mn_3NGa, Mn_2N, Fe_t@Mn_2N and Ni_t@Mn_2N strengthen the NH_2 adsorptions as they are below the correlation line, and thus, will fit our screening criteria.

Therefore, Mn_3NNi, Mn_2NFe_2, Mn_2N, and Ni_t@Mn_2N are selected for further evaluation of their performance for ammonia formation in next section as they exhibited either the ability to enhance NH_2 or weaken NH bindings.

6.4 Evaluations of Selected Nitride Models for NH_3 Production

6.4.1 NH_3 Formation Mechanisms Reduction of Nitrides Reduction by H_2

In Chapter 5, the Mars-van Krevelen mechanism was used to describe NH_3 formation on Mn_4N. The elementary reaction steps for the first NH_3 molecule are shown below in Equations (R17-R23), where ‘g’, ‘$(v)_t$’ and ‘$(v)_s$’ represent the gas phase, N vacancy site on top and sublayer, respectively. In the Mars-van Krevelan mechanism, we let molecular H_2 to undergo dissociative adsorption according to Equation (R17) before H atom is added to the surface N species.

$$\frac{1}{2}H_{2(g)} + * \rightarrow H^* \tag{R17}$$

$$H^* + N_{(t)} \rightarrow NH^*(v)_t \tag{R18}$$

$$\frac{1}{2}H_{2(g)} + *(v)_t \rightarrow H^*(v)_t \tag{R19}$$

$$NH^*(v)_t + H^*(v)_t \rightarrow NH_2^*(v)_t + *(v)_t \tag{R20}$$

$$NH_2^*(v)_t + H^*(v)_t \rightarrow NH_3^*(v)_t + *(v)_t \tag{R21}$$

$$NH_3^*(v)_t \rightarrow NH_{3(g)} + *(v)_t \tag{R22}$$

$$N_{(s)} + *(v)_t \rightarrow N_{(t)} + *(v)_s \tag{R23}$$

In addition, we also considered the Eley-Rideal mechanism, in which the gaseous H_2 directly reacts with lattice N to form NH, NH_2 and NH_3 instead, as represented by Equations (R24-R26), which has been reported by Zeinalipour-Yazdi for ammonia formation [16]. NH_3 desorption and lattice N diffusion, as in Equations (R22-R23), are also included as well.

$$N_{(t)} + \frac{1}{2}\mathrm{H}_{2(g)} \leftrightarrow NH^{*}(v)_t \tag{R24}$$

$$NH^{*}(v)_t + \frac{1}{2}\mathrm{H}_{2(g)} \leftrightarrow NH_2^{*}(v)_t \tag{R25}$$

$$NH_2^{*}(v)_t + \frac{1}{2}\mathrm{H}_{2(g)} \leftrightarrow NH_3^{*}(v)_t \tag{R26}$$

Recent experimental work by Pfromm and coworkers suggested that a traceable amount of NH_3 can be detected when pure Mn nitride is reduced under a hydrogen reduction environment at 500°C and 1 atm. Computationally, free energies for NH_3 formation following Mars-van Krevelan and Eley-Rideal mechanisms over $Mn_4N(111)$ were estimated under this condition using the method described earlier. The results are shown in Figure 6.6.

With Eley-Rideal mechanism (shown in solid pink in Figure 6.6), the overall NH_3 formation using the lattice N in Mn_4N is an endergonic process. As indicated in Figure 6.6, for production of the first NH_3 molecule, NH formation is exergonic (-0.21 eV). However, both NH_2 and NH_3 formations are endergonic (0.98 and 0.84 eV). The release of NH_3 from surface is exergonic with -0.45 eV. After the sublayer lattice N diffused to the surface, all the elementary steps are endergonic for the formation of the second NH_3 molecule. The only difference between Eley-Rideal and Mars-van Krevelen mechanisms is in the hydrogen dissociative adsorption steps. Although the hydrogen dissociative adsorption steps is exergonic (dashed blue lines in Figure 6.6), the strong H binding indicates that these atomic species will likely occupies the active sites instead of participating ammonia formation readily. Thus, the process following the Eley-Rideal pathway is more favorable for NH_3 production.

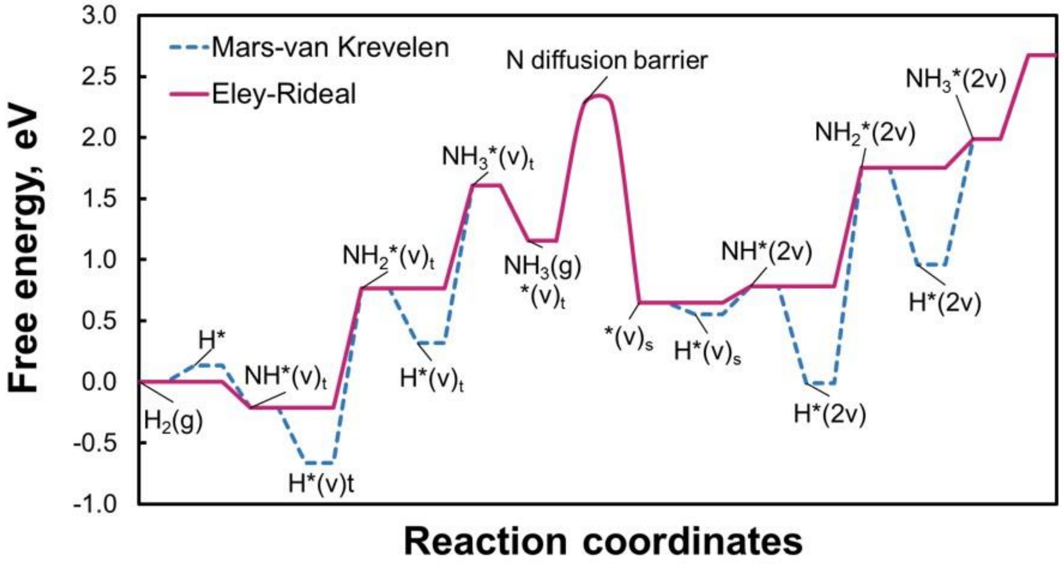

Figure 6.6 Free energy diagrams based on respective Mars-van Krevelen (dashed blue) and Eley-Rideal (solid pink) mechanism on Mn_4N for ammonia formation at 500 °C and 1 atm.

6.4.2 NH_3 Formation on Binary Alloyed Nitrides

Binary alloys such as Mn_3NNi and Mn_2NFe_2 were selected for the examinations of activity for ammonia production guided by the scaling relationships (Figure 6.5). Again, both Mars-van Krevelen and Eley-Rideal reaction mechanisms were employed for the evaluation.

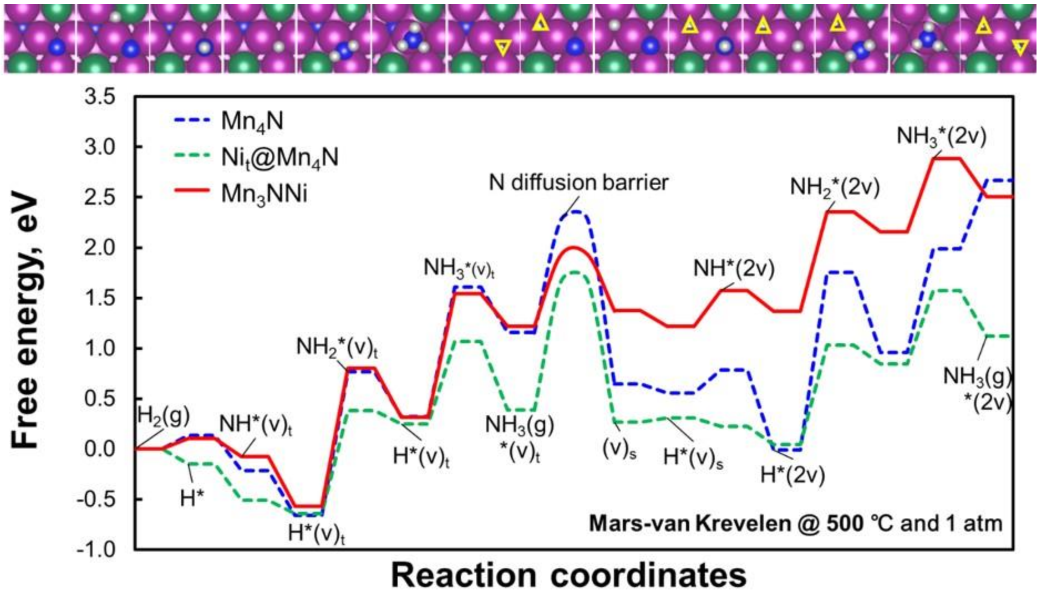

Figure 6.7 Free energy diagrams for the production of two NH_3 molecules on Mn_4N (dashed blue), $Ni_t@Mn_4N$ (dashed green) and Mn_3NNi (red) at 500 °C and 1 atm based on the Mars-van Krevelen mechanism. Optimized adsorbate structures on Mn_3NNi corresponding to each elementary step are shown in the top panel. The N vacancy site in the top-layer is indicated with a downward yellow triangle, while the N vacancy in the sublayer is indicated with an upward yellow triangle. Mn, Ni, N, and H are shown in magenta, green, blue and gray, respectively.

The free energies for NH_3 production via the Mars-van Krevelen mechanism over Mn_3NNi are depicted in red in Figure 6.7. Mn_4N, $Ni_t@Mn_4N$, and Mn_3NNi represent three system types (pure, doped, and alloyed) that are all derived from the FCC lattice with Ni as the secondary metal. The configurations corresponding to each elementary step are shown in the top panels. The H_2 dissociative adsorption (R17) on Mn_3NNi is only slightly more favorable thermodynamically than that on Mn_4N (by 0.04 eV), but much less favorable than on $Ni_t@Mn_4N$. Both formations of NH and NH_2 are less thermodynamically favorable than pure Mn_4N and $Ni_t@Mn_4N$. Slightly favored NH_3 formation were observed on Mn_3NNi comparing to pure Mn_4N, but not to $Ni_t@Mn_4N$. The adsorption of NH_3* on Mn_3NNi was slightly less favorable than that on Mn_4N (by 0.13 eV). The N diffusion barrier is lower in Mn_3NNi than in Mn_4N (by 0.41 eV) or $Ni_t@Mn_4N$ (by 0.57 eV). For the second NH_3 generation on Mn_3NNi, all NH, NH_2 and NH_3 formations are endergonic with the exergonic hydrogen dissociative adsorptions and NH_3 desorption, which results in Mn_3NNi becomes the least active for ammonia production among the three models, suggesting that too high Ni content (resulting in alloyed Mn-Ni nitride phase) will actually hinder ammonia formation.

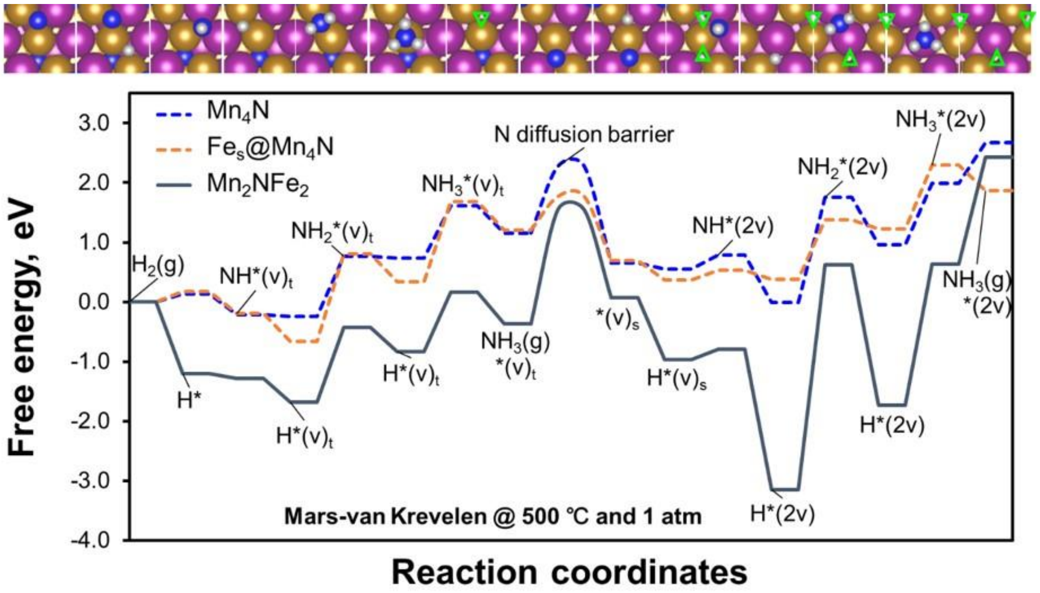

Figure 6.8 Free energy diagrams for the production of two NH_3 molecules via the Mars-van Krevelen mechanism on Mn_4N (dashed blue), $Fe_s@Mn_4N$ (dashed orange), and Mn_2NFe_2 (solid blue gray) at 500 °C and 1 atm. The optimized structures corresponding to each intermediate step on the close-packed surface of $Fe_s@Mn_4N$ (top panel) are shown. The N vacancy in the top-layer is represented with a downward green triangle, while the sublayer N vacancy is represented with an upward green triangle. Mn, Fe, N, and H are in magenta, gold, blue, and gray, respectively.

On Mn_2NFe_2, the adsorption configurations of N, NH, NH_2, and NH_3 are depicted in the top panel of Figure 6.8. As on Mn_4N, N, H, and NH all prefer the 3-fold site, while NH_2 binds on the bridge site between the two Fe atoms. NH_3 occupies the Fe top site on Mn_2NFe_2. When a nitrogen vacancy is present on the surface, NH_2 will prefer the bridge site between the two Mn atoms, while NH_3 binds on the Mn top site most preferably.

Free energies for NH_3 formation on Mn_2NFe_2 via the Mar-van Krevelen mechanism are summarized in Figure 6.8. Similarly, pure Mn_4N, $Fe_s@Mn_4N$ and Mn_2NFe_2 alloy were included in Figure 6.8 to get the insights into pure, doping and alloy systems. As shown in Figure 6.8, the overall thermodynamics for NH_3 production on Mn_2NFe_2 is more favorable than both Mn_4N and $Fe_s@Mn_4N$, indicating that higher Fe content presents advantageous activity for ammonia synthesis. The H_2 dissociative adsorption (R17) is very exothermic (-1.21 eV). The formation of NH (R18) is slightly exergonic (-0.08 eV). The formations of NH_2 and NH_3 become endergonic, similar to those on Mn_4N and $Fe_s@Mn_4N$. The lattice N in sublayer needs to overcome a barrier of 1.91 eV to diffuse onto the surface. Once a sublayer N lattice vacancy is generated, H adsorption becomes much stronger. The second NH_3 molecule formation is also endergonic, also with a very endothermic desorption energy 1.80 eV.

When ammonia formation is assumed to proceed via the Eley-Rideal mechanism on Mn_4N, $Ni_t@Mn_4N$, Mn_3NNi and Mn_2NFe_2, respective free energy diagrams are shown in Figure 6.9. On $Ni_t@Mn_4N$ (dashed green), the reactivity is shown to enhance NH_3 formation, as discussed in Chapter 5. On the Mn_3NNi alloy, however, similar reactivity enhancement is not observed (red in Figure 6.9). This is due to the endergonic lattice N diffusion and the successive endergonic NH_x ($x = 1, 2, 3$) formation steps in the second NH_3 production cycle. In this case, it can be understood that NH_3 production may not benefit from higher Ni-content. For Mn_2NFe_2, however, the reactivity for NH_3 production can be enhanced in the first reaction cycle (blue gray in Figure 6.9). However, this advantage on Mn_2NFe_2 diminishes during the second NH_3 molecule formation step due to high N diffusion barrier and high endothermicity of NH_3 release.

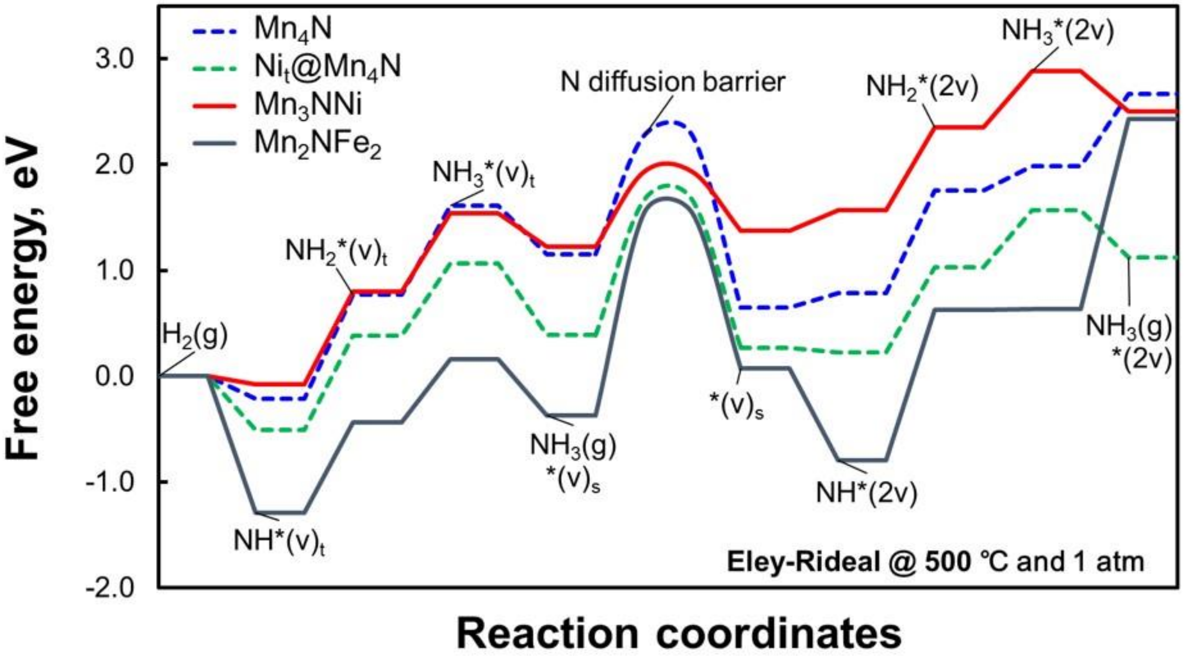

Figure 6.9 Free energy diagrams for two molecules of ammonia production via the Eley-Rideal mechanism on pure Mn_4N (dashed blue), $Ni_t@Mn_4N$ (dashed orange), Mn_3NNi (solid red) and Mn_2NFe_2 (solid blue gray) for NH_3 production 500 °C and 1 atm.

In this work, we proposed to exploit the scaling relationships among ammonia formation intermediates to screen for new materials to boost reactivity. Although Mn_3NNi was identified to break the scaling relationship in Figure 6.5(b), Mn_3NNi is shown unable to boost the overall rate due to the high endergonicity in the second NH_3 formation cycle (see Figure 6.7 and Figure 6.9). On the other hand, Mn_2NFe_2 did break the scaling relationship in Figure 6.5(a) and exhibited the enhanced activity for ammonia production with more favorable thermodynamics than Mn_4N,

Ni_t@Mn_4N and Mn_3NNi, as shown in Figure 6.9. In this case, it is proved that linear scaling relationships can be utilized profitably for the more active catalysts design.

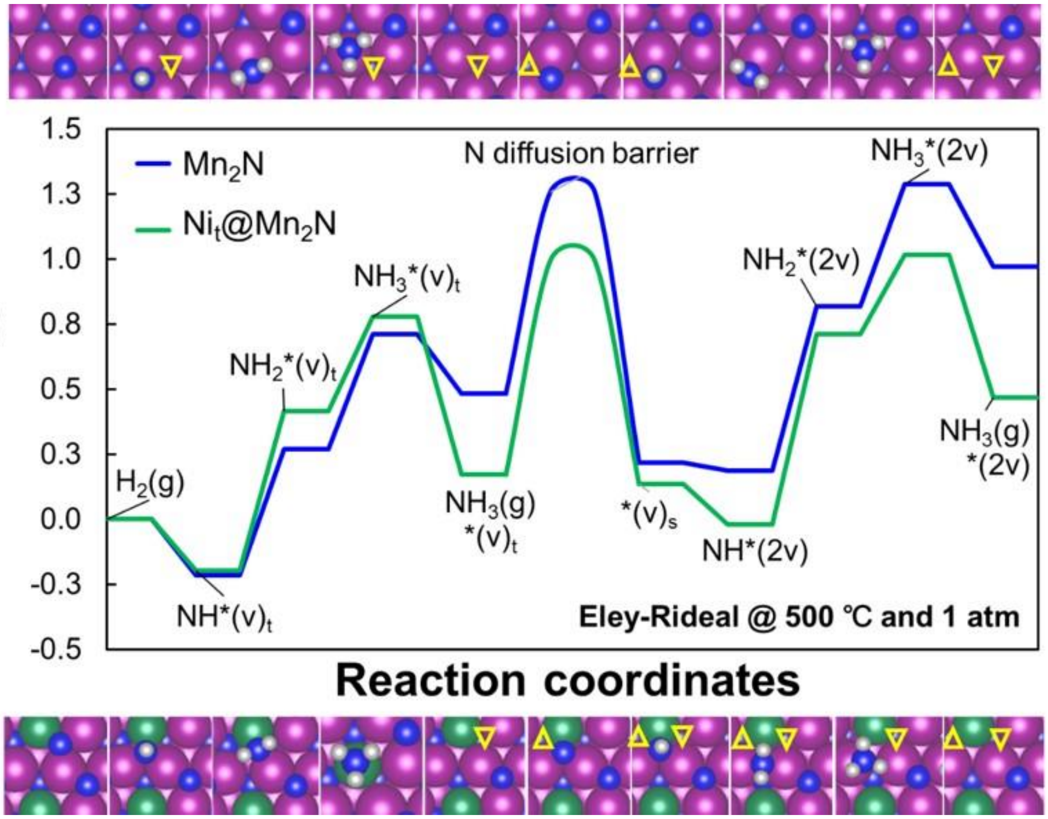

Figure 6.10 Free energies for the production of two NH_3 molecules via the Eley-Rideal mechanism on Mn_2N (solid blue), and Ni_t@Mn_2N (solid green) at 500 °C and 1 atm. Optimized structures on Mn2N and Ni_t@Mn_2N corresponding to each elementary step are depicted in the top and bottom panels, respectively. The top-layer N vacancy site is denoted by a downward yellow triangle, while the sublayer N vacancy site is indicated with an upward yellow triangle. Mn, Ni, N, and H are in magenta, green, blue and gray, respectively.

6.4.3 NH_3 Production on Mn_2N

Mn_2N represents a higher N-content Mn nitride phase. In this section, its performance for NH_3 production is evaluated using the Eley-Rideal mechanism. The free energies (in blue) for NH_3 formation are shown in Figure 6.10.

NH, NH_2 and NH_3 prefer the 3-fold, bridge and top sites, respectively, on Mn_2N, as illustrated in the top panels in Figure 6.10. Similar to Mn_4N, the NH formation (R24) is the exergonic step with -0.21 eV on Mn_2N, while NH_2 and NH_3 formations (R25-R26) are both endergonic, 0.49 and 0.44 eV. The release of NH_3 from the surface (R22) is exergonic (-0.23 eV). The sublayer lattice N diffusion onto surface is easier on Mn_2N than on Mn_4N at 0.78 eV (versus 1.12 eV). The trend for the second NH_3 formation resembles to the formation of the first NH_3 molecule on Mn_2N. The overall free energy to produce two NH_3 molecules on Mn_2N is 0.97 eV, which is much lower than that on Mn_4N (2.67 eV).

The scaling relationship can be broken on $Ni_t@Mn_2N$ as well, as shown in Figure 6.5. The reactivity is shown in Figure 6.10 in green. The most stable adsorption sites for NH, NH_2 and NH_3 on $Ni_t@Mn_2N$ (bottom panels in Figure 6.10) resemble to that on Mn_2N. Although the advantages for the formations of NH, NH_2 and NH_3 in first reduction cycle on $Ni_t@Mn_2N$ are not obvious when compared to Mn_2N, NH_3 desorption is more favorable on $Ni_t@Mn_2N$ (-0.61 eV) when compared Mn_2N (-0.23 eV). After overcoming an energy barrier of 0.82 eV, the second NH_3 production on $Ni_t@Mn_2N$ becomes more favorable. The overall free energy for the formation of two NH_3 molecules is 0.47 eV, lower than 0.97 eV on Mn_2N. It indicates that Ni-doping remains beneficial for NH_3 production regardless of the nitride lattice structures and N-content.

6.5 Conclusions

In this chapter, we focused on the modifications of Mn nitride to boost NH_3 production. Additional doped systems have been considered. Guided by the linear scaling relationship between NH_x (x=0, 1, 2), our search aims specially at systems that are able to strengthen NH_2 and NH_3 binding without too strong NH binding at the same time. Mn_3NNi, Mn_2NFe_2, Mn_2N and $Ni_t@Mn_2N$ have been identified. Mars-van Krevelen and Eley-Rideal reaction mechanisms were proposed. By comparing the free energies for NH_3 formation on different surfaces, Mn_2NFe_2 exhibit enhanced activity over Mn_4N, $Ni_t@Mn_4N$ and Mn_3NNi. It is shown that binary alloy of Mn-Ni nitride does not necessarily benefit NH_3 production. In addition, more thermodynamically favorable behaviors have been observed on Mn_2N due to high lattice N concentration. The $Ni_t@Mn_2N$ exhibits promising ability to further enhance NH_3 production.

6.6 Acknowledgments

This work was financially supported by the U.S. Department of Energy, Office of Science, Office of DOE EPSCoR (DE-FOA-0001572). Nannan Shan is thankful for the Sustainable Energy Award provided by Center of Sustainability Energy at Kansas State University. DFT calculations were performed thanks to the supercomputing service provided by K-State Beocat Research Cluster funded in part by NSF grants CHE-1726332, CNS-1006860, EPS-1006860, and EPS-0919443; Center for Nanoscale Materials (CNM) at Argonne National Laboratory supported by the Office of Science of the US Department of Energy under the contract No. DE-AC02-06CH11357; and the National Energy Research Scientific Computing Center (NERSC) under the contract No. DE-AC02-05CH11231.

Bibliography

[1]. Mittasch, A.; Frankenburg, W., Early Studies of Multicomponent Catalysts. In *Advances in Catalysis*, Frankenburg, W. G.; Komarewsky, V. I.; Rideal, E. K., Eds. Academic Press: 1950; Vol. 2, pp 81-104.

[2]. Michalsky, R.; Parman, B. J.; Amanor-Boadu, V.; Pfromm, P. H., Solar thermochemical production of ammonia from water, air and sunlight: Thermodynamic and economic analyses. *Energy* **2012,** 42, (1), 251-260.

[3]. Michalsky, R.; Pfromm, P. H., Thermodynamics of metal reactants for ammonia synthesis from steam, nitrogen and biomass at atmospheric pressure. *AIChE Journal* **2012,** 58, (10), 3203-3213.

[4]. Michalsky, R.; Pfromm, P. H., An Ionicity Rationale to Design Solid Phase Metal Nitride Reactants for Solar Ammonia Production. *The Journal of Physical Chemistry C* **2012,** 116, (44), 23243-23251.

[5]. Michalsky, R.; Avram, A. M.; Peterson, B. A.; Pfromm, P. H.; Peterson, A. A., Chemical looping of metal nitride catalysts: low-pressure ammonia synthesis for energy storage. *Chemical Science* **2015,** 6, (7), 3965-3974.

[6]. Michalsky, R.; Pfromm, P. H.; Steinfeld, A., Rational Design of Metal Nitride Redox Materials for Solar-driven Ammonia Synthesis. *Interface Focus* **2015,** 5, (3), 20140084.

[7]. Heidlage, M. G.; Kezar, E. A.; Snow, K. C.; Pfromm, P. H., Thermochemical Synthesis of Ammonia and Syngas from Natural Gas at Atmospheric Pressure. *Industrial & Engineering Chemistry Research* **2017,** 56, (47), 14014-14024.

[8]. McEnaney, J. M.; Singh, A. R.; Schwalbe, J. A.; Kibsgaard, J.; Lin, J. C.; Cargnello, M.; Jaramillo, T. F.; Nørskov, J. K., Ammonia synthesis from N_2 and H_2O using a lithium cycling electrification strategy at atmospheric pressure. *Energy & Environmental Science* **2017,** 10, (7), 1621-1630.

[9]. Zhang, L.; Ji, X.; Ren, X.; Luo, Y.; Shi, X.; Asiri, A. M.; Zheng, B.; Sun, X., Efficient Electrochemical N_2 Reduction to NH_3 on MoN Nanosheets Array under Ambient Conditions. *ACS Sustainable Chemistry & Engineering* **2018,** 6, (8), 9550-9554.

[10]. Shan, N.; Chikan, V.; Pfromm, P.; Liu, B., Fe and Ni Dopants Facilitating Ammonia Synthesis on Mn4N and Mechanistic Insights from First-Principles Methods. *The Journal of Physical Chemistry C* **2018,** 122, (11), 6109-6116.

[11]. Abghoui, Y.; Garden, A. L.; Hlynsson, V. F.; Björgvinsdóttir, S.; Ólafsdóttir, H.; Skúlason, E., Enabling electrochemical reduction of nitrogen to ammonia at ambient conditions through rational catalyst design. *Physical Chemistry Chemical Physics* **2015,** 17, (7), 4909-4918.

[12]. Abghoui, Y.; Garden, A. L.; Howalt, J. G.; Vegge, T.; Skúlason, E., Electroreduction of N_2 to Ammonia at Ambient Conditions on Mononitrides of Zr, Nb, Cr, and V: A DFT Guide for Experiments. *ACS Catalysis* **2016,** 6, (2), 635-646.

[13]. Abghoui, Y.; Skúlason, E., Electrochemical Synthesis of Ammonia via Mars-van Krevelen Mechanism on the (111) Facets of Group III–VII Transition Metal Mononitrides. *Catalysis Today* **2017,** 286, (Supplement C), 78-84.

[14]. Howalt, J. G.; Vegge, T., Electrochemical ammonia production on molybdenum nitride nanoclusters. *Physical Chemistry Chemical Physics* **2013,** 15, (48), 20957-20965.

[15]. Zeinalipour-Yazdi, C. D.; Hargreaves, J. S. J.; Catlow, C. R. A., Nitrogen Activation in a Mars–van Krevelen Mechanism for Ammonia Synthesis on Co3Mo3N. *The Journal of Physical Chemistry C* **2015,** 119, (51), 28368-28376.

[16]. Zeinalipour-Yazdi, C. D., On the possibility of an Eley–Rideal mechanism for ammonia synthesis on Mn6N5+x (x = 1)-(111) surfaces. *Physical Chemistry Chemical Physics* **2018,** 20, (27), 18729-18736.

[17]. Li, Q.; He, L.; Sun, C.; Zhang, X., Computational Study of MoN_2 Monolayer as Electrochemical Catalysts for Nitrogen Reduction. *The Journal of Physical Chemistry C* **2017,** 121, (49), 27563-27568.

[18]. Munter, T. R.; Bligaard, T.; Christensen, C. H.; Nørskov, J. K., BEP relations for N_2 dissociation over stepped transition metal and alloy surfaces. *Physical Chemistry Chemical Physics* **2008,** 10, (34), 5202-5206.

[19]. Laassiri, S.; Zeinalipour-Yazdi, C. D.; Catlow, C. R. A.; Hargreaves, J. S. J., The Potential of Manganese Nitride Based Materials as Nitrogen Transfer Reagents for Nitrogen Chemical Looping. *Applied Catalysis B: Environmental* **2018,** 223, 60-66.

[20]. Fernández, E. M.; Moses, P. G.; Toftelund, A.; Hansen, H. A.; Martínez, J. I.; Abild-Pedersen, F.; Kleis, J.; Hinnemann, B.; Rossmeisl, J.; Bligaard, T.; Nørskov, J. K., Scaling Relationships for Adsorption Energies on Transition Metal Oxide, Sulfide, and Nitride Surfaces. *Angewandte Chemie International Edition* **2008,** 47, (25), 4683-4686.

[21]. Kresse, G.; Hafner, J., Ab initio Molecular Dynamics for Open Shell Transitio Metals. *Physical Review B* **1993,** 48, (17), 13115-13118.

[22]. Kresse, G.; Furthmuller, J., Efficiency of *Ab initio* Total Energy Calculations for Metals and Semiconductors using A Plane-wave Basis Set. *Computational Materials Science* **1996,** 6, (1), 15-50.

[23]. Perdew, J. P.; Burke, K.; Ernzerhof, M., Generalized Gradient Approximation Made Simple. *Physical Review Letters* **1996,** 77, (18), 3865-3868.

[24]. Blochl, P. E., Projector Augmented Wave Method *Physical Review B* **1994,** 50, (24), 17953-17979.

[25]. Niewa, R., Nitridocompounds of manganese: manganese nitrides and nitridomanganates. *Zeitschrift für Kristallographie-Crystalline Materials* **2002,** 217, (1), 8-23.

[26]. Feng, W. J.; Sun, N. K.; Du, J.; Zhang, Q.; Liu, X. G.; Deng, Y. F.; Zhang, Z. D., Structural Evolution and Magnetic Properties of Mn–N Compounds. *Solid State Communications* **2008,** 148, (5), 199-202.

[27]. Yu, R.; Chong, X.; Jiang, Y.; Zhou, R.; Yuan, W.; Feng, J., The stability, electronic structure, elastic and metallic properties of manganese nitrides. *RSC Advances* **2015,** 5, (2), 1620-1627.

[28]. Mekata, M.; Haruna, J.; Takaki, H., Neutron Diffraction Study of Antiferromagnetic Mn_2N. *Journal of the Physical Society of Japan* **1968,** 25, (1), 234-238.

[29]. Fruchart, D.; Bertaut, E. F.; Madar, R.; Lorthioir, G.; Fruchart, R., Structure magnetique et rotation de spin de Mn_3NiN. *Solid State Communications* **1971,** 9, (21), 1793-1797.

[30]. Bertaut, E. F.; Fruchart, D.; Bouchaud, J. P.; Fruchart, R., Diffraction neutronique de Mn_3GaN. *Solid State Communications* **1968,** 6, (5), 251-256.

[31]. Henkelman, G.; Uberuaga, B. P.; Jonsson, H., A climbing image nudged elastic band method for finding saddle points and minimum energy paths. *Journal of Chemical Physics* **2000,** 113, (22), 9901-9904.

[32]. Henkelman, G.; Jónsson, H., A Dimer Method for Finding Saddle Points on High Dimensional Potential Surfaces using Only First Derivatives. *The Journal of Chemical Physics* **1999,** 111, (15), 7010-7022.

[33]. Le, T. N.-M.; Liu, B.; Huynh, L. K., SurfKin: An Ab initio Kinetic Code for Modeling Surface Reactions. *Journal of Computational Chemistry* **2014,** 35, (26), 1890-1899.

[34]. Shan, N.; Zhou, M.; Hanchett, M. K.; Chen, J.; Liu, B., Practical Principles of Density Functional Theory for Catalytic Reaction Simulations on Metal Surfaces – from Theory to Applications. *Molecular Simulation* **2017,** 43, (10-11), 861-885.

Chapter 7 - Conclusions

In this dissertation, two case examples, electrochemical reduction of furfural on transition metals and step-catalysis for ammonia synthesis with manganese nitrides, were used to demonstrate how molecular-level modeling is utilized for rational catalysts design. The molecular interactions and mechanical properties were revealed by periodic DFT calculations. Free energy diagrams coupling with scaling relationships were displayed, which illustrated the reaction activities and catalytic trend of different catalysts for furfural reduction and ammonia synthesis. With the computational investigations, the questions proposed in Chapter 1 have been addressed.

(1) Five pathways for FA and MF production on Ag, Pb and Ni were evaluated. The mh6 is the favored intermediate on Ag and Pb for both FA and MF formations. However, pathways involving the mh7 intermediate are competitive against the mh6 pathways on Ni due to the strong binding of the furan ring.

(2) The first hydrogenation step and C-O bond cleavage are likely to be the rate-limiting step for FA and MF production, respectively. Although MF formation is more thermodynamically favorable than FA formation on Ag, Pb and Ni, the kinetics will be reduced due to the higher energy barriers of C-O bond cleavage for MF production.

(3) The interactions between metal-water, water-water and adsorbate-water for adsorptions of glycerol and its dehydrogenated intermediates on Pt were elucidated in the aqueous phase. A network-like structure formed collaboratively by water and adsorbates has been observed. In addition, it is notable that the scaling relationship established in solvent-free scheme still works for the adsorption energy estimations in aqueous phase, which will greatly improve the computational efficiency for the reactions involving complex biomass molecules.

(4) The Mars-van Krevelen and Eley-Rideal reaction mechanisms were evaluated for ammonia synthesis using Mn nitrides. On Mn_4N, ammonia production is endergonic with weak H, NH_2 and NH_3 adsorptions and high N diffusion barriers.

(5) Sublayer Fe- and Ni-doped Mn_4N facilitate N diffusion and can enhance the second NH_3 formation. On the other hand, Ni-doped Mn_4N in the top-layer ($Ni_t@Mn_4N$) boosts NH_3 production due to the enhanced H binding.

(6) Linear scaling relationships between NH_x (x=1, 2) and elemental N indicate that NH_2 adsorption has to be strengthened, and in the meantime, NH adsorption cannot be too strong. Therefore, alloys based on Mn_4N and doping Mn_2N were examined for NH_3 production. Mn_2NFe_2, Mn_2N and $Ni_t@Mn_2N$ broke the linear scaling relationship and were selected for the validations for NH_3 synthesis. It turns out that all of these Mn nitride configurations exhibit improved activity for ammonia production compared to Mn_4N and $Ni_t@Mn_4N$.

Throughout this dissertation, convincing evidence has been obtained to show DFT calculations can be used to produce molecular and mechanistic insights that are necessary for functional catalysts design. However, more work lies ahead in order to further refine and improve the predictive power of DFT modeling for catalysis and catalyst design. In fact, the catalytic trend can be received through the ‘volcano’ plot using the micro-kinetic modeling, which has been believed as a powerful approach for catalytic trend prediction. Through kinetic modeling, both intrinsic properties of catalysts and the environmental effects, such as temperature, pressure and solvation, can be analyzed in a more quantitative fashion. Along with the development of computational hardware as well as the computational theories, DFT modeling integrating with experiments will pave more promising avenues for advanced materials design.

Appendix A - Electrochemical Reduction of Furfural on Transition Metals

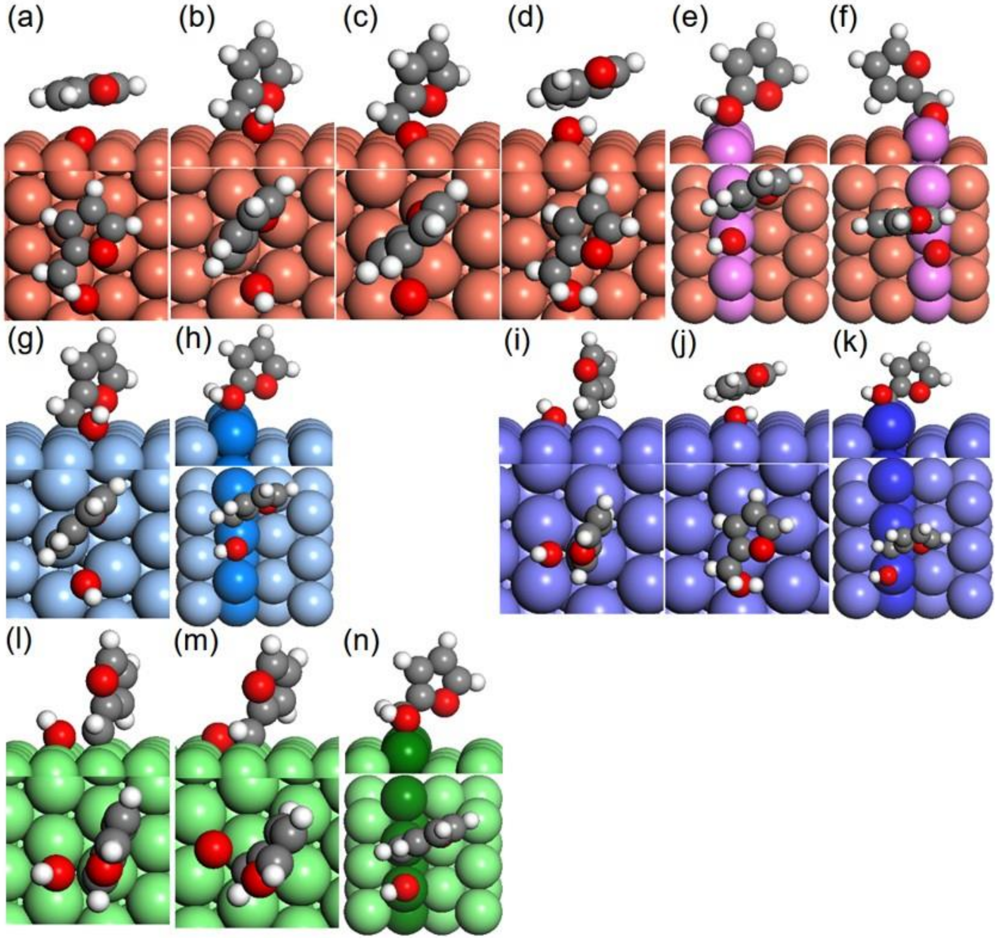

Figure A.1 The geometries of transition state obtained from PBE functional for C-O bond cleavage of (a) mh6 on Cu(111), (b) mh7 on Cu(111), (c) furfural on Cu(111), (d) FA on Cu(111), (e) mh7 on Cu(211), (f) furfural on Cu(211), (g) mh7 on Ag(111), (h) mh7 on Ag(211), (i) mh7 on Pb(111), (j) FA on Pb(111), (k) mh7 on Pb(211), (l) mh7 on Ni(111), (m) furfural on Ni(111), and (n) mh7 on Ni(211). The grey, red, white, orange, blue, purple and green spheres represent C, O, H, Cu, Ag, Pb, and Ni, respectively. The step edges are highlighted.

Table A.1 Energy barriers (eV) for C-O bond cleavage on Cu, Ag, Pb and Ni surfaces in vacuum.

	PBE	optPBE	optB88
Cu(111) mh6 dissociation	1.24		
Cu(111) mh7 dissociation	0.75	0.78	
Cu(211) mh7 dissociation	0.72		
Cu(111) furfural dissociation	1.47	1.57	1.69
Cu(211) furfural dissociation	1.62		1.60
Cu(111) FA dissociation	0.93	0.87	
Ag(111)mh7 dissociation	1.29		
Ag(211)mh7 dissociation	1.41	1.23	1.25
Pb(111) mh7 dissociation	0.99		
Pb(211) mh7 dissociation	1.25	1.09	1.14
Pb(111) FA dissociation	0.95	0.84	
Ni(111) mh7 dissociation	1.09	1.05	
Ni(211) mh7 dissociation	1.26	0.93	
Ni(111) furfural dissociation	1.18	1.30	1.45

Microkinetic modeling of electrochemical furfural reduction on transition metals

(1) Reaction mechanism ($C_5H_4O_2$ represents furfural, $C_5H_5O_2$ represents mh6, $C_5O_2H_5$ represents mh7)

'H_2_g → H_2_g',

'CO_g → CO_g',

'*_s + $C_5H_4O_2$_g → $C_5H_4O_2$*',

'$C_5H_4O_2$* + pe_g ↔ $C_5H_4O_2$-pe* → $C_5H_5O_2$*',

'$C_5H_4O_2$_s + pe_g ↔ pe-$C_5H_4O_2$_s → $C_5O_2H_5$_s',

'$C_5H_5O_2$* + pe_g ↔ $C_5H_5O_2$-pe* ↔ $C_5H_6O_2$*',

'$C_5O_2H_5$_s + pe_g ↔ $C_5O_2H_5$-pe_s ↔ $C_5H_6O_2$*',

'$C_5H_6O_2$* + *_s + pe_g ↔ C_5H_5OOH-pe* + *_s → C_5H_5O* + H_2O*',

'$C_5H_5O_2$* + *_s + pe_g ↔ C_5H_5OO-pe* + *_s → C_5H_5O* + OH*',

'$C_5O_2H_5$* + *_s + pe_g ↔ C_5H_4OOH-pe* + *_s → C_5H_4O* + H_2O*',

'$C_5H_4O_2$* + *_s + pe_g ↔ C_5H_4OO-pe* + *_s → C_5H_4O* + OH*',

'C_5H_4O* + pe_g ↔ C_5H_4O-pe* → C_5H_5O*',

'C_5H_5O* + pe_g ↔ C_5H_5O-pe*→ C_5H_6O*',

'C_5H_6O* ↔ C_5H_6O_g + *_s',

'$C_5H_6O_2$* ↔ $C_5H_6O_2$_g + *_s',

'OH* + pe_g → H_2O_g + *_s',

'H_2O* ↔ H_2O_g + *_s',

(2) Reaction conditions

Voltage = -0.6 V, Pressure of $C_5H_4O_2$ = 1/11, Pressure of pe_g (i.e. proton) = 10/11

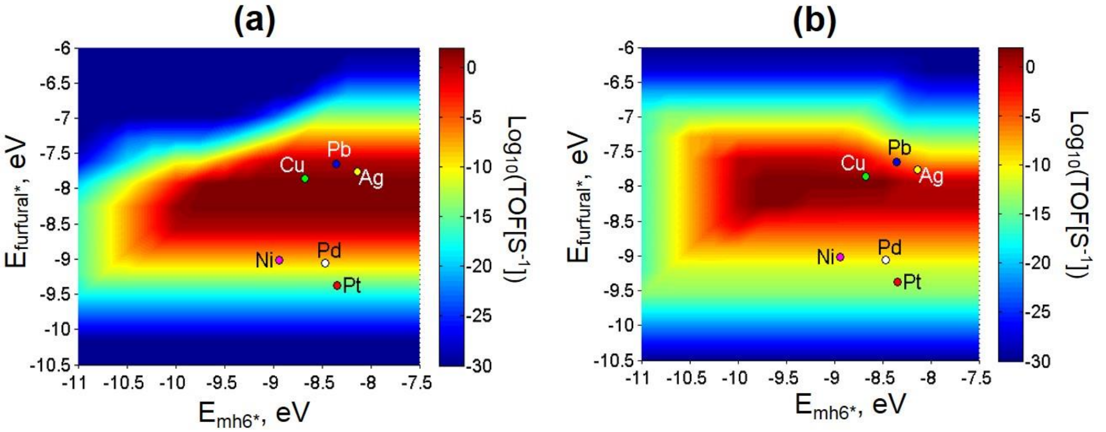

Figure A.2 Volcano plots obtained from micro-kinetic modeling for (a) furfuryl alcohol (FA) and (b) 2-methylfuran (MF) formations at 298 K, 1 atm. The applied potential is -0.6 V. Adsorption energies of furfural and mh6 were used as the descriptors.

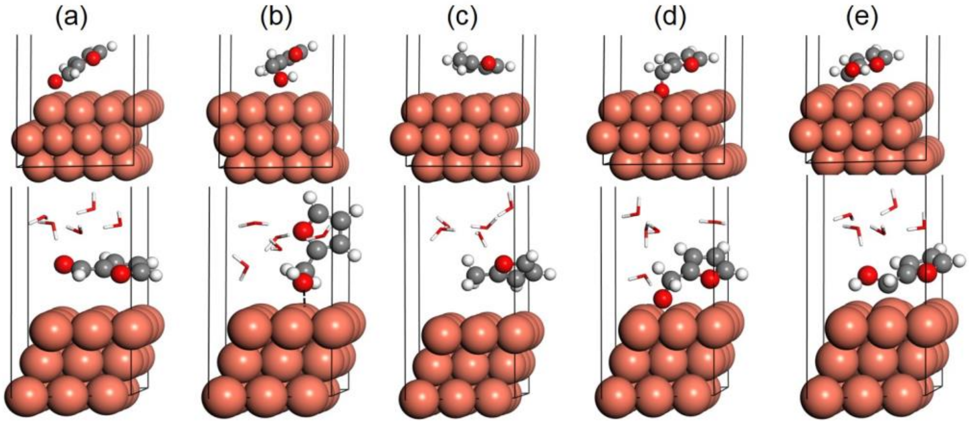

Figure A.3 The adsorption geometries of (a) furfural, (b) furfuryl alcohol (FA), (c) 2-methylfuran (MF), (d) mh6, and (e) mh7 in vacuum (top panel) and aqueous solution (bottom panel) on Cu(111). Cu, C, O and H are in orange, grey, red and white, respectively.

Table A.2 Adsorptions energies (in eV) of furfural, furfuryl alcohol, 2-methylfuran, mh6 and mh7 in vacuum and solution on Cu(111).

	furfural	FA	MF	mh6	mh7
vacuum (eV)	-0.69	-0.81	-0.76	-2.96	-1.19
solution (eV)	-0.79	-0.89	-0.55	-2.83	-1.18

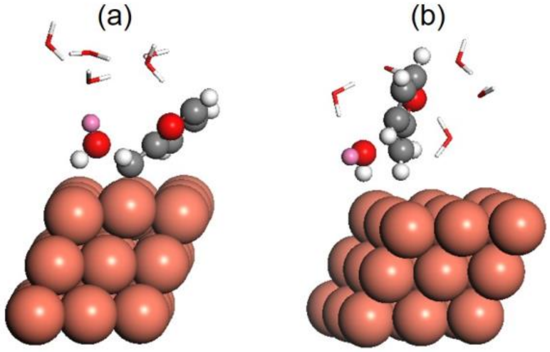

Figure A.4 The configurations of transition state for C-O bond cleavage of (a) mh7 and (b) furfuryl alcohol (FA) on Cu(111) with solvation. Cu, C, O and H are in orange, grey, red and white, respectively. The involved proton is highlighted in pink color.

Table A.3 Comparison of energy barriers (in eV) of C-O bond cleavage in mh7 and furfuryl alcohol (FA) on Cu(111) in vacuum and solution.

C-O bond cleavage of	vacuum (eV)	solution (eV)
mh7	0.76	0.30
furfuryl alcohol (FA)	0.93	0.54

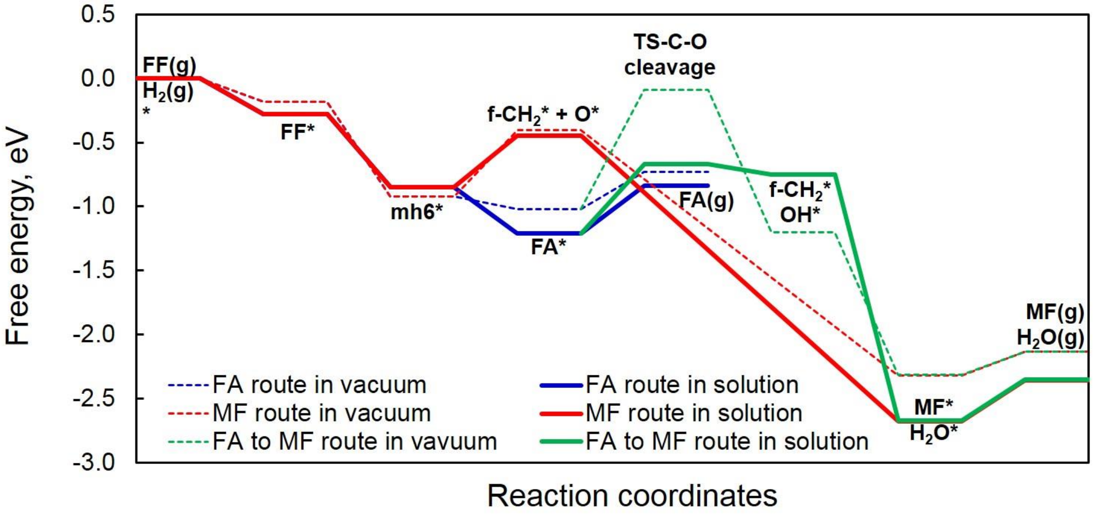

Figure A.5 Free energy diagrams for FA and MF production on Cu(111) in vacuum (dashed lines) and solution (solid lines).

Appendix B - Ammonia Synthesis on Mn_4N

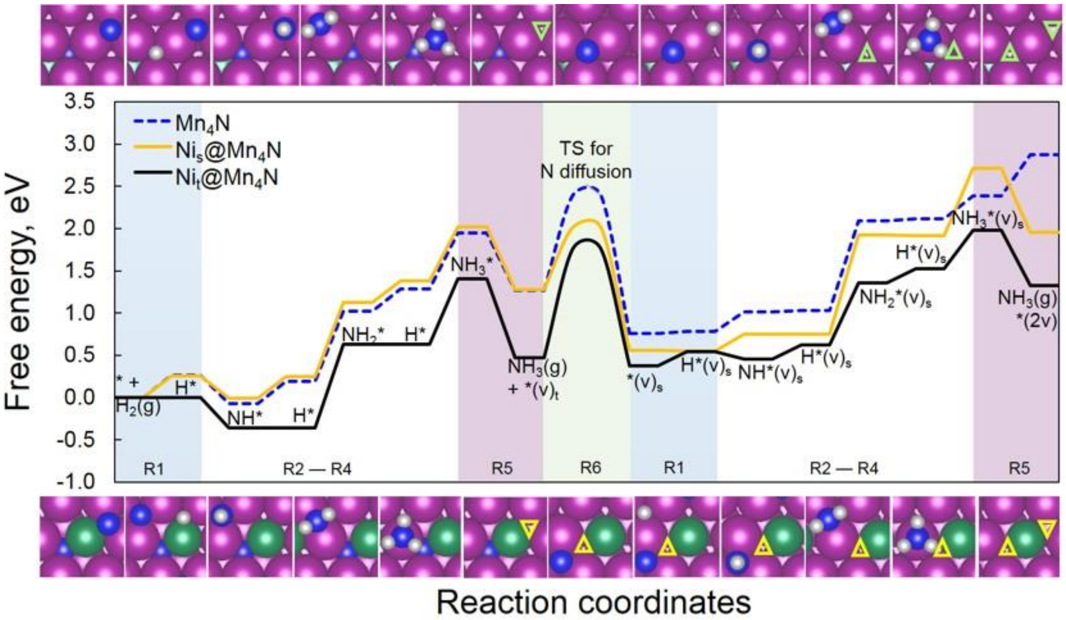

Figure B.1 Free energy diagrams for NH_3 production (2 NH_3 molecules) on pure N terminated Mn_4N (dashed blue as the reference), $Ni_s@Mn_4N$ (yellow line) and $Ni_t@Mn_4N$ (black line) at 700 °C and 1 bar. Optimized intermediate structures corresponding to elementary steps are also shown. Surface N vacancy is represented with a downward triangle, while the sublayer N vacancy is represented with an upward triangle. Triangles are in green for $Ni_s@Mn_4N$ and in yellow for $Ni_t@Mn_4N$. Mn, Ni, N, and H atoms are in magenta, green, blue, and grey, respectively.

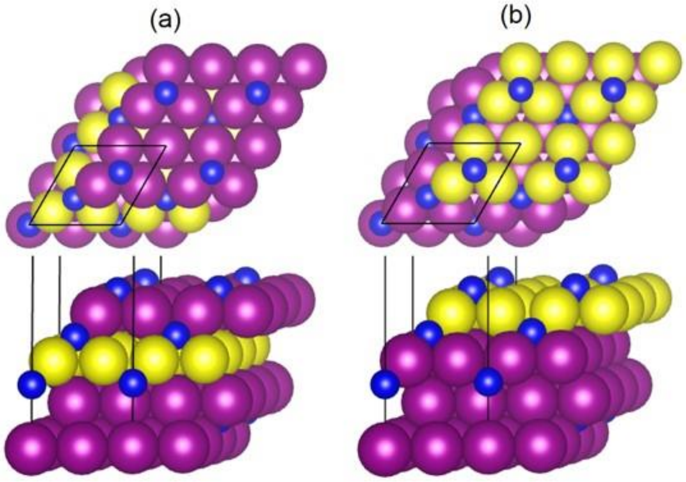

Figure B.2 Top and side views of (a) sub-monolayer, (b) top-monolayer doped N-terminated $Mn_4N(111)$ surfaces. Mn, N, and the dopant atom are in magenta, blue, and yellow, respectively. Black lines represent the periodic boundaries of the p(1x1) unit cell.

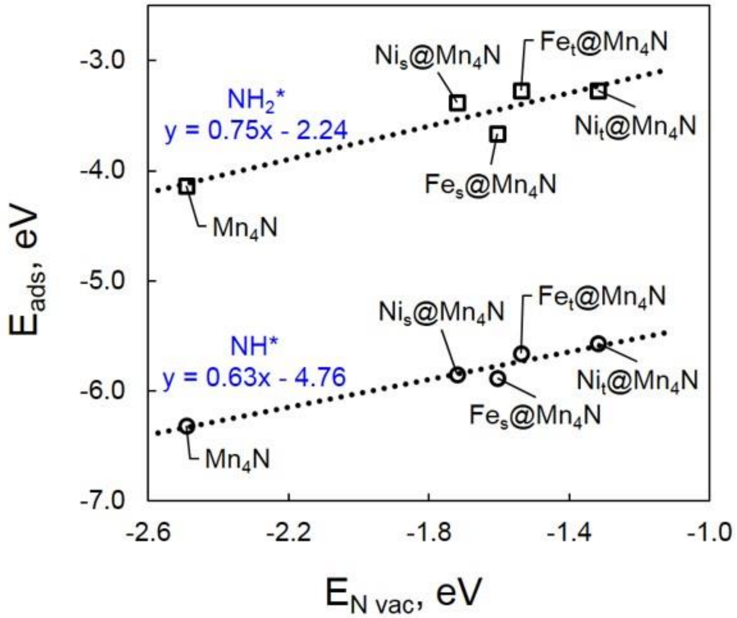

Figure B.3 Scaling relationships (black dash lines) between N binding energy ($E_{N\ vac}$) and adsorption energies of NH* (hollow circle) and NH_2* (hollow square) on the surface with N vacancy in the sublayer.

Appendix C - Reprint Permissions

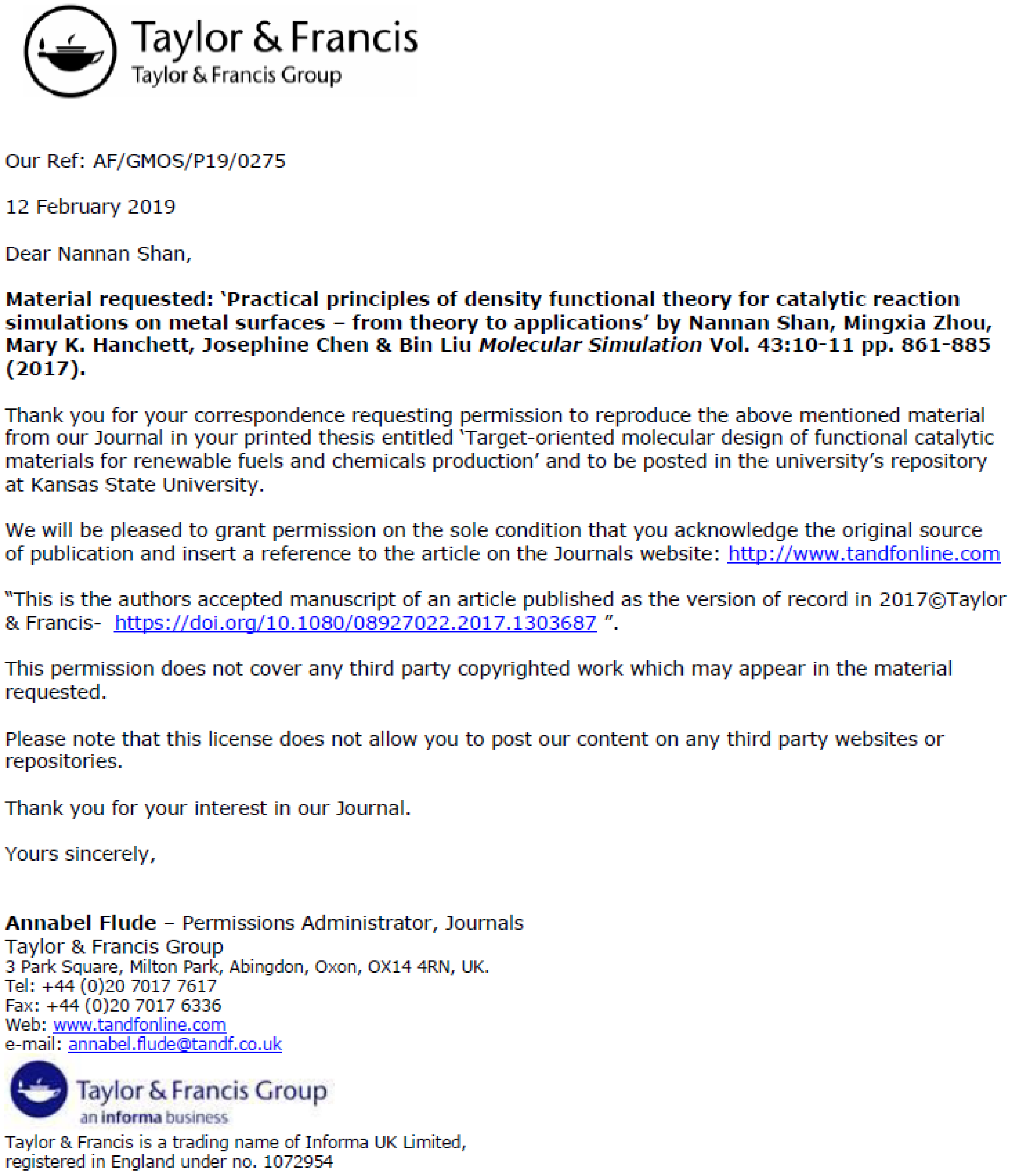

Taylor & Francis
Taylor & Francis Group

Our Ref: AF/GMOS/P19/0275

12 February 2019

Dear Nannan Shan,

Material requested: 'Practical principles of density functional theory for catalytic reaction simulations on metal surfaces – from theory to applications' by Nannan Shan, Mingxia Zhou, Mary K. Hanchett, Josephine Chen & Bin Liu *Molecular Simulation* Vol. 43:10-11 pp. 861-885 (2017).

Thank you for your correspondence requesting permission to reproduce the above mentioned material from our Journal in your printed thesis entitled 'Target-oriented molecular design of functional catalytic materials for renewable fuels and chemicals production' and to be posted in the university's repository at Kansas State University.

We will be pleased to grant permission on the sole condition that you acknowledge the original source of publication and insert a reference to the article on the Journals website: http://www.tandfonline.com

"This is the authors accepted manuscript of an article published as the version of record in 2017©Taylor & Francis- https://doi.org/10.1080/08927022.2017.1303687 ".

This permission does not cover any third party copyrighted work which may appear in the material requested.

Please note that this license does not allow you to post our content on any third party websites or repositories.

Thank you for your interest in our Journal.

Yours sincerely,

Annabel Flude – Permissions Administrator, Journals
Taylor & Francis Group
3 Park Square, Milton Park, Abingdon, Oxon, OX14 4RN, UK.
Tel: +44 (0)20 7017 7617
Fax: +44 (0)20 7017 6336
Web: www.tandfonline.com
e-mail: annabel.flude@tandf.co.uk
Taylor & Francis Group
an informa business

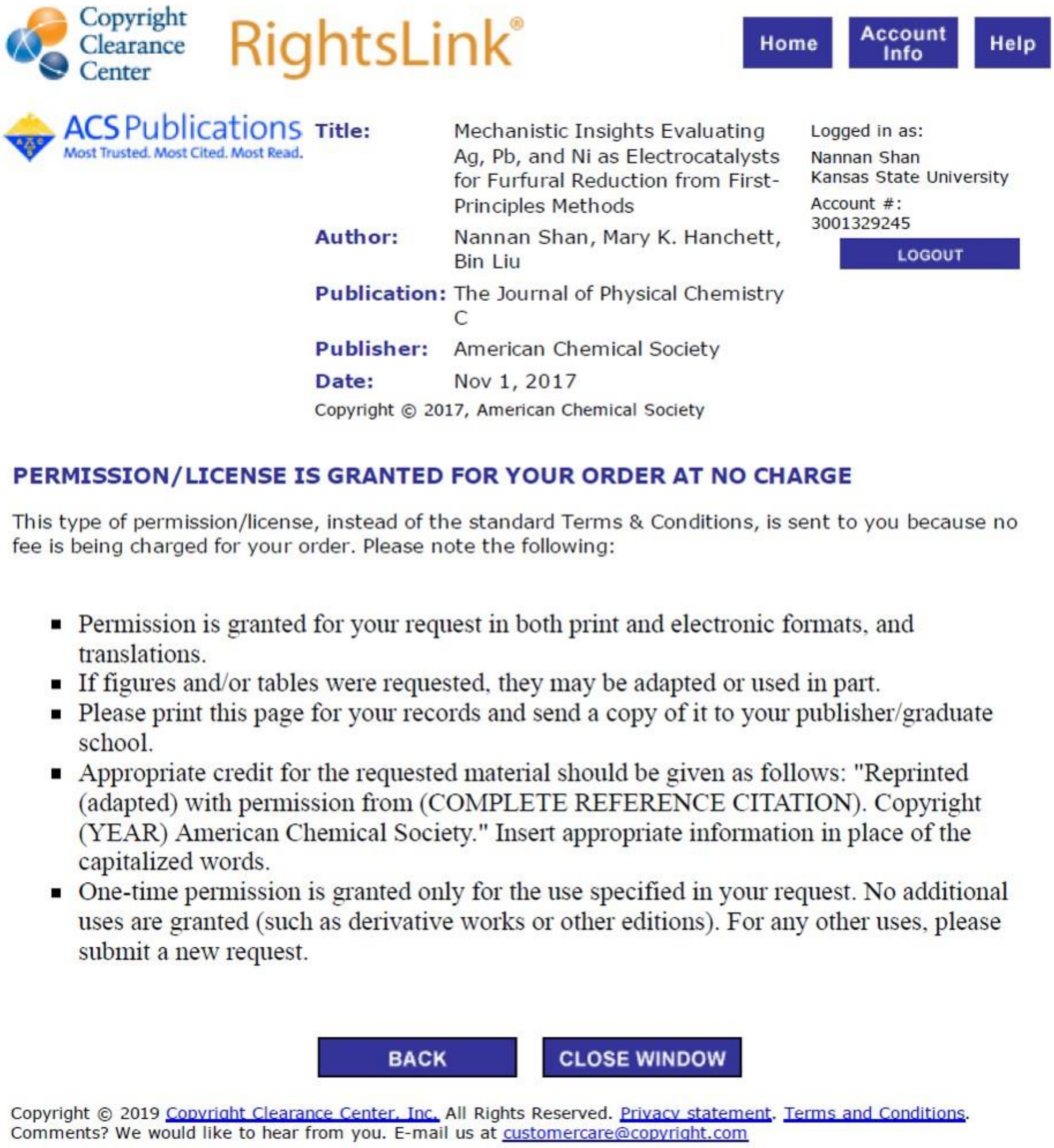

Title: Mechanistic Insights Evaluating Ag, Pb, and Ni as Electrocatalysts for Furfural Reduction from First-Principles Methods

Author: Nannan Shan, Mary K. Hanchett, Bin Liu

Publication: The Journal of Physical Chemistry C

Publisher: American Chemical Society

Date: Nov 1, 2017

Logged in as:
Nannan Shan
Kansas State University
Account #:
3001329245

PERMISSION/LICENSE IS GRANTED FOR YOUR ORDER AT NO CHARGE

This type of permission/license, instead of the standard Terms & Conditions, is sent to you because no fee is being charged for your order. Please note the following:

- Permission is granted for your request in both print and electronic formats, and translations.
- If figures and/or tables were requested, they may be adapted or used in part.
- Please print this page for your records and send a copy of it to your publisher/graduate school.
- Appropriate credit for the requested material should be given as follows: "Reprinted (adapted) with permission from (COMPLETE REFERENCE CITATION). Copyright (YEAR) American Chemical Society." Insert appropriate information in place of the capitalized words.
- One-time permission is granted only for the use specified in your request. No additional uses are granted (such as derivative works or other editions). For any other uses, please submit a new request.

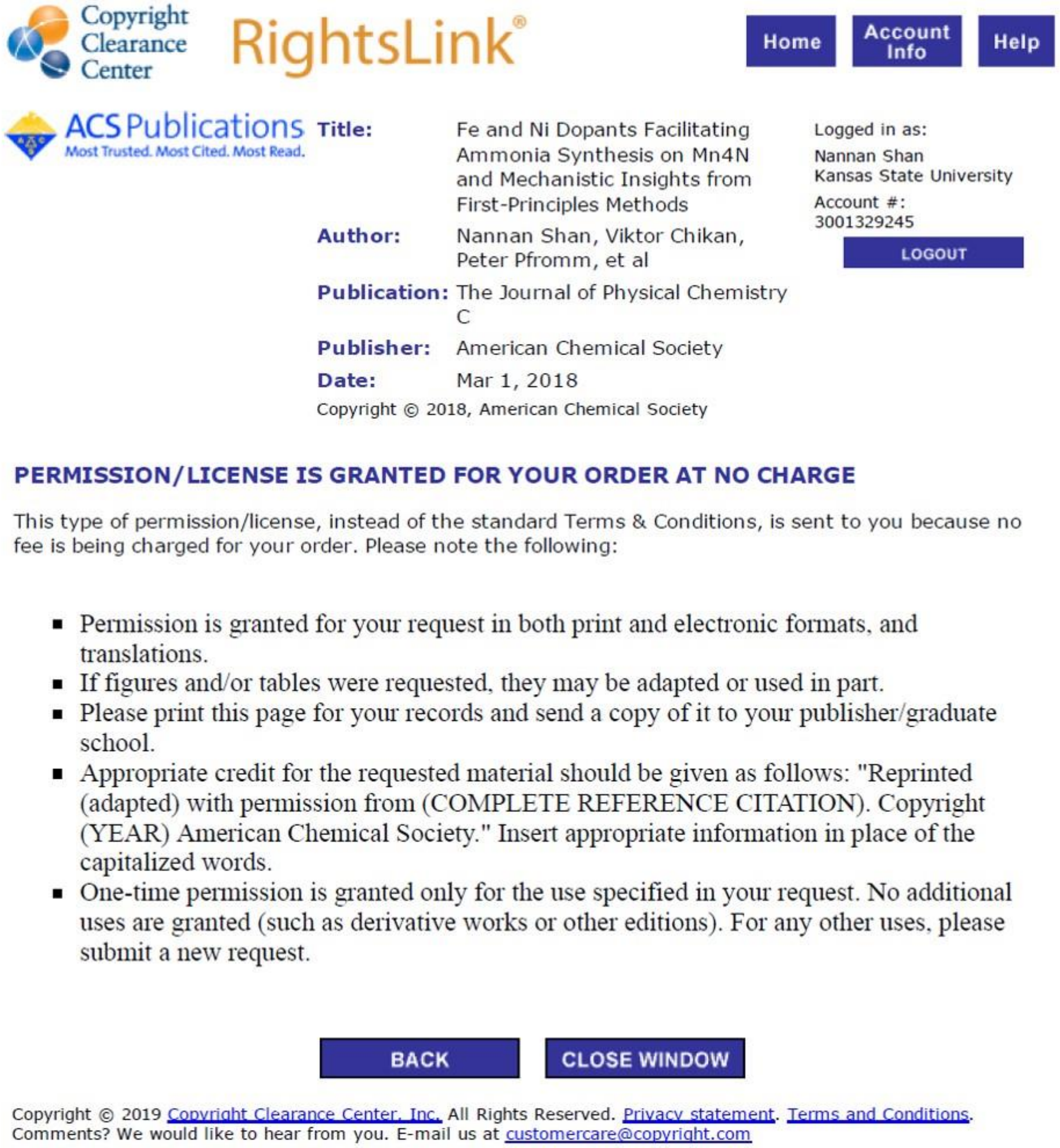

Title: Fe and Ni Dopants Facilitating Ammonia Synthesis on Mn4N and Mechanistic Insights from First-Principles Methods

Author: Nannan Shan, Viktor Chikan, Peter Pfromm, et al

Publication: The Journal of Physical Chemistry C

Publisher: American Chemical Society

Date: Mar 1, 2018

Logged in as:
Nannan Shan
Kansas State University
Account #:
3001329245

PERMISSION/LICENSE IS GRANTED FOR YOUR ORDER AT NO CHARGE

This type of permission/license, instead of the standard Terms & Conditions, is sent to you because no fee is being charged for your order. Please note the following:

- Permission is granted for your request in both print and electronic formats, and translations.
- If figures and/or tables were requested, they may be adapted or used in part.
- Please print this page for your records and send a copy of it to your publisher/graduate school.
- Appropriate credit for the requested material should be given as follows: "Reprinted (adapted) with permission from (COMPLETE REFERENCE CITATION). Copyright (YEAR) American Chemical Society." Insert appropriate information in place of the capitalized words.
- One-time permission is granted only for the use specified in your request. No additional uses are granted (such as derivative works or other editions). For any other uses, please submit a new request.

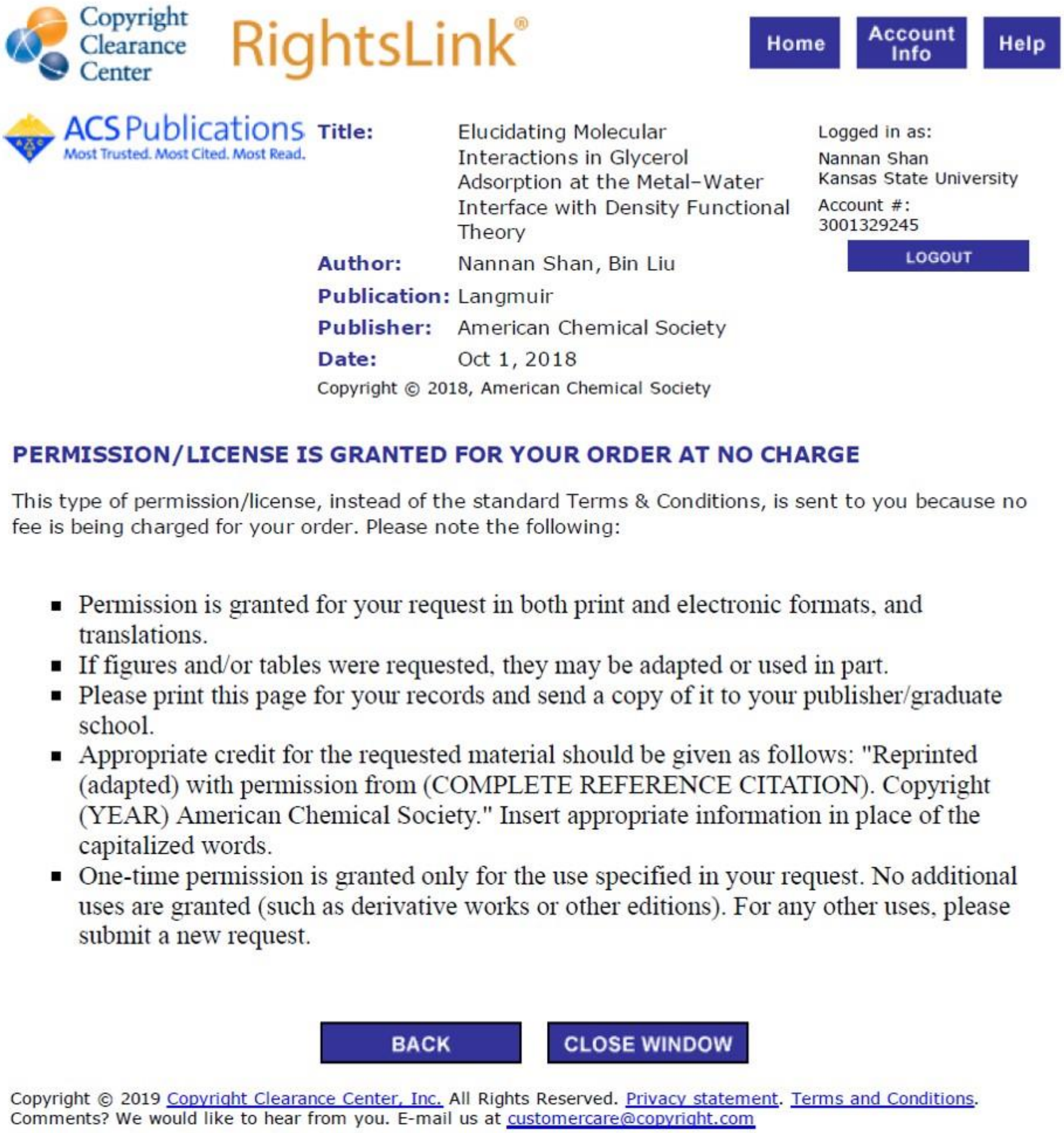

Title: Elucidating Molecular Interactions in Glycerol Adsorption at the Metal–Water Interface with Density Functional Theory

Author: Nannan Shan, Bin Liu

Publication: Langmuir

Publisher: American Chemical Society

Date: Oct 1, 2018

Logged in as:
Nannan Shan
Kansas State University
Account #:
3001329245

PERMISSION/LICENSE IS GRANTED FOR YOUR ORDER AT NO CHARGE

This type of permission/license, instead of the standard Terms & Conditions, is sent to you because no fee is being charged for your order. Please note the following:

- Permission is granted for your request in both print and electronic formats, and translations.
- If figures and/or tables were requested, they may be adapted or used in part.
- Please print this page for your records and send a copy of it to your publisher/graduate school.
- Appropriate credit for the requested material should be given as follows: "Reprinted (adapted) with permission from (COMPLETE REFERENCE CITATION). Copyright (YEAR) American Chemical Society." Insert appropriate information in place of the capitalized words.
- One-time permission is granted only for the use specified in your request. No additional uses are granted (such as derivative works or other editions). For any other uses, please submit a new request.